공학박사학위논문

# 슬라이더-텐던 구동기를 이용한 손 부위 착용형 로봇

## Tendon-Driven Hand Wearable Robot using Slider-Tendon Linear Actuator

2020 년 8 월

서울대학교 대학원

기계항공공학부

김 병 철

공학박사학위논문

# 슬라이더-텐던 구동기를 이용한 손 부위 착용형 로봇

## Tendon-Driven Hand Wearable Robot using Slider-Tendon Linear Actuator

2020 년 8 월

서울대학교 대학원

기계항공공학부

김 병 철

# 슬라이더-텐던 구동기를 이용한 손 부위 착용형 로봇

Tendon-Driven Hand Wearable Robot using Slider-Tendon Linear Actuator

지도교수 조 규 진

이 논문을 공학박사 학위논문으로 제출함

2020년 7월

서울대학교 대학원
기계항공공학부
김 병 철

김병철의 공학박사 학위논문을 인준함

2020년 5월

위 원 장 : ________________________

부위원장 : ________________________

위 원 : ________________________

위 원 : ________________________

위 원 : ________________________

# Tendon-Driven Hand Wearable Robot using Slider-Tendon Linear Actuator

Byungchul Kim
Department of Mechanical & Aerospace Engineering
Seoul National University

## Abstract

Due to significant improvements in actuation and sensing components in terms of size and performance, technologies for wearable devices have received great attention and have been developed for various purposes. In the wearable device development process, it is required to satisfy two different kinds of performance factors: Usability and functionality of the robot. It is because, unlike other devices, the wearable device should be worn on the human body. For instance, in hand wearable robot researches, the researchers have aimed for making compact, light, and soft device to guarantee the usability; For the functionality of the robot, on the other hand, they have attempted to design the robot that assists a sufficient number of grasp types with enough grasping force. Designing the robot that satisfies both performance factors is a challenging issue because of an inevitable trade-off between keeping the usability with less number of actuators and keeping the functionality by using numerous high-force actuators.

As a solution for the trade-off issue, a tendon-driven under-actuation mechanism has been proposed in previous researches. In this design, it is possible to reduce the number of actuators by applying a certain ratio

of torque to multiple joints. This concept of applying torque constraints satisfy both performance factors of usability and functionality because it not only enables to use of less number of actuators but also provides adaptability to external environments. However, design with an under-actuation mechanism still has an unsolved issue about scalability; The system becomes complicated and the friction increases in the transmission when the under-actuation mechanism is used to cover a large number of joints. Therefore, wearable robots using under-actuation mechanism have been developed to have limited functions.

This thesis proposes a method to deal with the aforementioned issue with 1) a novel actuator named Slider-Tendon Linear Actuator that is specifically designed for the tendon-driven under-actuation mechanism, and 2) a design framework to optimize the under-actuated tendon routing. Using these given two solution, a novel soft hand wearable robot named Exo-Glove II is developed to assist index, middle finger flexion/extension and thumb opposition/reposition with only four Slider Tendon Linear Actuators. With Exo-Glove II, the thesis also shows several useful research to improve the robot performance; 1) a method to find out the optimal tendon routing using a concept of opposition workspace; 2) a method to find out the kinematic information of human body using a kinematic calibration; 3) a data-driven method to find out the relationship between wire tension and joint angle for robot control. Using these researches, the thesis finally shows that it is possible to assist various types of grasp using the proposed robot.

Keywords: soft hand wearable robot, tendon transmission, tendon driven actuator, under-actuation, Data-driven system identification

Student number: 2014-30349

# Contents

# List of Figures

# List of Tables

**Appendix A**

**Appendix B**



**Appendix C**

**Appendix D**

# Chapter 1

# Introduction

## 1.1. Background

Advances in robot technology are expanding the environment in which robots can be used as well as robot function. Industrial robots that perform predetermined tasks in a controlled environment such as factories or robots that operate to replace human tasks in extreme environments have been developed. Recently, wearable robots or robotic prosthetics in environments where human lives are being developed to assist human tasks. Since the human assist robots have high potential to improve the quality of life by being closely located to the human body, these robots have received great attention. Among the wearable robots for various body parts, hand wearable robots are one of the studies that have received much attention. It is because hand performs versatile roles in activities of daily living.

In the wearable robot development, unlike design process of the conventional robot, it is important to think about the fact that the robots are intended to be worn on the human body. In order to consider the fact, the researchers have attempted to design a compact and light weight robot with safe actuation (De Santis *et al.* 2008); These characteristics are usually called as a *usability* of the robot. Among body parts, the hand is one of the most difficult areas to satisfy the usability. It is because - due to the inherent characteristic of the hand that has numerous joints in a compact space - the hand wearable robots require lots of actuators and high performance controllers. Several enabling technologies have been applied on the hand wearable robot studies to enhance the usability. Some well-used technologies that improves the usability of the hand wearable robot are as below; More details of the hand wearable robots in the previous researches can be found in Appendix A.1.

1. Soft robotics

   Design method of using soft material as a robot body has been recently used in the robot researches and is called as a *soft robotics*. One major advantage of soft robotics is an *adaptability* to the external environment (Alexander *et al.* 2015); Unlike the robot using rigid components, the soft robots has an ability to change its shape to the external environment (Chu & Patterson 2018; Shahid *et al.* 2018). In the wearable robot study, by using this method, the problem of fitting robot size to human body can be easily handled because a soft structure can fit well against the human body, even if there is a slight difference in size. Also, the use of soft material makes soft robots more compact; this is because - due to the inherent characteristics of soft wearable robots - there are no joint alignment issues. Joint alignment issues in rigid robots are a safety concern; efforts to minimize these issues result in added size (Cempini *et al.* 2015*a*;

Chiri *et al.* 2012). This aspect is especially effective in hand because hand has lots of joints in a compact size.

2. Remote actuation

   In addition, to sustain the advantages of the method that uses soft materials, remote actuation is frequently used in the wearable robot study. *Remote actuation* indicates an actuation method of locating actuators far from the end-effector. The system using remote actuation has advantages in reducing the complexity and impedance of the end-effector (Sporer *et al.* 2002). It is because, bulky and heavy components such as actuators, controllers, and batteries are not located in the end-effector in this design. Since the actuators are not located at the joint, additional components that transmit the mechanical work from the actuators to the joints are required. These are called as a *transmission* and frequently used transmission in the wearable robot is described at the next part.

3. Tendon transmission

   Tendon transmission is one of frequently used transmission in soft wearable robot because it maintains the softness of the robot. Also, by using the tendon, the robot size can be minimized because the tendon can transmit force even in a small cross-sectional area(Iannucci *et al.* 2018); Tendon can endure high tensile force even with a small cross-sectional area and has an ability to be adapted to external shape due to its high compliance. Also, the tendon transmission provides additional advantages (i.e, impact resistance and safe actuation) to the wearable robot (Grebenstein *et al.* 2012).

4. Under-actuation mechanism

   Although tendon-driven soft wearable robot has advantages in enhancing the usability, generating hand motion is still difficult problem to solve. It is because, the hand requires lots of actuators to cover lots of joints. Alternative method to reduce the actuator number is usually called as an *under-actuation mechanism*. To cover more joints than actuators, the mechanism are designed to apply certain constraints: kinematic constraint or kinetic constraint. Since the detail explanation could harm the overall flow of the thesis, details about the actuation characteristics of kinematic constraint or kinetic constraint are explained in chapter 3.

Similar to lots of engineering technologies, above techniques have some side effects as well; These side effects are explained in the section 1.2.

## 1.2. Problem Definition

In the soft robot with under-actuated tendon transmission, the side-effects could be organized as follow :

1. Friction

   The friction of the tendon depends on the tendon configuration; it occurs when the tendon path is bent. In the under-actuated tendon transmission, due to the fact that the tendon should pass through numerous joints to transmit the tension, the friction accumulates through the tendon routing. Details about the relationship between wire curve and friction in the under-actuated tendon routing is explained in the Appendix B. Increase of the friction, not only reduce the efficiency of the robot but also makes the robot hard to control. Also, the friction reduces the under-actuation performance and makes the robot vulnerable to the impact (Wensing *et al.* 2017).

2. Controllability

   Although the under-actuation mechanism enables to cover more joints with less number of actuators, it also has a limitation on the controllability. For instance, when three joints move by a single wire, it is impossible to control each joint position or torque independently. With the limited controllability, we can only generate limited posture or force (or torque) using an under-actuation mechanism.

By thinking deeply about the reasons of the above side effects, we can induce that these are originated from the fact that the hand wearable robot should be designed in a compact size. For instance, to reduce the friction at the wire, we can consider a method of using mechanical components such as bearings which easily remove the friction. However, it is not suitable in the soft wearable robot because usage of these rigid mechanical components deprive the advantages of soft wearable robot by increasing the overall size and weight. In a same manner, the controllability can be also increased by using more actuators but it makes the system bulky and heavy as well. The thesis paper is about proposing methods to solve the aforementioned side effects - without increasing the robot size and weight - in the hand soft wearable robot that contains under-actuation mechanism; In this thesis, we are going to call this problem as a *scalability issue*. Details about the method are in the next section 1.3.

## 1.3. Research Goal

The thesis contribution can be described by answering how the above two issues (i.e, friction and controllability) are solved in the proposed robot. In this thesis, for the friction issue, a novel actuator that contains the under-actuation mechanism is developed; Details are explained in the chapter 2 and the chapter 3. The actuator is named as *Slider-Tendon Linear Actuator* and it reduces both friction and complexity of the end-effector by containing the mechanism in itself.

For the controllability issue, on the other hand, the thesis shows a novel soft wearable robot named *Exo-Glove II*; This robot is designed to assist the thumb motions to make various hand grasp postures. By utilizing the actuator that is explained above (i.e, Slider-Tendon Linear actuator), it was possible to use only four actuators to assist thumb, index, and middle finger. The design process of the Exo-Glove II is explained in the chapter 4, and the method to find out the minimum number of actuators is expressed in this chapter as well. As it can be found in the chapter 5, it was possible to make various postures using the proposed robot and actuators. Before explaining the main text, the design framework for the Exo-Glove II is described briefly to clarify the contribution of the robot; The design framework is expressed as follow :

1. Target body part

   Since the wearable robot requires both usability and functionality which has conflicting aspects (i.e, the usability requires compact and light weight while the functionality requires lots of sensors and actuators), we have to think about the importance of the body function; This process requires in-depth understanding of biomechanics. For instance, when we are assisting human hand, the thumb is the most important body part to assist (Nanayakkara *et al.* 2017); Details about human hand anatomy and function are expressed in the Appendix A.2. The Exo-Glove II in this thesis have been developed to assist the thumb, index finger and middle finger.

2. Requirements

   After deciding the target body part, we have to consider the requirements of the chosen body part. In the case of the thumb, it is required to provide at least two degree of freedoms (DOFs) and this information can be also acquired by considering the biomechanics of the human body(Bunnel 1938; Li & Tang 2007). In Exo-Glove II, we decided to design the system with three DOFs to assist the thumb, index and middle finger.

3. Tendon routing

   After deciding the target body part and requirements of the robot, we have to think about how to design the overall tendon configuration. For instance, in our robot design, we are assisting nine joints (total 13 DOFs) using only three DOFs. Therefore, it is important to think about how each actuators are taking over numerous joints; It can be referred as an optimization problem for the under-actuation mechanism (Kim *et al.* 2018). One thing different from the conventional optimization under-actuation mechanism is that it is more complicated problem because the joint stiffness is not well defined and the Jacobians are non-linear matrices.

4. Performance factor

To find out the optimal tendon routing using the under-actuation mechanism, it is required to define the performance factor of the robot. (i.e, it can be considered as a cost function of the engineering problem.) In our case about assisting hand functions, we decided a concept of opposition workspace as a performance factor and it was possible to show that using four Slider-Tendon Linear actuators is sufficient to cover the workspace. Details about the opposition workspace are explained in the chapter 4.

In summary, this thesis propose a novel hand wearable robot named Exo-Glove II and the proposed robot assists the thumb motion for various grasp. Since a novel actuator named Slider-Tendon Linear Actuator is used in the robot design, it was possible to reduce the friction at the tendon and to design simple tendon routing. Also, the thesis propose a method to find out the minimal actuator number to function given tasks. As a result, by utilizing the Slider-Tenodn linear Actuator, the thesis shows Exo-Glove II which assists various hand motions with only four tendon driven actuator.

Details of the above contents are explained in the thesis as a following procedure. In chapter 2, we show how a novel tendon driven actuator has been developed; Unlike other papers, the development of the actuator precedes the overall contents of the robot because the method of solving the scalability issue of the under-actuation mechanism should be understood first to figure out the main contribution of the thesis; Following chapter, chapter 3, explains a design methodology of the robot‘s tendon routing with consideration of the developed actuator. As a next chapter, control method for the developed robot is depicted. Finally, discussion and conclusion of the thesis is explained in chapter 6.

# Chapter 2

# Tendon Transmission and Tendon Driven Actuator

## 2.1. Background

A tendon transmission has advantages in its ability to make the end-effector of a robot compact, simple, and safe, as compared to other transmissions such as linkage or gear transmissions; these advantages arise due to the compliance of the tendon transmission's wire (Ogane *et al.* 1996; T.Townsend 1988). A tendon transmission allows heavy components – such as the actuator, controller, and battery – to be located far from the end-effector through the use of a simple structure such as a Bowden cable. Therefore, tendon transmission has been widely used in soft wearable robots designed for disabled people with difficulties in daily life (Kang *et al.* 2019), patients in need of rehabilitation (Guo *et al.* 2018), soldiers in extreme environments (Panizzolo *et al.* 2016), and tired workers who have difficulty maintaining their posture (Park & Cho 2017). In these applications, soft wearable robots benefit from a simple, compact, and light end-effector and a design that moves some of the weight to locations where it can be more easily carried (Veale & Xie 2016).

To implement a tendon transmission in soft wearable robots, several methods have been proposed to pull the wire. One method is to use a linear actuator to pull and release the wire through the use of a moving a linear component (Ding *et al.* 2014). A ball screw is commonly used because it has high back-drivability, reliability, and accuracy. However, the actuator becomes bulky when the required stroke is long, since the traveling length of the linear component must be longer than the stroke of the wire. Furthermore, if the required tension increases, the actuator becomes even bulkier due to enlargement of the ball screw mechanism and the resulting increase in the cross-sectional area.

To minimize the size of the actuator, a spool can be used as an alternative to the linear actuator (Asbeck *et al.* 2015; Mao & Agrawal 2012; Chernyak *et al.* 2012; In *et al.* 2017). In this setup, the wire is pulled by winding it around a spool that is connected to a rotary motor. In this case, derailment of the wire around the spool can induce tangling failure; thus, tangling must be prevented. One way of preventing derailment is to use antagonistic actuation with pre-tension; this approach is widely used for traditional rigid robots (Grebenstein *et al.* 2012). In the soft robotic field, unfortunately, pretension could cause unwanted deformation of the structure. Therefore, the efficiency of the actuation could also be reduced (In *et al.* 2015; Kang *et al.* 2019). Recently, several soft wearable robots adopted an actuation method that uses a slack-enabling mechanism that incorporates rollers to prevent derailment, without applying pretension on the robot (In *et al.* 2015; Kang *et al.* 2019; Xiloyannis *et al.* 2016, 2017). Rollers sustain only the tension of the tendon inside the actuator (not the whole tendon) by applying friction on the tendon. Here, a single wire can be divided by rollers into two sections: a pretension section inside the actuator and a tension-free section outside the actuator. However, when the friction and slip between the wire and rollers is used for stable actuation, researchers are still struggling to overcome the low durability of the wire and rollers (In *et al.* 2017).

In wearable robot applications, both the size and reliability of the actuator are important factors that affect the performance of the wearable robot. The reliability of the actuator system affects the safety of the robot users, while the size affects portability and usability (Veale & Xie 2016). A ball screw is reliable, accurate, and back drivable; however, the size is bulky. On the other hand, a slack-enabling actuator is compact, but it is not reliable or efficient, because the mechanism utilizes the friction and slip between the wire and rollers. Since neither previous actuator used in wearable robots satisfies both design requirements, it is necessary to develop an actuator system that is suitable for soft wearable robots.

In this thesis, we propose a Slider-Tendon Linear Actuator (STLA) that is compact and reliable and offers various functionality enhancements for soft wearable robots. The proposed STLA utilizes a tendon-driven slider as a component that combines a spool and a linear transmission. Each side of the slider is connected to two different tendons: a motor tendon and an end-effector tendon. Here, the motor tendon, the wire that is being wound around the spool, pulls the slider and the slider pulls the end-effector tendon, the wire that is connected to the end-effector, as shown in Figure 2.2. Also, two springs are installed at the slider parallel to the end-effector tendon to generate slider movement toward the end-effector, since the motor tendon can only pull the slider. The tendon-driven slider with springs and two separate tendons (i.e., the motor tendon and the end-effector tendon) offer the following contributions.

1. This design reduces actuator size, as compared to a ball screw linear actuator. It has a small cross-sectional area, since the tendon is strong at resisting a tensile force. The tendon-driven slider can only pull the end-effector tendon. The fact that the slider can only generate force in a single direction is not a problem, since the tendon transmission inherently transmits only the tensile force.

2. The proposed approach has two advantages in reliability and durability, as compared to the use of a slack-enabling mechanism. First, no pretension is applied to the end-effector tendon, which is important for soft wearable robots. This advantage is easily achieved from the inherent nature of the proposed method, which decouples the tendon routing into the motor tendon and the end effector tendon. Second, derailment of the motor tendon around the spool can be prevented without applying friction. This is made possible through springs installed on the slider. Since the spring is serial to the motor tendon but parallel to the end effector, tension can be applied only to the motor tendon.

3. Use of the slider enables the addition of other features (Veale & Xie 2016) that improve maintenance, efficiency, operability, and portability of wearable robots. As shown in Figure 3, without increasing the size or complexity of the actuator system, STLA contains the following features in a single actuation unit: (1) an under-actuation mechanism that enhances the simplicity and adaptability of the robot without complex control, (2) a tendon connector that increases portability and eases maintenance, and (3) a stroke amplification

method that helps to keep the size of the actuator small while generating a long wire stroke. Further details regarding each of these actuator features are explained in the following section.

As a result of utilizing a tendon-driven slider, the size of the STLA is reduced to 24.6% of the size of a ball screw linear actuator. Furthermore, derailment prevention with a spring, rather than rollers, increases the reliability and durability of the wire. These increases are enabled because tensile force is applied on the wire, rather than friction and slip. In addition, adding features in the actuator, rather than the end-effector, not only increases the simplicity of the end-effector but also improves the performance of the feature itself. By placing components in the actuator, useful mechanical components can be used in the STLA while maintaining simplicity, softness, and usability of the end-effector.

chapter 2.2 provides details about how the additional proposed features improve the robot, how the STLA is implemented, and how performance is improved without increasing the complexity of the end-effector. After this explanation of the STLA, a detailed design process is explained in chapter 2.3 to inform decisions about mechanical components. Next, chapter 2.4 describes how STLA is adapted to a soft wearable robot called Exo-Glove II, and STLA performance is verified. Finally, chapter 2.5 provides a discussion and offers conclusions.

## 2.2. Working Principle of The Actuator

This section explains the working principle of the proposed STLA. The STLA contains the following four functions to satisfy requirements of the actuator needed for a soft wearable robot. In addition, since these functions can all be implemented through a single linear motion, the size of the actuator does not increase, as shown in Figure 2.3. This section explains the methods used to implement each feature listed below, including: 1) wire derailment prevention, 2) the under-actuation mechanism, 3) the tendon connection, and 4) stroke amplification.

### 2.2.1. *Wire derailment prevention*

For derailment prevention, an internal spring is installed in the STLA. The main principle of the derailment prevention is to connect the spring at the middle of the tendon. Using this connection method, part of the tendon, the tendon that will be wound around the spool, is connected in series with the spring; the other part is connected in parallel with the spring. Since the pretension of the spring only affects the serially connected tendon, it is possible to make an actuator that prevents derailment without applying pretension on the end-effector. The tendon-driven slider in the STLA is the main component that connects the spring, as noted above. The slider divides the wire into the motor tendon (blue, broken line in Figure 2.3 (b)) and the end-effector tendon (yellow, solid line in Figure 2.3 (b)). The motor tendon only exists inside the actuator and the end-effector tendon is connected both to the end-effector and to the actuator. When the spool winds the motor tendon, the slider moves toward the spool and the internal spring elongates. In the unwinding step, the internal spring pulls the slider and the motor tendon back in the opposite direction. Therefore, the spring works to prevent the motor tendon from losing tension even in the unwinding process.

The tendon-driven slider, a component used to apply pretension on the motor tendon, not only decouples the tendon, but also serves as a transmission, which affects the tension and linear speed of the end-effector tendon. The relation between the motor dynamics and the end-effector tendon dynamics can be described by the following equations:

$$T_{end-effector} = (n_m \epsilon_M / n_e R)\tau_M - kx = (\epsilon\epsilon_m)\tau_M - kx \qquad (2.1)$$

$$V_{end-effector} = (n_e R / n_m \epsilon_M) w_M = (\epsilon\epsilon_M)^{-1} w_M \qquad (2.2)$$

$$\tau_{impact} = (n_e R / n_m) F_{impact} = \epsilon^{-1} F_{impact} \qquad (2.3)$$

where $T_{end-effector}$, $V_{end-effector}$, $\tau_{impact}$ represent the tension of the end-effector tendon, velocity of the end-effector tendon, and the impact applied to the motor, respectively. $\epsilon$ in the equation is a force transmission ratio defined by the number of bearings at the end-effector tendon and at the motor tendon. Since the spring is connected to the actuation unit, the tension produced by the motor results in a loss as much as the elastic force. Also, it is possible to prevent the motor from being broken from the impact because the number of movable pulleys affects the impact torque, as shown in Eq 2.3. All variables used in equations in this paper, including the equations above, are described in Table 2.1.

### 2.2.2. *Under-actuation mechanism*

An under-actuation mechanism simplifies the robot system in a manner that uses fewer actuators than the number of joints (Kang *et al.* 2019; In *et al.* 2015). Also, the mechanism enables the robot to make adaptive motion without complicated control (Dollar & Howe 2010; Jingdong *et al.* 2006; Lalibert 2008). Therefore, this mechanism has been adapted in several wearable robots to make robots adaptable without increasing complexity (Kang *et al.* 2019; In *et al.* 2015). We also implemented this mechanism inside the STLA to make the actuator more suitable for a wearable robot.

In a tendon transmission, a wire path that uses a movable pulley is the most common method used to realize the under-actuation mechanism, as shown in Figure 2.4 (b) (Birglen & Gosselin 2006). In this case, the mechanism requires a relatively large volume because of the space that the linear guides need for the pulley to move. To address the size issue, another tendon routing using fixed pulleys was proposed, as shown Figure 2.4 (a) (Kang *et al.* 2019; Catalano *et al.* 2014). In the tendon routing shown in Figure 2.4 (a), neither end of the wire is fixed at the end of the link; instead, it passes through the end of the link and goes to another link. The wire is not fixed to link A or B as is done conventionally; instead, it passes from segment 4 to segment 1 and both ends of the wire are fixed to the motor, as shown in Figure 2.4 (d). Although this method does not require linear space for a movable pulley, the system is not simple because three pulleys are required. Further, the friction is relatively large because it is applied on the wire in all curved paths and is accumulated through the paths. In soft wearable robot research, conduit-type components, such as Teflon tubes, are used as an alternative to minimize the size for this routing method; however, the friction applied on the wire increases exponential to the curved angle, as outlined in the capstan equation described in (Palli & Melchiorri 2006; Kaneko *et al.* April, 1991). The increased friction reduces several performance measures, including durability, adaptability, efficiency, and control performance. Therefore, a method is required that reduces the friction, while maintaining a compact mechanism size.

This issue can be solved by containing the mechanism in the STLA without size increases, because the tendon-driven slider in the STLA is already designed to move along the linear guide. By containing the movable pulley in the STLA, as shown in Figure 2.4 (c), the end-effector can be simple compared to a tendon routing that uses fixed pulleys. Also, the friction applied on the wire can be dramatically reduced.

2.2.3. *Tendon connection*

A tendon connector, a component that enables separation of the end-effector from the actuator, has been adopted in several wearable robots (Madson 2013; Nilsson *et al.* December, 2012; Kim & Park 2018). A tendon connector is an important component because it maximizes the portability and ease of replacement; this is essential for the actuation techniques used in human assist robots (Veale & Xie 2016). When the end-effector is detached from the heavy components, the end-effector can be more easily carried. Moreover, a tendon connector allows the wearable part to be easily washed, because the non-waterproof components, such as the actuator and controller, can be easily detached. However, a tendon connector also has a size issue because most of the connectors have been developed using a rigid structure with a linear guide that harms the softness, volume, and weight. The size issue of the tendon connector can be solved by using the STLA in a same manner that the STLA solves the problem of the conventional under-actuation mechanism, as Figure 2.5 shows. Components inside of the green dotted line in Figure 2.3 play the role of the tendon connector. Since the tendon-driven slider in the STLA was originally designed to slide linearly along the actuator, adding the function of a tendon connection can be established by just making space for the tendon connector.

2.2.4. *Stroke amplification*

Although the STLA is designed to be compact, by containing several functions in a single linear unit, the actuator size increases as the required stroke increases. This is because all functions of the STLA require linear motion with a longer drive distance than the wire stroke. Additional pulleys are used as movable pulleys in the STLA design to reduce the size of the actuator, as shown in Figure 2.6. By adopting movable pulleys, the wire stroke ($D_s troke$) increases as the number of movable pulleys increases, as shown in Eq 2.4 . Therefore, the overall actuator length ($L_t$) reduces as the number of movable pulleys increases. However, an appropriate number of movable pulleys should be used, since use of the pulley also increases the cross-sectional area of the actuator. The method to induce an appropriate number of movable pulleys is described in more detail in the next section.

$$2n_e(L_t - l_{sta}) = D_{stroke} \tag{2.4}$$

## 2.3. Modelling and Mechanical Design

Section 3 explains the process used to select appropriate components for the STLA. For the modelling, we chose a soft wearable robot for a certain application for a specific body part, because it is necessary to know the requirements to fix the mechanical components. Our target application was determined to be the Exo-Glove II. The application, Exo-Glove II (shown in Figure 2.1), is a wearable robot designed to assist a hand-paralyzed person in their activities of daily living. The Exo-Glove II has been developed to assist flex motion of the index and middle finger with a single wire using an under-actuation mechanism (Kang *et al.* 2019).

Since the Exo-Glove II generates motion with a single wire, the actuation requirement can be summarized by the tension, stroke, and pulling speed of a single wire. The Exo-Glove II requires a 100mm stroke and 80N tension to assist with grasping in daily life (Kang *et al.* 2019). Further, the requirement for the pulling speed of the wire is set to be 25mm/s because the design goal of the Exo-Glove II is to assist with a grasp in 4 seconds. Considering the safety factor, the target requirements of the actuator are set to be 120mm stroke, 100N tension, and 30mm/s pulling speed, as summarized in Table 2.2. With the given requirements of the Exo-Glove II, each component in the proposed STLA is determined to increase the efficiency and to minimize the size of the actuator.

### 2.3.1. *Design of components in the STLA*

1) Design of a movable pulley to reduce the size of the STLA

Based on the required stroke of the Exo-Glove, the actuator size is determined by choosing the number of movable pulleys used in the STLA. When the number of movable pulleys is increased, the actuator length is reduced; however, the cross-sectional area of the actuator increases, as shown in Eqs 2.5 – 2.6. We determined the number of movable pulleys as two in our design because this choice showed the smallest size when using the selected motor. The arithmetic-geometric mean of the number of movable pulleys ($n_e$) enables optimization of the actuator volume, as the following equations show. However, the optimal number of pulleys is obtained inductively, rather than deductively, because determining the initial size of the actuator is complicated to solve deductively. This is because the size of the actuator varies depending on the design.

$$L_t = l_{sta} + D_{stroke}/2n_e \ (\because 2n_e(L_t - l_{sta}) = D_{stroke}) \qquad (2.5)$$

$$A_t = A_{motor} + n_e a_e \tag{2.6}$$

After determining the number of pulleys, to show that the movable pulleys are effective to reduce the size, the size of the STLA is compared with other actuators, such as a ball screw linear actuator, a slack-enabling actuator, and an STLA that does not use movable pulleys. Several assumptions are used in the size comparison. First, we only estimate the size of the actuation unit; the motor size is excluded to allow more equitable comparison. Second, each size of the actuation method is compared by calculating the volume of the smallest cube that surrounds the actuation unit. Each volume is calculated by multiplying the cross-sectional area and height. Third, the gap between each mechanical part ($d_{gap}$ in the Figure 2.7) is set as 1mm. Fourth, estimation is carried out by considering the larger part when several parts are placed in parallel. For example, the length of the actuation unit with a ball screw ($L_{BS}$) is determined by the length of the longer part among the ball bushing and ball screw because the ball bushing and the ball screw are placed in a row, as shown in Figure 2.7 (a). The function max is used to express the above situation as shown in Eq 2.10. Lastly, the size of the STLA is estimated without considering its ability to include the under-actuation mechanism or the tendon connector; this enables fair comparison because the other actuation unit also doesn't contain these functions.

In the size estimation of the actuation unit with the ball screw, the volume is calculated using the smallest ball screw among commercially available products; this is named "MDK-0401-3" because the ball screw is a commercial product (Thomson Industries Inc. 2013; THK 2017). The schematic of the actuation unit with the ball screw is shown in Figure 2.7

(a). Since the given ball screw requires an additional linear ball bushing for the linear motion, the size of the actuation unit with the ball screw is estimated by including the space needed for the bushing, which is depicted in gray in Figure 2.7 (a). Two bushings are used because the flange of the ball screw must be designed to have force equilibrium to minimize friction. For fair comparison, the STLA design also includes two linear ball-bushings of the same size used in the ball screw size estimation. One unusual aspect exists in this case unlike other size estimations. Since the ball screw has different lengths in horizontal ($T_{bs}$) and vertical directions ($D_{bs}$), the size of the ball screw is estimated by using the smaller value among $\mathrm{A}_{BS_{ver}}$ in Eq 2.7 and $A_{BS_{hor}}$ in Eq 2.8, as shown in Eq 2.9. Actuator size can be estimated using Eq 2.11, with the design parameters shown in Table 2.3.

$$A_{BS_{ver}} = T_{bs}(D_{bs} + 2D_{bush} + 4d_{gap}) \tag{2.7}$$

$$A_{BS_{hor}} = D_{bs}(T_{bs} + 2D_{bush} + 4d_{gap}) \tag{2.8}$$

$$A_{BS} = min(A_{BS_{ver}}, A_{BS_{hor}} \tag{2.9}$$

$$L_{BS} = max(L_{BS}, L_{bush}) + 2d_{gap} \tag{2.10}$$

$$V_{BS} = A_{BS} * (D_{stroke} + L_{BS}) = 481(D_{stroke} + 13) \tag{2.11}$$

In the case of the slack-enabling mechanism, the size of the mechanism is determined by the feeder, idler, and spool. Since the slack-enabling actuator is not a commercial product and its size estimation was done in previous research, we used the values from the previous research, as shown in Eq 2.12 (In *et al.* 2017). As the equation shows, the size of the slack-enabling mechanism barely increases as the required stroke increases.

$$V_{SEA} = 264(0.018D_{stroke} + 5.4) \tag{2.12}$$

]par Lastly, for the case of the basic STLA ($STLA_B$), the sliding tendon actuator that does not use stroke amplification, the size of the actuation unit is derived using the schematic shown in Figure 2.7 (b). The size of the $STLA_B$ is estimated as following. In the $STLA_B$ size estimation, $L_{STLA_{B-final}}$ is relatively complicated since the space to fix the spring should be considered. Since the spring is fixed both at the slider and at the wall, the length of the wall and the $STLA_B$ must be considered in the estimation, as shown in Eqs 2.17 – 2.18. However, if the length of the spring is longer than the sum of the length of the wall and the length of the slider, the length of the spring will affect the volume; the length of the entire actuation unit is expressed as shown in Eq 2.16.

$$V_{STLA_B} = (L_{STLA_B} + D_{stroke}) * d_{STLA_B} * h_{STLA_B} \tag{2.13}$$

$$h_{STLA_B} = (2d_{gap} + max(D_{bush}, D_{spring})) \tag{2.14}$$

$$d_{STLA_B} = (D_{spring} + 2D_{bush} + 4d_{gap}) \tag{2.15}$$

$$L_{STLA_{B-final}} = max(L_{wall} + L_{STLA_B}, L_{spring} + 2d_{gap}) \tag{2.16}$$

$$L_{STLA_B} = 2d_{gap} + L_{bush} \tag{2.17}$$

$$L_{wall} = 2d_{gap} + d_{sp_{fix}} \tag{2.18}$$

To show the effect of the additional movable pulley, we also obtained the size of the actuator that arises from using an STLA with two movable pulleys, as shown in Figure 2.3 (b). The size of the STLA is estimated as follows. Since two movable pulleys are used, 0.25 is multiplied by the stroke of the wire in the final volume estimation.

$$V_{STLA} = (L_{STLA_{B-final}} + 0.25D_{stroke})d_{STLA}h_{STLA} \tag{2.19}$$

$$d_{STLA} = max(3D_{bearing} + 2d_{gap}, 2D_{bush} + D_{spring} + 4d_{gap}) \tag{2.20}$$

$$h_{STLA} = (3d_{gap} + max(D_{bush}, D_{spring}) + h_{bearing}) \tag{2.21}$$

$$L_{STLA_{final}} = max(L_{wall} + L_{STLA}, L_{spring} + 2d_{gap}) \tag{2.22}$$

$$L_{wall} = max(D_{bearing}, d_{sp_{fix}} + 2d_{gap}) \tag{2.23}$$

$$L_{STLA_B} = 2d_{gap} + max(L_{bush}, D_{bearing}) \tag{2.24}$$

With the actual size of the component, the size of the STLA and $STLA_B$ can be estimated using Eqs 2.25 – Eq 2.26. One note is that a single spring was included in the STLA size estimation; however, two springs are used in the actual design, as Figure 2.3 shows. This is because it is more compact to attach springs to both sides than to connect a spring at the center when the motor or tendon connector is considered. Since the assumption in this estimation is to ignore the effect of the tendon connector or motor, the size is estimated using a single spring.

$$V_{STLA-B} = 162(D_{stroke} + 32) \tag{2.25}$$

$$V_{STLA} = 312(0.25D_{stroke} + 32) \tag{2.26}$$

Using the equations above, the volume of each actuator component can be compared, as shown in the graph in Figure 2.8. When the required stroke is 240mm, the size of the STLA is 24.67% that of the ball screw linear actuator. It is true that the required stroke of the actuator is set to be 120mm; however, we compared the size at 240mm so as to not to consider the under-actuation, as mentioned above. Although the size of the STLA is small, the volume is 10.64 times bigger than the conventional slack-enabling actuation unit.

2) Design of the spring to enable a sufficient releasing speed

The other component that is important for the actuator performance is the internal spring used for derailment prevention. When the spring coefficient is too low, wire can be derailed from the spool because the slider can move slower than the spool rotation speed. On the other hand, when the spring coefficient is too high, the actuator efficiency is reduced because the tension of the end-effecter tendon is the difference between the tension of the motor tendon and the spring force, as Eq 2.1 shows. Therefore, we obtained the optimal spring coefficient to prevent slack in the wire. The equation of motion of the slider in the STLA is shown as Eq 2.27. The range of motion of the slider is set to -$D_{stroke}/n_e$ to 0. With the relationship between x and t in Eq 2.28, the spring coefficient k is chosen to make $t_released$, estimated releasing time of the slider, to be less than four seconds; The releasing time is determined by a requirement of the Exo-Glove, as shown in Table 2.2. The desired spring coefficient is obtained using the friction coefficient of the bushing specified on the data sheet (0.01) and the mass of the slider, as directly measured (30.4g).

$$m\ddot{x} = \mu_{bs} m_s g + T_0 = kx + f_{ext} \tag{2.27}$$

$$x(t) = (-D_{stroke}/n_e - f_{ext}/k)e^{(-\sqrt{(k/m_s t)})} + f_{ext}/k \tag{2.28}$$

$$f_{ext} = T_0 - \mu_{bs} m_s g \tag{2.29}$$

$$(x(0) = -D_{stroke}/n_e,\ x(t_{released}) = 0) \tag{2.30}$$

$$t_{released} = \sqrt{m/k} ln(1 + kD_{stroke}/n_e f_{ext}) < 4(sec) \tag{2.31}$$

$$k_{desired} \geqslant 0.00544 N/mm \tag{2.32}$$

Finally, the spring constant was selected as 0.02 N/mm, considering the safe factor of three, to have enough releasing speed.

2.3.2. *Final actuator design with optimized components*

Using the components chosen as outlined in the previous sections, the final actuator is obtained after selecting the spool size and motor. First, the power of the motor is selected by considering the requirements for tension and wire speed. In this study, a 8.5W motor (Faulhaber, 2224SR, $\phi$ 22mm, Length 24mm) is selected to achieve the required tension and speed. The motor length is 58.7mm when the gearbox is attached. Second, gear ratio and spool size are determined because these variables are all related to the force-speed relationship. We first determined the diameter of the motor spool because the size of the spool is related to the impact torque applied to the motor and the reliability of the wire. When the motor spool size is reduced, the external impact force applied to the wire is transmitted to the motor with small torque. Therefore, it can be prevented from damaging motor when impact force is applied on the wire. However, if the size of the spool is too small, it will promote wear of the wire, thus, the spool size must be kept in a proper size to prevent wear. The size of the motor pulley is determined to be 5mm in diameter, so as to not bend the wire; this was determined using the equation defined in previous research (Horigome *et al.* 2018*a*; Horigome & Endo 2016). After diameter selection, the gear ratio is chosen as 69:1 and final wire tension, pulling speed, and stroke are calculated as 161.49N, 62.22mm/s and 248mm, respectively. When the actuator is assumed to perform an under-actuation function, the wire at both ends has a performance of 161.49N, 31.11mm/s, and 124mm because the actuator pulls in both directions, as summarized in Table 2.4. Motor and the gear efficiency are calculated as 0.8 and 0.69.

The STLA has two movable pulleys to minimize the volume. The internal spring has a spring coefficient of 0.02N/mm, as summarized in Table

2.4. Using the components with the above values, the actuator was developed as shown in Figure 2.9. The final size of the actuator is 35mm height, 112.9mm length, and 34mm width. The actuator size is relatively large compared to the estimation in the previous section, because additional components are included in the actuator. Specifically, a single loadcell (LSB200, Futek, USA) and the additional space to fix the Bowden cable are included in final actuator. All actuation characteristics are verified in the next section.

## 2.4. Simulation and Performance

In this section, we show whether or not the final actuator design satisfies the robot requirements through both simulation and experiment. First, experiments that measure the tension and speed of the wire are conducted. Next, a second experiment that shows the effectiveness of the under-actuation mechanism is conducted.

### 2.4.1. *Validation of the actuator speed*

The STLA contains springs that have a spring constant of 0.02N/mm. First, we measured the speed of the slider to check whether the selected spring works well. This is because that the wire speed is related to the slider speed, rather than the rotational speed of the motor. To measure the speed of the slider without affecting the actuation, captured video is analyzed by Matlab (Mathworks, Natick, MA, USA). The real position of the slider and estimated position using the motor encoder data are compared, as shown in Figure 2.10 (a). Since the tension increases after contact in our application, this experiment was conducted in a no-load condition. The tension begins to increase only at the last moment when it contacts the object; thus, the experiment under a no-load condition does not differ from the actual situation. The blue dotted line in the graph shows the estimated position of the slider calculated with the encoder data and the black solid line means the measured position of the slider using video analysis. The RMS error between the estimated and real position is 4.01%. After the speed experiment, tension of the wire is also measured using the loadcell. Since the STLA contains an under-actuation mechanism, tension of both ends of the wire is measured. The force properties results are depicted in Figure 2.10 (b). As a result, the tension at each wire sufficiently reaches the requirements of the application, and the tension difference between the two wires is small. In this experiment, the root mean value of the tension difference is 0.78N.

#### 2.4.2. *Simulation and validation of the under-actuation mechanism*

In the previous section, we explained two under-actuated tendon routings, as depicted in Figure 2.4. Although routings are designed to have the same function, which applies the under-actuation mechanism on the two-link system, the tension distribution shows a difference due to the difference of path and the routing components (pulley, Teflon tube, etc.). When the wire path is linear, the friction is barely applied because the normal force also does not generate. However, when the tendon passes through the curved structure, normal force increases proportional to the tension of the tendon. Here, friction is defined by the capstan equation that relates the tension to the friction force. Also, the routing component changes the friction by affecting the friction type. When a fixed component such as a Teflon tube is used, the relative movement between the wire and the routing component always exists, inducing the kinetic friction. On the other hand, in a case that uses rotating components, such as bearing and spool, rolling resistance is applied for the calculation. Therefore, the friction force can be differently defined. The friction coefficient of the Teflon tube and the bearing are 0.05 and 0.001, respectively, in the modelling (In *et al.* 2015).

By extending the content above about friction to the whole tendon routing, the overall tension distribution can be derived by considering the direction of the wire movement, friction coefficient, and the elongation of the wire. To do so, we simplified the tendon routing in the finger to the routing shown in Figure 2.11 (a) and (b). The wire is divided into six segments in the tendon routing using fixed pulleys; two segments at the actuator side (a, b), and four segments at the end-effector side (1 to 4). The upper block in the figure refers to link A (finger A in the wearable robot application) and is assumed to have contact with the external environment, while link B (finger B in the wearable robot application) that is depicted as the lower block is assumed to move freely.

In the tendon routing that uses fixed pulleys, as shown in Figure 2.11 (a), the wire at segment a and b will be wound around the spool amount of $R\theta$ ($R$ means spool radius), respectively, when the spool rotates an amount of $\theta$. As block A does not move, the length of segments 1 and 2 does not change, while the lengths of segments 3 and 4 decrease in the amount of d when block B moves an amount of d. Then, it is obvious that the traveling length of the lower block (d) is equal to the wound length of the spool ($R\theta$), which is described as Eq (2.34). The notation used in this equation is depicted in Figure 2.11 (a).

$$2(l_{out} + l_{in}) - 2R\theta = l_{out} + l_{in} + (l_{out} - d) + (l_{in} - d) \tag{2.33}$$

$$R\theta = d \tag{2.34}$$

In this tendon routing, the wire at the segment 3 will move to segment a by passing through segments 2 and 1. This is because the lengths of segments 2 and 1 don't change, while the length of the segment 3 is reduced. On the other hand, the wire at segment 4 directly moves to segment b. The aspects of the movement of the end-effector wire when the motor pulls the wire can be depicted as the arrow in Figure 2.11 (a). In this case, one unusual aspect is presented: there is no movement in wire between segments 3 and 4. Here, the additional assumption that the wire elongates when the tension increases is used to consider the movement. Using this assumption, we envision that the elongated wire in segment 3 moves to segment 4. Using the above information about the direction of movement of the wire, the total tension distribution can be obtained as shown in Table 2.5.

In addition, we defined the concept of transmission ratio, a ratio of the pulled length of the wire by the actuator to the moving distance of the link, to obtain the relation between the motor torque and the fingertip force using the virtual work principle. The routing system with fixed pulleys has a transmission ratio of 1:1 because the wound length of the wire is equal to the traveling distance of the lower block, as Eq 2.34 shows.

When the under-actuation is implemented with the movable pulley, as in Figure 2.11 (b), the wire can be divided in to four segments; two segments in the motor part (a and b) and two segments in the end-effector part (1 and 2). Here, the wire in segment 2 moves to segment a after passing segment b. The wire at segment 1 does not move because link A does not have movement. However, when we assume elongation of the wire, the wire at segment 1 also moves to segment a. In this case, the transmission ratio is 2:1 because the link moves twice the length of the wire wound by the spool. The tension relationship between each segment and the final tension distribution is derived as shown in Table 2.6.

Experiments to validate the under-actuation performance are conducted as shown in Figure 2.12. The overall appearance of the experimental setup is shown in Figure 2.12. To create a situation in which the link moves slowly with increasing wire tension, springs are connected to each link; link A is blocked by the block to assume contact. Four load cells are used to measure the segmental tension of a single wire divided into segments. Figure 2.12 (a) and (b) each show the tendon routing of under-actuation that use a Teflon tube and movable pulley, respectively.

To measure the tension, a tension meter is designed, as shown in Figure 2.12 (c), by referring to the conventional method of measuring the tension. Experimental equipment includes a wire curve unit to reflect the change in the wire path caused by finger bending; the curve unit is designed as shown Figure 2.12 (d). Inside the curve unit, the Teflon tube is installed at a certain bending angle. The finger bending angle can be considered by replacing the unit that curves at different angles. The tension meter is located after the wire curve unit because a measurement of how much force the wire transfers to each finger is a goal of the experiment.

Using the experiment setup introduced above, the tension distribution of the tendon routing using fixed pulleys and the routing using movable pulleys are each obtained, as shown Figure 2.3. $F_A$ and $F_B$ each mean the force applied on two fingers; the 1 to 4 notations in the tendon routing using fixed pulleys refer to the tension at the wire segment that is introduced in Figure 2.1. In this experiment, we found that the difference between FA and FB is 15.1N when the fixed pulley is used, while the difference of the two fingers is 0.2N when the movable pulley is used. Here, the experiment was conducted until the sum of the forces applied to finger B reached 100 N.

The experiment described above was conducted when the curve angle of the wire curve unit was 0 rad, which means that the finger is fully extended. The experimental results of measuring the difference in the force of the fingers according to the variation of the bent angle is shown in Figure 2.13 (b). The routing using fixed pulleys shows that the difference in force applied to the two fingers increases as the angle of bending of the finger increases. On the other hand, in the case of under-actuation using a movable pulley in the STLA, it can be found that the difference in the force does not cause a significant change as the bending angle of the finger changes.

## 2.5. Discussion & Conclusion

Tendon-driven soft wearable robots have been developed to take advantage of a design that makes the end effector more compact, light, and simple. However, a tendon transmission requires special care so as to not induce high friction and such that the wire does not become tangled around the spool. To address these issues, researchers have applied additional functions to the tendon transmission, such as a pre-tension mechanism or a slack-enabling mechanism. Other techniques, such as using an under-actuation mechanism or a tendon connector, have also been proposed to simplify and minimize the end-effector. In this paper, we proposed a Slider-Tendon Linear Actuator (STLA) that uses a tendon-driven slider. Utilizing the tendon, rather than a ball screw, for the slider motion reduces the actuator size. Springs inside the STLA enable stable actuation of the tendon-driven slider. The STLA contains an under-actuation mechanism to reduce the number of actuators, a tendon connector to improve portability, and a stroke amplification mechanism to reduce the size of the actuator. The proposed STLA not only simplifies the end-effector, it also improves the performance of the robot. Performance is improved due to the STLA's easy-to-use mechanical components; reduced mechanical components in the end-effector also result in increased wearability, simplicity, and compactness.

It should be noted that the durability of the proposed actuator may be less than that of a conventional ball screw transmission. However, although durability is of course important, the STLA's durability will be sufficient if its durability is higher than the durability of the Bowden cable. Since the wire slips at the Bowden cable, it is obvious that the durability of the actuator is higher than that of the Bowden cable. Because the STLA offers advantages in size, we can conclude that the STLA is more suitable for soft wearable robots. Moreover, the proposed actuation method has additional minor advantages that are not explained in detail in this paper. First, the actuator is inexpensive because it consists of two bushings and two springs. Second, the actuator can be easily customized to meet the requirements of a particular robot by changing the motor spool size, the number of pulleys, and the gear ratio. In addition, the STLA can be a good solution for high-impact situations by reducing the radius of the spool and increasing the number of pulleys on the motor side. By changing these parameters, damage to the motor from a large impact can be avoided.

The size of the proposed STLA is 24.67% the size of a ball screw and 10.64 times bigger than a slack-enabling mechanism. However, the durability of the slack-enabling actuator is not sufficient to for many practical applications, since it uses friction and slip for derail prevention. Also, the slack-enabling actuator does not have space for the linear motion, which makes it difficult for it to adopt additional functions, such as tendon connecting and under-actuation.

The STLA also has the potential to contain other components used in other research about tendon transmissions with rotary motors. First, the actuator can increase the peak tension by using a compliant material. By adding a compliant component that accumulates spring energy in the unwinding process and emits energy in the winding process, we can increase the maximum tension without using a high-torque motor. Also, research of adding an extra spool in parallel to the existing spool can be pursued. In this design, the actuator can pull two wires, even using a single motor. Therefore, we can make the actuator apply bi-directional force as a dual slack-enabling actuator, as shown in previous research (In *et al.* 2017). Other research related to changing the radius of the motor spool can also be used in the STLA. This research uses a motor spool as a transmission. It generates high tension by decreasing the radius of the motor spool and generates high speed by increasing the radius of the spool (Xu *et al.* 2018).

The proposed actuator will require additional research about the type of wire. The wire used in the proposed actuator is Dyneema, because this wire has high yield strength. However, the wire used in our work has high hysteresis, which is not preferred in force control. Therefore, the best wire to be used in the actuator should be chosen based on future work. Additional research should also be performed to increase the performance of the tendon transmission. Friction and the wear of the wire is one of the main disadvantages that leads many researchers to hesitate to use a tendon transmission. In future work, a wear monitoring system can be proposed for the STLA. By measuring and comparing the tension at the end-effector and on the actuator side, the system can observe the tendon wear. As a long-term goal, we are eager to make the tendon transmission a compact, safe, and reliable transmission to be used in human assist robots by adding more functions to the STLA proposed here.

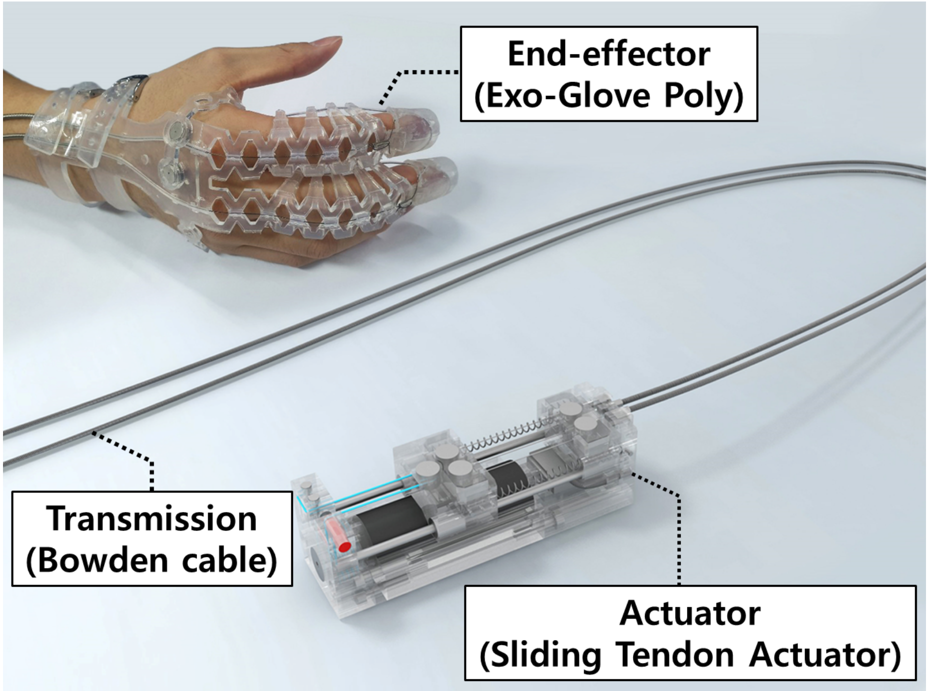


**Figure 2.1: Overview concept of a tendon transmission that uses a Bowden cable.**

By locating the heavy components such as the actuator, battery, and controller far from the end-effector, the end-effector can be light, compact, and simple. By concentrating the application of the actuator only on the tendon transmission, STLA has optimized performance and includes functions such as tendon connection, under-actuation mechanism, and stroke amplification.

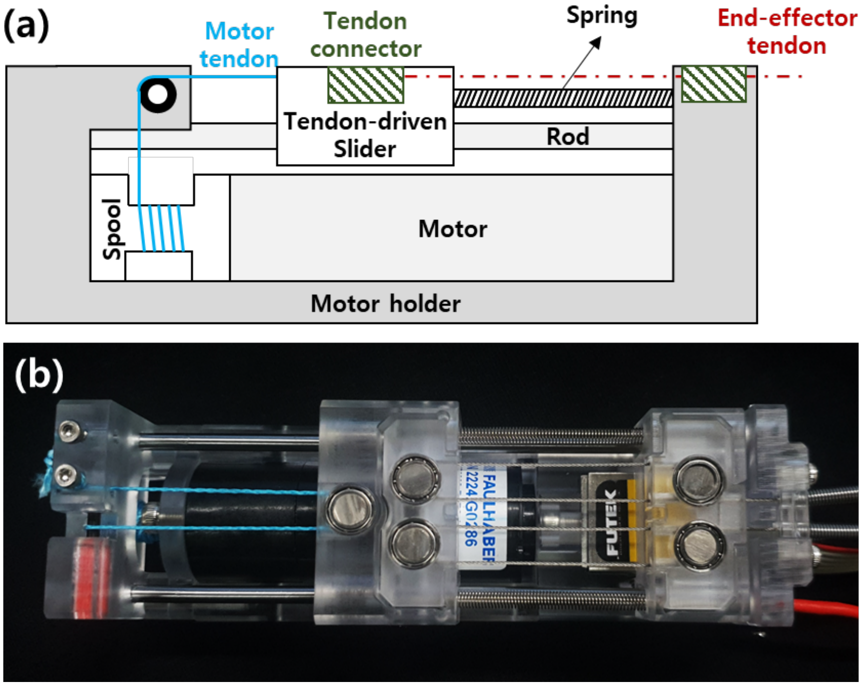


**Figure 2.2: Overview of Slider-Tendon Linear Actuator (STLA)** By utilizing a tendon-driven slider, STLA shows compact size and reliable actuation performance. **(a)** shows side view of the schematic and **(b)** shows top view of the real actuator. STLA pulls the end-effector tendon (red dotted line) by winding the motor tendon (blue solid line) that pulls the slider. To release the end-effector tendon, the spool unwinds the motor tendon and springs pulls the slider and motor tendon.

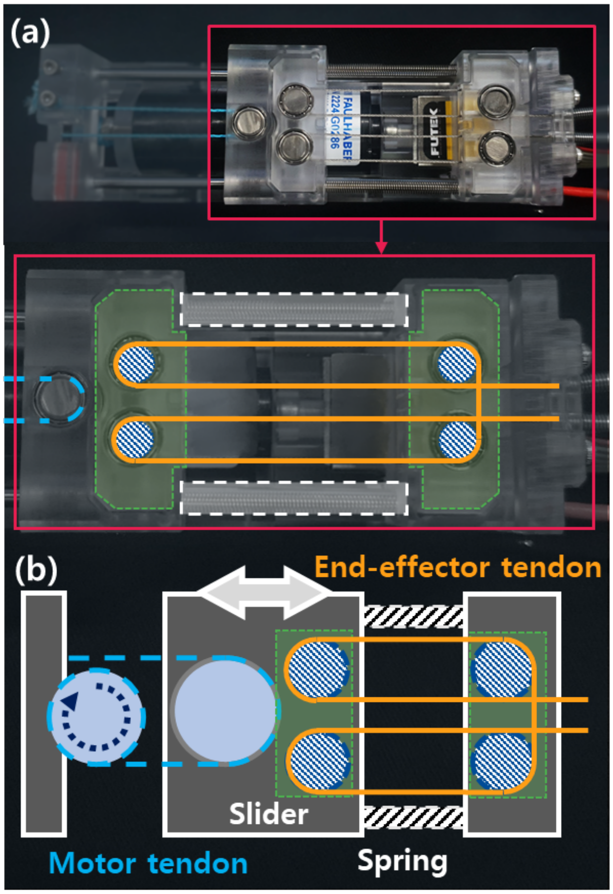


**Figure 2.3: Details of the STLA working principles.**

The actuator offers the following four functions in a single slider. 1. Derailment of the motor tendon is prevented by springs (white broken line). 2. Under-actuation is implemented to the end-effector tendon using a movable pulley in the slider (dark blue hatched circle). 3. The tendon connector makes the end-effector separate from the actuator easily (green dotted line). 4. The stroke of the tendon is amplified by designing the tendon routing (yellow solid line).

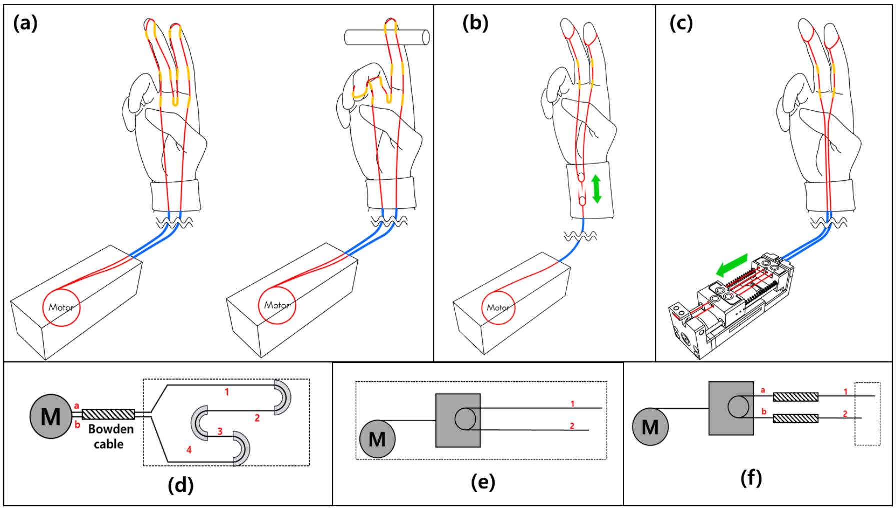


**Figure 2.4: Methods to apply tendon-driven under-actuation mechanisms in two links.**

The figure **(a)** shows how the under-actuation mechanism increases the adaptiveness of the robot. Also, the figure **(a)** and **(d)** show the under-actuation mechanism that uses a fixed pulley. The figure **(b)** and **(e)** show the under-actuation mechanism using a movable pulley that is used in the conventional robot. Figure **(c)** and **(f)** show the method to implement the under-actuation mechanism using the proposed STLA. The dotted lines in the figure **(d)** to **(f)** mean the end-effector while the other part is located far from the end-effector.

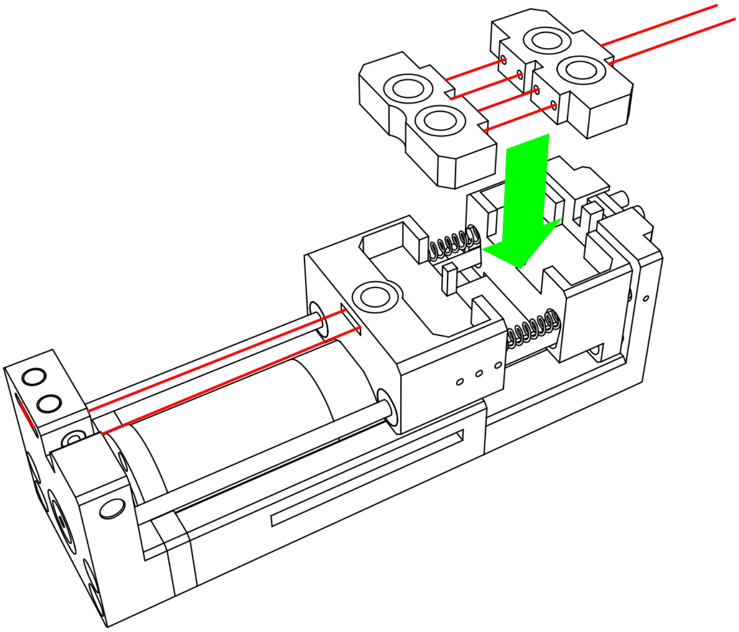

**Figure 2.5: Schematic showing how the tendon connector in the STLA works.**

It includes the function of the tendon connection by separating the end-effector tendon from the slider.

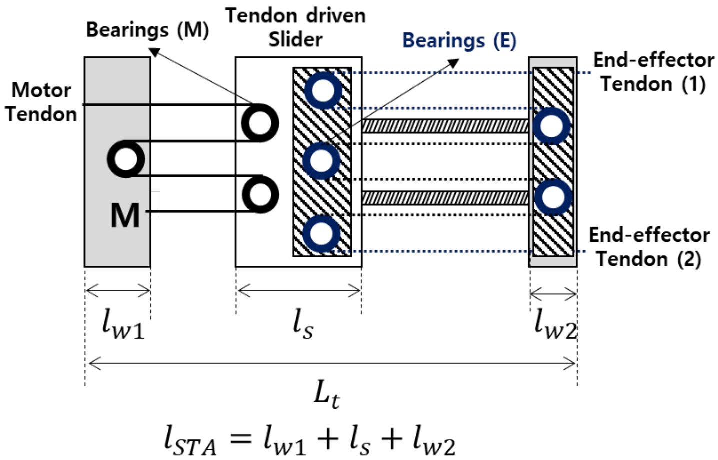


**Figure 2.6: Schematic showing how the stroke of the STLA is amplified.**

Bearings on the end effector side not only allow the STLA to have the under-actuation mechanism, but also amplify the wire stroke. $n_e$ is the number of the movable pulleys at the slider.

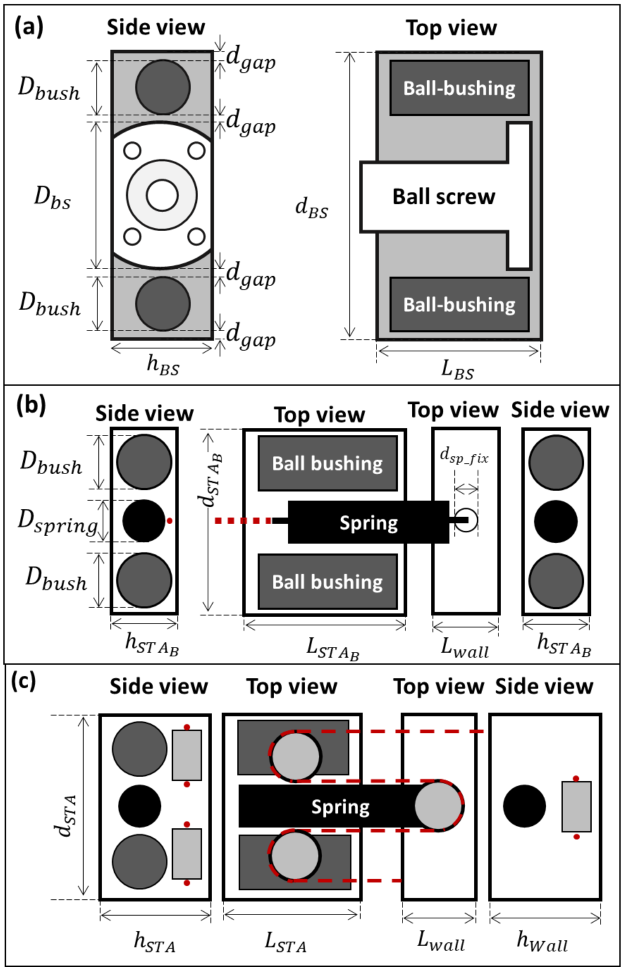


**Figure 2.7: Schematic of each actuation for size comparison**

**(a)** ball screw linear actuator, **(b)** Basic STLA (STLAB), and **(c)** STLA. The red dotted line in the figure is the wire used in the actuator.

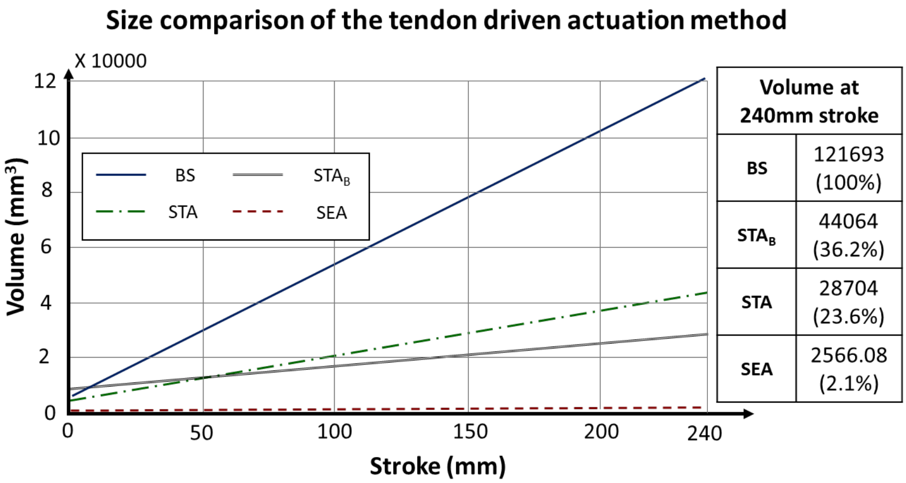


**Figure 2.8: Size comparison of the tendon-driven actuation unit for a soft wearable robot.**

The size of the STLA is 36.2% of the ball screw. When the movable pulley is used in STLA design, the size becomes more compact and it is 23.6% of the ball screw. Although the size is reduced, the STLA is about 11.2 times bigger than the slack-enabling actuation unit. Values on the right side show the volume of each actuation method when the stroke is 240 mm.

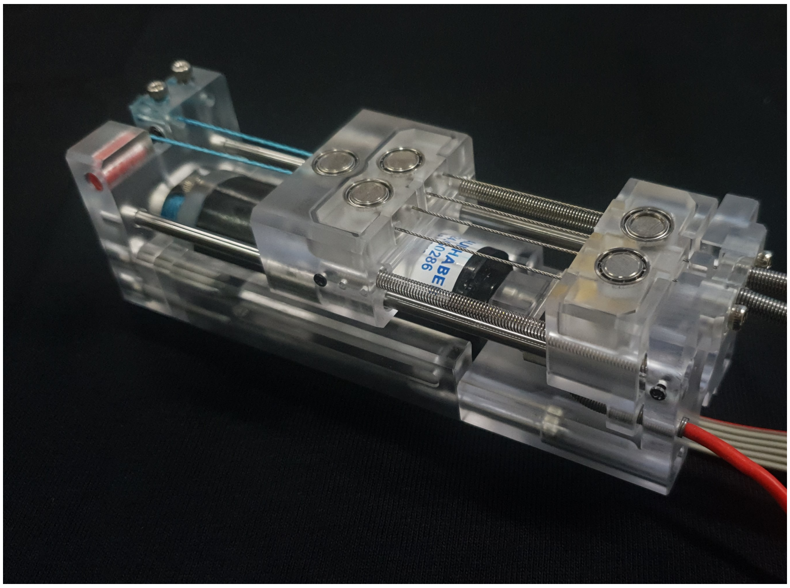

**Figure 2.9: Final design of Slider-Tendon Linear Actuator.**
The actuator contains the functions of wire derailment prevention, under-actuation, and tendon connection. One loadcell is used to measure the tension of the wire. The blue wire in the left side is a motor tendon while the gray wire in the right side is an end-effector tendon.

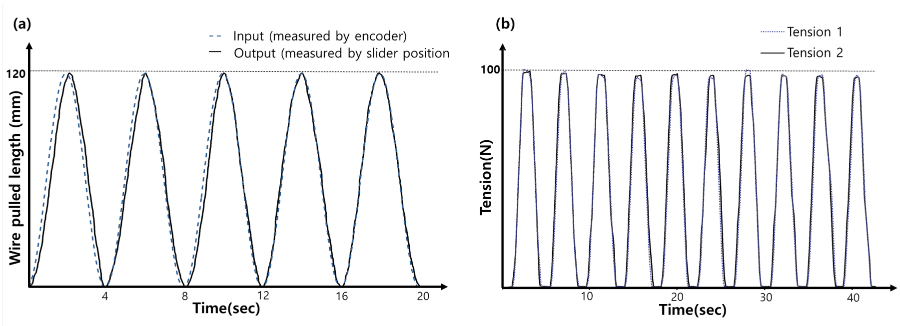


**Figure 2.10: Actuator performance in position (a) and force domain (b).**

The actuator pulls wire 120mm in 1.5 seconds in a no-load condition, which sufficiently satisfies the requirements. The rms error between the estimated and real slider position is 3.61(%). The blue dotted line in figure **(a)** is the pulled length calculated by the encoder and the black solid line is the pulled length of the wire calculated by the slider position. Figure **(b)** shows that the tension of the wire reaches to 100N and the tension applied on the two wires is similar.

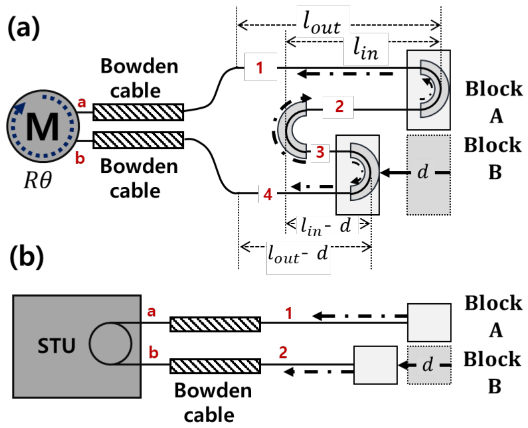


**Figure 2.11: Schematic of the tendon routing to analyze the tension distribution.**

For simplification, fingers are assumed as a block that moves linearly; **(a)** shows the under-actuated tendon routing using fixed pulleys and **(b)** shows the under-actuated tendon routing using a movable pulley.

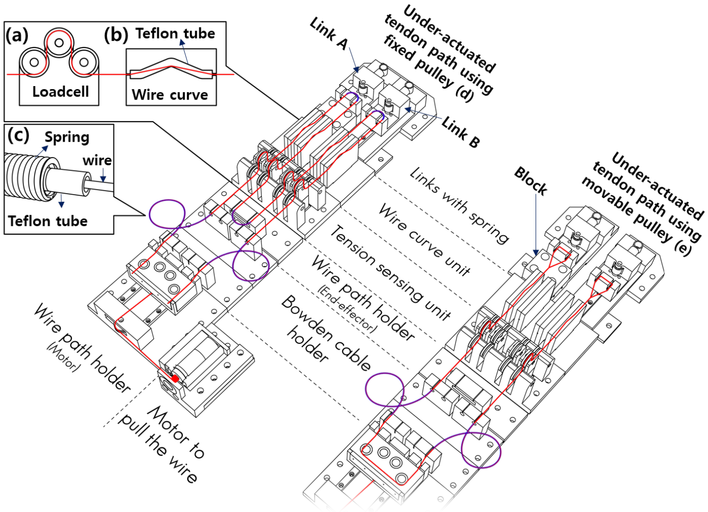


**Figure 2.12: Experimental and simulated results of the force difference that is applied to the finger**

**(a)** Tendon routing A refers to the wire path that has an under-actuation mechanism using fixed pulleys; tendon routing B means the path that uses a movable pulley. (*) means that there is a significant difference between the two results. Also, the force difference enlarges as the finger flexion angle increases in tendon routing A, while routing B is not significantly affected by the change in the angle of the finger bend **(b)**. For the under-actuation mechanism evaluation, it is important to know the ratio of the force applied to the two fingers, rather than the absolute magnitude of the force. Therefore, both graphs are represented by converting all values as a percentage of the force exerted on one finger ($F_B$).

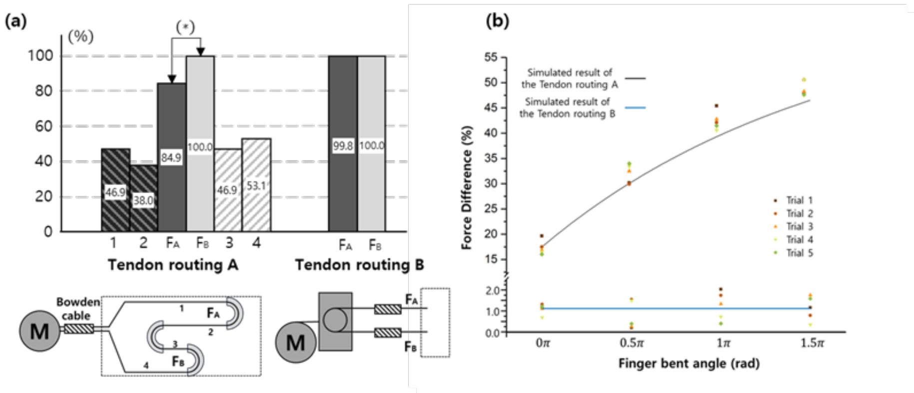


**Figure 2.13: Experimental setup to measure the tension distribution of the wire path.**

**(a)** shows the method to measure the tension with curved wire path. The wire curve unit in **(b)** intentionally makes the wire to bent. **(c)** shows schematic of Bowden cable. By changing the wire path, tension distribution of two wire paths is measured.

**Table 2.1:** Notation used in the chapter 2

| Notation | Definition |
|---|---|
| $n_e$ | Number of movable pulleys at the motor tendon |
| $\epsilon_M$ | Gear ratio of the motor |
| $n_e$ | Number of movable pulleys at the end-effector tendon |
| $R$ | Radius of the motor spool |
| $tau_M$ | Motor stall torque |
| k | Spring coefficient at the actuation unit |
| x | Displacement of the slider |
| $w_M$ | Motor no-load speed |
| $L_t$ | Total length of the actuator |
| $l_{sta}$ | Length of the sliding tendon unit |
| $D_{stroke}$ | Stroke of the actuator |
| $A_t$ | Actuator total cross-section area |
| $A_{motor}$ | Initial cross-section area of the motor |
| $a_e$ | Cross-section area generated by movable pulley |
| $m_s$ | Mass of the slider |
| $\mu_{bs}$ | Friction coefficient b.t.w the rod and bushing |
| g | Gravitational acceleration |
| $T_0$ | Initial tension of the spring |
| $T_M$ | Tension of the end-effector tendon |
| $\mu_{sh}$ | Friction coefficient b.t.w the wire and spring sheath |
| $\theta$ | Curved angle of the spring sheath |
| $\mu_{tf}$ | Friction coefficient b.t.w the wire and Teflon tube |
| $\mu_b$ | Friction coefficient b.t.w the wire and bearing |

**Table 2.2:** Requirements for the actuator for use in the Exo-Glove II

| **Requirements** | **Value** |
|---|---|
| Tension | 100 (N) |
| Stroke | 120 (mm) |
| Pulling and releasing time | 4 (sec) |

Table 2.3: Parameters for actuator size estimation

| Design parameter | Value |
|---|---|
| Gap between mechanical components ($d_{gap}$) | 1 (mm) |
| Diameter of bushing ($D_{bush}$) | 7 (mm) |
| Length of bushing ($L_{bush}$) | 10 (mm) |
| Diameter of flange ($D_{bs}$) | 19 (mm) |
| Width of flange ($T_{bs}$) | 13 (mm) |
| Length of flange ($L_{bs}$) | 13 (mm) |
| Diameter of bearing ($D_{bearing}$) | 8 (mm) |
| Height of bearing ($h_{bearing}$) | 2 (mm) |
| Diameter of spring ($D_{spring}$) | 3 (mm) |
| Length of spring ($l_{spring}$) | 30 (mm) |
| Diameter of bolt to fix the spring ($d_{sp-fix}$) | 2 (mm) |

**Table 2.4:** Properties of the STLA components and actuator performance

| **Component** | **Value** |
|---|---|
| Number of movable pulleys | 2 (EA) |
| Spring coefficient | 0.02 (N/mm) |
| Spool diameter | 5 (mm) |
| Motor stall torque (without gearbox) | 21.2 (Nmm) |
| No-load speed (without gearbox) | 8200 (rpm) |
| **Actuator performance** | **value** |
| Max. Tension (at nominal torque) | 161.49 (N) |
| Stroke of the actuator | 124 (mm) |
| Max. speed of the wire | 31.11 (mm/s) |
| Required time to pull 100mm stroke | 3.23 (sec) |

**Table 2.5:** Tension distribution of the wire path with fixed pulleys

| Tension relationship | | Tension distribution | |
|---|---|---|---|
| $T_M = T_a + T_b$ | (2.35) | $T_1 = G_\mu T_M e^{-\mu_{sh}\theta}$ | (2.36) |
| $T_1 = T_a e^{-\mu_{sh}\theta}$ | (2.37) | $T_2 = G_\mu T_M e^{-\mu_{sh}\theta - \mu_{tf}\pi}$ | (2.38) |
| $T_4 = T_b e^{-\mu_{sh}\theta}$ | (2.39) | $T_3 = G_\mu T_M e^{-\mu_{sh}\theta - 2\mu_{tf}\pi}$ | (2.40) |
| $T_2 = T_1 e^{-\mu_{tf}\pi}$ | (2.41) | $T_4 = G_\mu T_M e^{-\mu_{sh}\theta - \mu_{tf}\pi}$ | (2.42) |
| $T_3 = T_2 e^{-\mu_{tf}\pi}$ | (2.43) | $G_\mu = 1/(1 + e^{-\mu_{tf}\pi})$ | (2.44) |
| $T_3 = T_4 e^{-\mu_{tf}\pi}$ | (2.45) | | |

**Table 2.6:** Tension distribution of the wire path with a movable pulley

| **Tension relationship** | | **Tension distribution** | |
|---|---|---|---|
| $T_M = T_a + T_b$ | (2.46) | $T_1 = G_{\mu_b} T_M e^{-\mu_{sh}\theta}$ | (2.47) |
| $T_b = T_a e^{-\mu_b \pi}$ | (2.48) | $T_4 = G_{\mu_b} T_M e^{-\mu_{sh}\theta - \mu_b \pi}$ | (2.49) |
| $T_1 = T_a e^{-\mu_{sh}\theta}$ | (2.50) | $G_\mu = 1/(1 + e^{-\mu_b \pi})$ | (2.51) |
| $T_4 = T_b e^{-\mu_{sh}\theta}$ | (2.52) | | |

# Chapter 3

# Under-actuated Tendon Routing

## 3.1. Background

This chapter introduces a method to implement the STLA (Slider-Tendon Linear Actuator) in the Exo-Glove II. Since the STLA is developed to locate mechanisms in the actuator part rather than in the end-effector, the tendon routing of the robot to have better features: 1) Performance of the under-actuation mechanism such as force distribution, efficiency, and reliability can be improved. 2) Tension at the end-effector, which is required for the force control of the end-effector, can be simply measured. This chapter, therefore, show a method to obtain the best tendon routing when the STLA is considered. For the detail, section 3.2 explains the basic principle of the under-actuation mechanism. Then in section 3.3, methods to implement STLA in the robot that improve the under-actuation performance are described. In the section 3.4, the validation of the under-actuation performance of the Exo-Glove II is explained. Finally, section 3.5 shows the discussion and conclusion of this chapter.

## 3.2. Under-actuation Mechanism

In this thesis, we define under-actuated system as a system that a rank of the vector space of the actuator input ($n$ in the Figure 3.1) is smaller than a rank of the vector space of the joints ($m$ in the Figure 3.1). To apply torque on all joints with smaller number of actuator, some joints should be designed to have constraints with other joints; In this case, we do not consider a passive element such as spring. The constraints applied on the joints can be divided into kinematic constraint and kinetic joints as shown in the Figure 3.1. The aspects of the motion varies according to the type of the constraints. Details of under-actuation mechanism with each constraints are explained in the following sections. The definitions of all variables used in this chapter are organized in Table 3.1 for the reader‘s convenience. Also, the actuation characteristics for all the constrained under-actuation mechanism are summarized as Table.3.2.

### 3.2.1. *Kinematic ($k_m$) constrained under-actuation mechanism*

When the joints are constrained kinematically which is usually named as a *coupling mechanism*, the joints move according to the fixed ratio while the torque applied on the joints do not have any relationship as shown in 3.2 (a). The design with kinematic constraints ($K_mC$s) has advantages in making a certain motion precisely even the external force or disturbance is applied to the system. However, kinematic constrained under-actuation mechanism($KmC$-$UM$) sometimes causes a problem in the application which interacts with the environment because the overall joints cannot move when the specific joint is blocked (Catalano *et al.* 2014).

In the tendon-driven system, several wires tied to a single wire or a set of pulleys having the same rotational axis make coupled motions of kinematically constrained joints as shown in 3.2 (b). *KmC-UM* in the tendon-driven system is sometimes named as *synergy*, which is a concept developed by observing human movement from neuroscientific studies (Bicchi *et al.* 2011). Several robotic hands were developed by applying the concept of synergy to either control or robot mechanism. Asada (Brown & Asada 2007) designed robotic hand with the concept of postural synergy and proved that the robotic hand can be designed simpler by reducing the number of actuators.

### 3.2.2. *Kinematic ($k_m$) constrained under-actuation mechanism with compliant components*

Some researches tried to complement the contact problem of the *KmC-UM* with a concept named as *soft synergy*. It solves the problem by connecting compliant components in series to the kinematic constrained under actuation mechanism (Catalano *et al.* 2014). In this concept, as shown in Figure 3.3, the joint configuration is defined by the force equilibrium equation using the compliance of the additional components. The real robot configuration($x_i$) does not depend on the position($X$) of the actuator as shown in Eq (3.1);Here, joint $j$, the joint which does not contact with the object, moves similar to the joint with *KmC-UM*. However, the joint $l$, the joint which contacts with the object, sustains it‘s position after contact, even the actuator position ($\Delta X$) increases because force applied on the joint ($F_l$) also increases. As a result, joints in this system make adaptive motion thanks to the elongation of the compliant components.

$$\Delta x_i = \begin{cases} r_j \Delta X & \text{Joint } j \text{ does not contact.} (i = j) \\ r_l \Delta X - \dfrac{F_l}{k_l} & \text{Joint } l \text{ contacts with the object.} (i = l) \end{cases} \tag{3.1}$$

However, contact force with compliant *KmC-UM* depends on the stiffness($k_i$ in the Eq (3.2) and the difference between the real joint position and the actuator position($\Delta x_i - r_i \Delta X$ in the Eq (3.2). When the stiffness is too large, the contact force increases rapidly even the other links do not contact to the object. Rapidly increased contact force cause grasp problem because the object can be affected by the force before stable grasp is formed. In the case of using the low stiffness component, on the other hand, the adaptability of the grasp is increased. However, the low stiffness case requires relatively long time to make grasp force. It is because the contact force is determined by the difference between the reference position and the real position multiplied by the stiffness: the low stiffness case, therefore, requires enlarged actuation stroke to make enough reference position.

$$F_i = k_i(\Delta x_i - r_i \Delta X) \tag{3.2}$$

3.2.3. *Kinetic ($k_n$) constrained under-actuation mechanism*

On the other hand, when the joints are constrained in kinetic condition, which is also named as *differential mechanism* or *under-actuation mechanism* in other researches, the contact problem caused in the *KmC-UM* or compliant *KmC-UM* can be solved (Birglen & Gosselin 2006). The joints with a kinetic constraints ($k_n c$s) have no restriction on displacement, but the torque or force applied to the joints is maintained to a certain ratio. Because of the above feature, the kinetic constraint between joints enables to apply a uniform force or torque and to make an adaptable configuration for the surrounding object. In the tendon-driven system, the kinetic constraint is applied to the target joints by making a single wire to passes through multiple joints or links simultaneously. The tension applied on the target joints are always the same because the tension is always consistent when the friction is not considered.

When applying the kinetic ($k_n$) constraints to the joints by passing one wire through multiple joints, both movable pulley and fixed pulley can be used as shown in Figure 3.4. Usually, the type of pulley is differently used depending on whether joints are connected in series to a single linkage or joints are connected in parallel to multiple links. In the case, which serially connected joints (e.g., different joints located in a single finger) at the same link, $k_n$ constraints can be easily assigned to the joints by connecting one end of the wire to the last link and the other end of the wire to the actuator as shown in right side of the Figure 3.4 (b).

However, in the case of other joints in other links (e.g., different joints located in different fingers) with a parallel configuration, movable pulleys can be used. The movable pulley between the two parallel links transmit the force to the wire and enables to give $k_n$ constraints on the joints in parallel connected linkages as shown in the left of the Figure 3.4 (b). With the concept of movable pulleys, (Hirose 1985) developed a robotic hand using moving pulley. Also, this method was also extended to the study developing a robotic hand which has $k_n$ constraints on 5 fingers(Lalibert 2008). A total of four moving pulleys were used to assign $k_n$ constraints in the above research because additional pulley should be added when the additional finger is actuated under the $k_n$ constraints. $k_n c\text{-}UM$ using movable pulleys successfully apply pre-determined tension to each tendon, but it also makes the end-effector bulky because additional space is required for the pulleys and the space required for pulleys to move. Moreover, when the number of the linkages increases, the system becomes complex because system with $n$ number of linkages requires $n-1$ number of movable pulleys for $k_n c$-$UM$.

### 3.2.4. *Kinetic ($k_n$) constrained under-actuation mechanism with dual tendon routing*

In the tendon driven $k_n c$-$UM$, we can see that $k_n c$-$UM$ can be implemented by a single wire passing through multiple joints; since the tension is sustained along the wire, it can apply $k_n c$s on the joints. In a same manner,methodology to pass the wire twice in a single linkage is proposed in robot named SNU Exo-Glove to make compact $k_n c$-$UM$ (In *et al.* 2015). Here, the wire is not just connected to the end of the link, but rather it goes out after being bent at the end of the links as shown in Figure 3.5. This tendon routing allows the force to be transmitted without using movable pulleys because the wire end can be connected to the actuator after passing through the joints of whole fingers. In this thesis, we named the tendon routing as *dual tendon routing*(Originally it was named as *soft tendon routing* because it was implemented in the soft wearable robot. However, this tendon routing method is possible to be used also in the rigid robot, therefore we renamed the routing.) Although this routing compactly assigns $k_n c$s to multiple linkages, it has disadvantages over the use of movable pulleys in terms of performance that the torque applied to the joints are relatively less uniform;The tension distribution is less uniform in *dual tendon routing* because the friction force overlaps through the tendon routing., which will be explained details at the section 3.4.

The robotic hand using dual tendon routing for five fingers were developed by (Catalano *et al.* 2014) and showed that the *dual tendon routing* makes the robotic hand simple even the hand has many fingers. In the case of dual tendon routing of SNU Exo-Glove, Teflon tube was used instead of the bearing to fix the wire path in curvature. Tendon routing with Teflon tube made the robot part more compact because it is relatively small compared to bearing and it can be easily attached on the glove with sewing.

However, the method using the Teflon tube and dual tendon routing has disadvantages on force distribution and efficiency. As a result, the tendon driven under-actuation mechanism has a trade-off relationship between performance and size depending on the type of components used and the tendon routing method. Therefore, our goal of this chapter is to get the best tendon routing which covers the above trade-off relationship by considering the Slider-Tendon Actuator, which is explained in the chapter 2, and dual tendon routing in this chapter.

## 3.3. Kinetic Constrained Under-actuated Tendon Routing with Slider-Tendon Linear Actuator in Soft Wearable Robot

### 3.3.1. *Dual tendon routing in system with N fingers*

In this subsection, methodology to obtain whole possible dual tendon routing for $N$ linkages is described as shown in Figure 3.6. The possible tendon routing are first derived by considering the actuator part as well as the end-effector. It is because our hypothesis is that locating the under-actuation mechanism both in to the end-effector and the actuator increases the number of possible routing and shows a higher performance than the conventional mechanism. Since the friction of the wire is generated when the wire path is curved, we divided the segments into $2N$ sections as shown in the Figure 3.6. Also, all the notation used in this chapter is described in the Figure 3.6.

When the wire is passing the top of the $i^{\text{th}}$ segment(space between section $2i-1$ and $2i$), only fixed pulley can be used at the curve of the wire path as shown in right side of the Figure 3.6. On the other hand, the tendon routing at the bottom of the section, area between the $i^{\text{th}}$ segment and $(i+1)^{\text{th}}$ segment shown in Figure 3.6, has two design candidates of using movable pulley or fixed pulley. The pulley can be attached to the robot to work as a fixed pulley or can be attached on the actuating part to work as a movable pulley. Therefore, the number of $2^{N-1}$ cases exists because it is necessary to determine whether a total of N-1 pulleys will be used as a movable pulley or a fixed pulley. After that, by fixing the method to connect the wire at $P_1$ in the first segment and $P_{2N}$ in the $N^{\text{th}}$ segment, we can obtain whole possible tendon routing in $N$ numbers of finger system; It can be either fixed to the glove or to the motor, so there exist two cases each. As a result, tendon routing for system with N segments can be configured and has total $2^{N+1}-1$ number of cases for routing; There are $2^{N+1}-1$ of cases instead of $2^{N+1}$ because one design, which whole wire is routed by fixed pulleys and wire at the both ends are fixed on the robot, should be excluded because the actuation force cannot be transmitted to the robot in the design. When the number of the segment is odd number, total numbers of design, which requires to ignore the symmetric case, can be reduced to $2^N-1$ because of several overlapping tendon routing.

In the dual tendon routing which combines to use both fixed pulleys and movable pulleys, the end-effector can make high force with small actuation force but requires a long stroke when the use of fixed pulley increases. On the other hand, when the use of movable pulleys is increases, the end-effector can generate motion with a short stroke but requires a higher force to make force at the end-effector. It is quite obvious and can be obtained using the virtual work principle. In addition, the friction of the wire shows different aspects because the friction is affected by the moving direction of the wire and the material properties.

Therefore, final tendon routing can be decided after the application is fixed. In this thesis, we simplified the tendon routing of $N$ segments cases to tendon routing of 2 segments case because our target application is Exo-Glove II. The tension distribution in each segment for $7(2^{(2+1)}-1)$ design candidates were calculated considering friction in the subsection 3.3.2.

### 3.3.2. *Dual tendon routing in Exo-Glove II*

The tendon routing for flexion of the index and middle finger of the Exo-Glove II can be designed in 7 cases, which is classified in Figure 3.7 (a). As Figure 3.7 (b) - (h) show, 7 tendon routings are possible and each are named as TR1 to TR7 respectively. In order to select the best tendon routing, distribution of the wire tension is calculated for each case as shown in Table.#. Since we are considering dual tendon routing in 2 linkages system, tension of maximum 8 segments can be obtained as 3.7 shows; Four are on the motor side and other four are on the end-effector side. The segments in motor side from the spring sheath is notated from $a$ to $d$ and the glove side from the spring sheath is defined as 1 to 4. The finger containing the wire segment 1, 2 is named as Finger A, and the finger with wire segment 3, 4 is called Finger B. Since the friction on the wire is mainly modeled by the capstan equation, the wire tension of all segments is also obtained as proportional to the motor torque. The detail process to derive the tension distribution is described in Appendix A.

### 3.3.3. *Indicators to validate the under-actuation mechanism*

In addition to obtaining the tension distribution, four indicators for the $k_n c$-$UM$ are proposed, as shown in Table.3.3 and 3.4, for the best tendon routing of the Exo-Glove II . The first indicator is derived to measure an adaptability of the robot, that is defined as a difference between sum of the tension applied on two fingers as shown in Eq (3.4). The difference between the tension induces a problem when only one finger is contacted with the object. Depending on the shape of the object, there is a case where only one of the two fingers is touched first. In this case, if a large force is applied to the contact surface before the other finger touches, the object is moved and disturb the stable grip.

Second performance is a performance about the tension difference in the same finger. When the tension applied on the same finger has big difference, the finger can make abduction or adduction motion which is an unwanted motion. Moreover, in the soft wearable robot case, the difference between the tension makes deform of the robot itself and the tendon routing can be changed. For this reason, the performance about the tension difference in the same finger is named as torsional resistance performance and can be defined as Eq (3.5).

Third performance is about the reliability of the system. The tendon-driven system must have low friction because the wear, which is related to the reliability, of the wire is determined by the friction. However, since the failure will occur first in the area where friction is concentrated, the largest frictional force is defined as an index of the reliability. The third indicator is described as Eq (3.6), where $n$ in the equations mean the number of areas which friction occurs.

The final performance indicator is related to the efficiency of the robot. Efficiency is selected because it affects the size and weight of the motor and battery used in the robot. The indicator is expressed as the ratio of the work done by actuator and the work done by end-effector. Therefore, the performance can be expressed as Eq (3.7).

## 3.4. Validation of the Dual Tendon Routing with Slider-Tendon Linear Actuator

### 3.4.1. *Tension distribution*

To verify the tension distribution and indicators of seven tendon routings, an experimental setup was designed to measure the tension at each segment as shown in Figure 3.8. Four load cells were used to measure the tension distribution. By changing the tendon routing at the wire path holder part, tension distribution of 7 tendon routings were obtained in a single experimental setup; Four bearings are used in the path holder and 7 tendon routings is made as shown in Figure 3.8(f). The Motor is controlled to pull the wire until the sum of the tensions at section 1 to 4 reaches the 70N tension. The experimental results of each tendon routing are also described in each section. Using the experimental setup, tension distribution of the 7 tendon routings was obtained. Since all tension of each section is function of the motor torque, the distribution is described in terms of percentage to the total sum of tension.

### 3.4.2. *Under-actuation performance*

With the tension distribution data, under-actuation performance of 7 tendon routings were verified. Since there are four indicators for 7 tendon routings, radial graph is used as shown in Figure 3.10. Equations for normalized indicators are described as Eq (3.8) - Eq (3.11). In the normalization process, it is assumed to sum from $T_1$ to $T_4$ to be $200N$. $w_a$, $w_t$,$w_r$, and$w_e$ are set to be 5 to make all indicators to have maximum 5 and minimum 0.

### 3.4.3. *Possible applications*

Seven tendon routings introduced in this paper show different performance. As we can see in Figure 3.10, TR6 shows better performance compared to other tendon routings. It is quite obvious because this tendon routing includes two movable pulleys, which have advantages to make uniform tension distribution by reducing the friction. Although TR6 shows better performance, TR3 is decided to be used in the case of Exo-Glove II because this tendon routing has the advantages of compact tension measurement and easy wire length adjustment at the end effector. Details about how to measure tension and to adjust the wire length is not explained in this chapter because these are described in chapter 4.

Although tendon routings, paths other than TR3 and 6, are not applied in Exo-Glove-thumb, but they can be used in other applications that have different requirements. For example, TR1, a tendon routing that uses three fixed pulley, shows relatively low performance because friction is applied on the wire in a serial. However, TR1 has high force transmission ratio with compact size. The force transmission ratio can be easily defined as a ratio between force applied on a finger and tension of wire at the motor as shown in Eq (3.3). When the friction is not considered, the transmission ratio of the TR1 can be easily obtained as 4 while that of other tendon routings is obtained as 1 or 2. Therefore, TR1 can be used where large grasping force is required with small actuation force. It is true that the transmission ratio is not exactly 1 or 2 or 4, when the friction is considered.

$$R_{tr} = \frac{F_{finger-A} + F_{finger-B}}{T_M} = \frac{T_1 + T_2 + T_3 + T_4}{T_M} \tag{3.3}$$

TR1 can be found in a previous research about GRIPIT, which is a hand wearable device developed to assist tripod grasp of a disabled person(Kim *et al.* 2017). In GRIPIT shown in Figure 3.11, one side of the wire is connected at the end-effector part while the other side of the wire is pulled by the user. Since GRIPIT has TR1 type tendon routing, the device can make sufficient grasping force with small tension. It is suitable to use TR1 in GRIPIT because the device is developed not to include motor and to be operated manually with a single actuation.

On the other hand, when the different amount of tension is required to be applied on different fingers, TR4 and 5 can be adequate candidates. Since the wire passes from one finger to the other finger through Bowden cable in these paths, tension applied on two fingers show big difference in TR4 and 5. Due to this aspect, these paths can be used for the device that assists pinch grasp. It is because tension applied on the thumb should be big while the tension on the other fingers only requires to make a posture in the pinch grasp.

In the case of TR2, it can be used for the case which requires to locate the actuator at the end-effector. When the actuator is required to locate at the end-effector, the size of actuator has to be minimized. When slack enabling actuator is used for compact size, only TR1 or TR2 can be used because the slack enabling actuator does not have a room for movable pulley(In *et al.* 2017). Therefore TR2 should be used in this case.

## 3.5. Discussion & Conclusion

In chapter 3, we proposed a design framework to obtain the best tendon routing that applies kinetic constraints on the joints. The framework combines following two functions used in the tendon driven soft wearable robot: a concept of dual tendon routing and the Tendon-Slider linear actuator. With this framework, researchers can derive an optimal tendon routing because it assists to get whole possible tendon routings considering the dual tendon routing and the Slider-Tendon actuator. By using the framework the Exo-Glove II could be designed to measure tension and adjust the length of wire at the end-effector easily. Since chapter5 shows control of the Exo-Glove II, all contents about advantages of the framework on force control are explained in the next chapter.

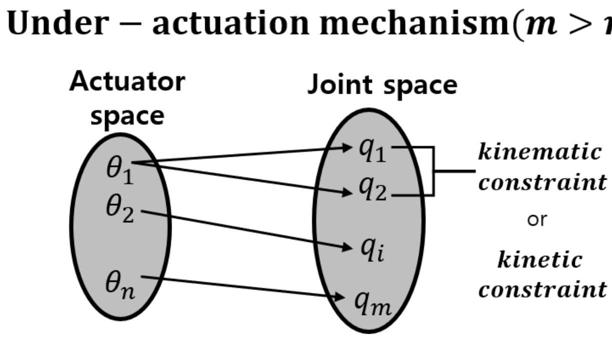


**Figure 3.1: Classification of the under-actuation mechanism**

$\theta_i$ in the figure means the displacement of the actuators while the $q_i$ in the figure means the displacement of the joints. Since the number of the joints are smaller than that of the actuator, constraints between the joint angle are required.

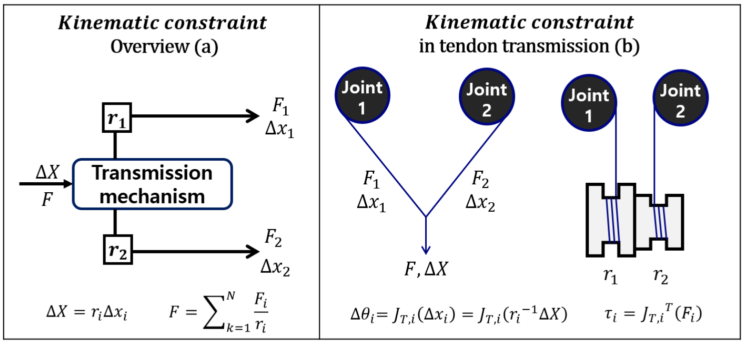


**Figure 3.2: Overview of the under-actuation mechanism with kinematic constraints**

**(a)** shows the schematic of the kinematic constrained under-actuation mechanism. This figure is inspired by (Birglen & Gosselin 2006). **(b)** shows the exact method to apply kinematic constrained under-actuation mechanism using tendon transmission.

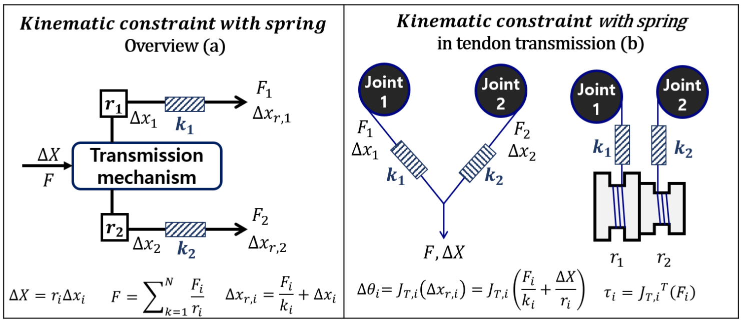


**Figure 3.3: Schematic of the under-actuation mechanism with kinematic constraints and springs**

**(a)** shows the schematic of the kinematic constrained under-actuation mechanism. This figure is inspired by (Birglen & Gosselin 2006). **(b)** shows the exact method to apply kinematic constrained under-actuation mechanism using tendon transmission.

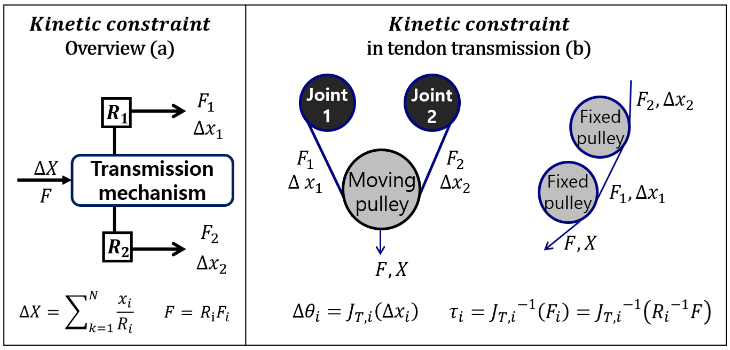


**Figure 3.4: Schematic of the under-actuation mechanism with kinetic constraints**

**(a)** shows the schematic of the kinetic constrained under-actuation mechanism. This figure is inspired by (Birglen & Gosselin 2006). **(b)** shows the exact method to apply kinetic constrained under-actuation mechanism using tendon transmission. The constraints can be applied using both moving pulley and fixed pulley

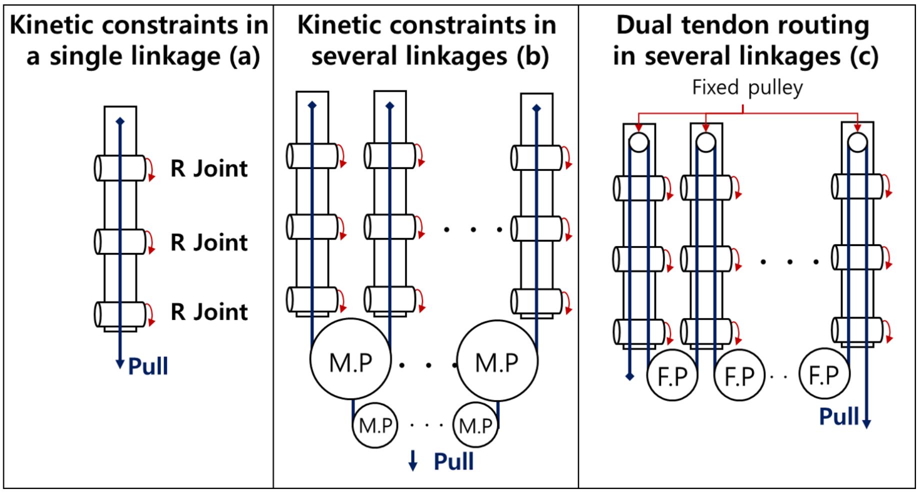


**Figure 3.5: Summary of the under-actuation mechanism with $k_n$ constraints**

**(a)** shows a kinetic constrained under-actuation mechanism in a single linkage. **(b)** shows a kinetic constrained under-actuation mechanism using movable pulleys. **(c)** shows a kinetic constrained under-actuation mechanism using dual tendon routing.

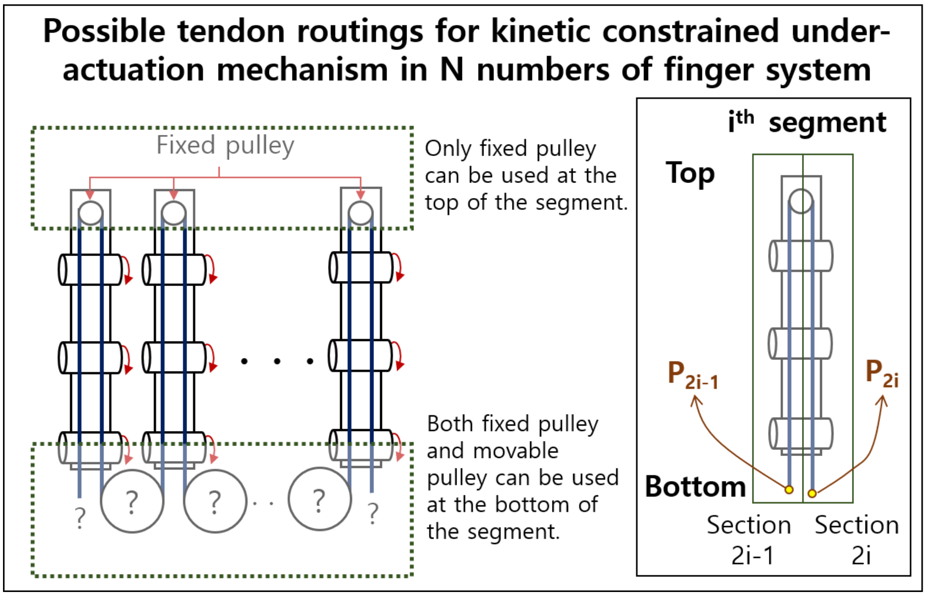


**Figure 3.6: Overview of the dual tendon routing in $N$ numbers of linkage system**

The tendon routing is separated in to $2N$ sections.The tendon routing can be determined by determining whether to use a fixed pulley or a movable pulley in the space between the sections.

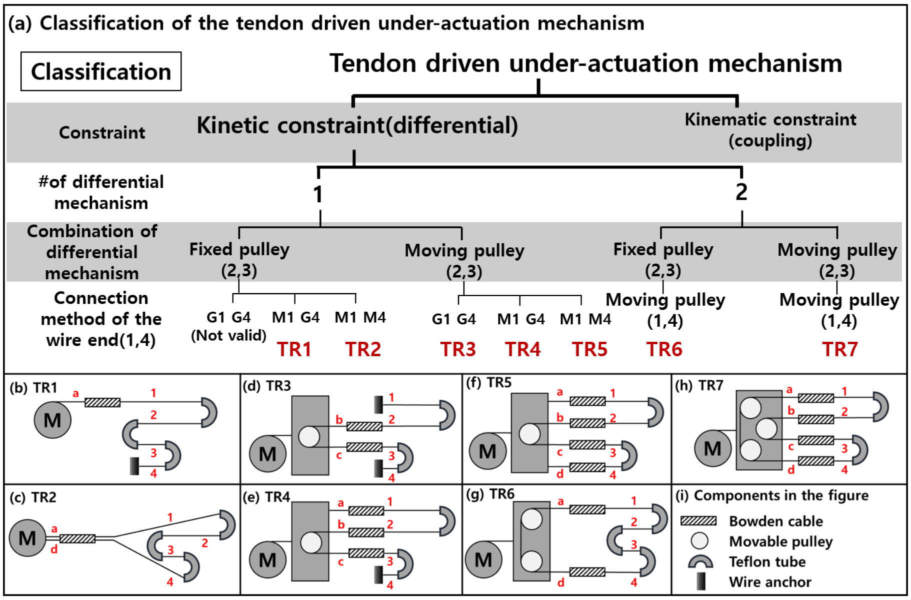


**Figure 3.7: Classification method for possible tendon routing in two linkage system**

**(a)** shows the overall view of the classification and **(b)** - **(h)** show each tendon routing that applies kinetic constraints on the joints. **(i)** shows the description of the components used in the figure. In the figure, E(#) means the wire in # segment is connected at the end-effector and M (#) means the wire in # segment is connected at the actuator. Wire anchor in **(i)** means the point where tendon is fixed.

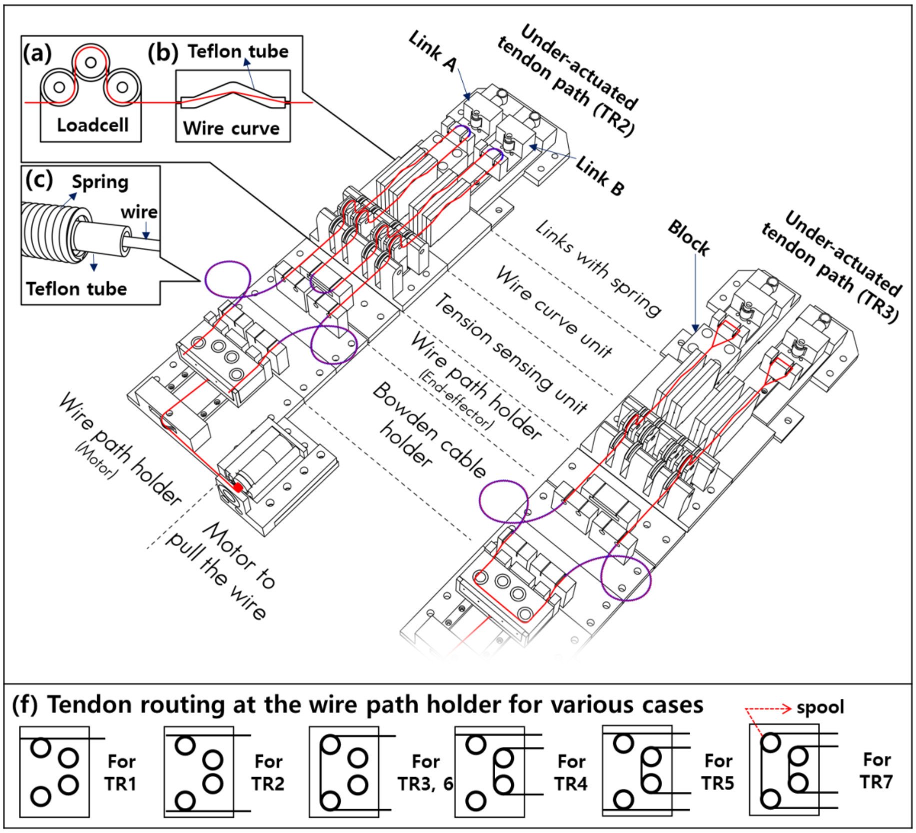


**Figure 3.8: Experimental setup to measure tension distribution of the tendon routing**

By changing the tendon routing at the wire path holder, the experimental setup cover tension measurement for seven tendon routings as shown in **(f)**.

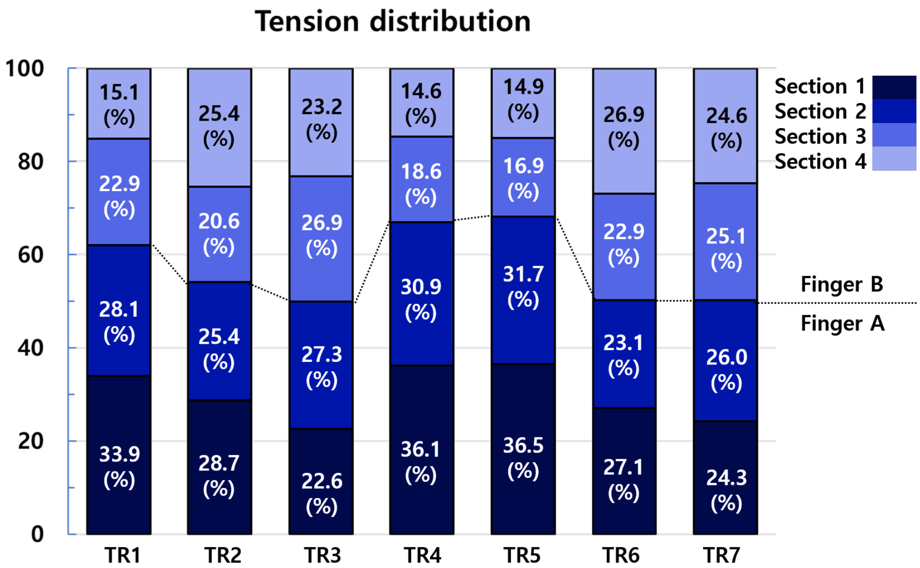


**Figure 3.9: Tension distribution of tendon routing with dual tendon routing**

Tension at each section is described in terms of percentage to the total sum of tension. TR1 to TR7 are nominations of tendon routing which are described in Figure 3.7. As indicated by the dotted lines in the figure, the difference in the forces exerted on the fingers A and B is different according to the tendon routing.

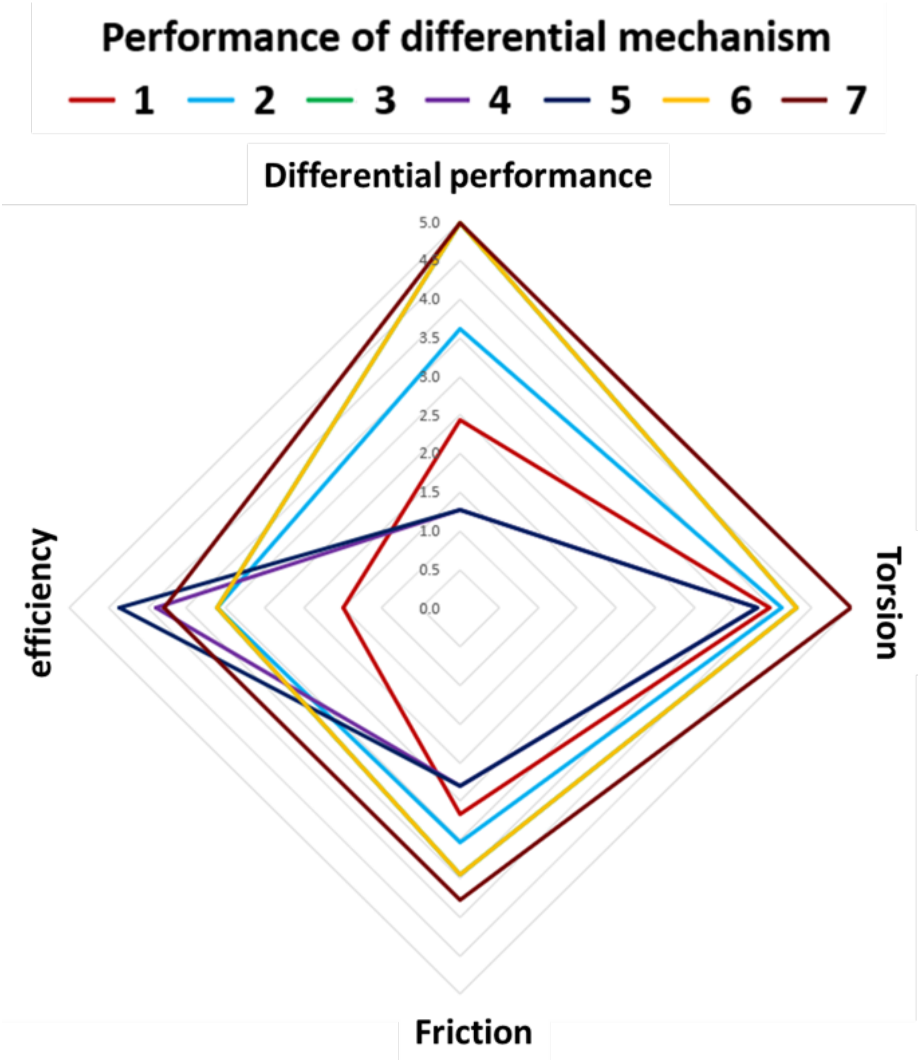


**Figure 3.10: Experimental result about indicators of kinetic constrained under-actuation mechanism**

Four indicators are used for the validation. Here, TR6 shows the best result because of movable pulleys that have advantage to reduce the friction.

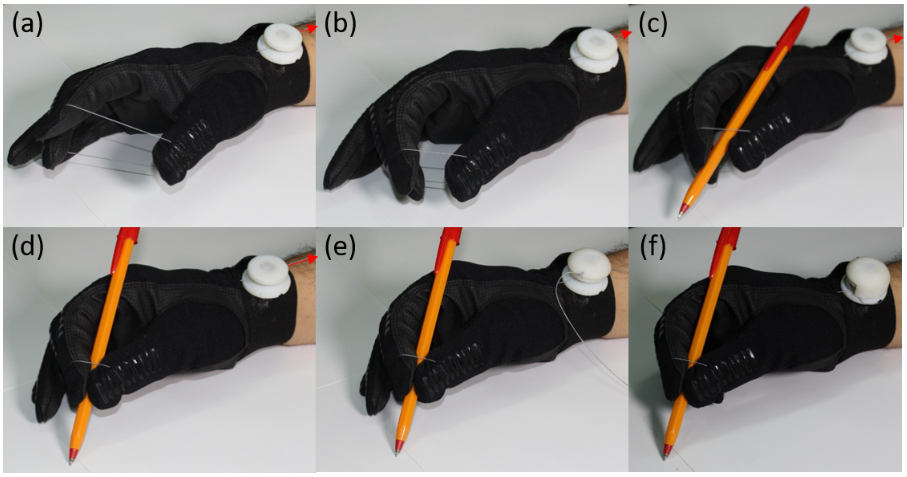


**Figure 3.11: Example of TR1 in dual tendon routing method: GRIPIT**

GRIPIT, which has a tendon routing similar to TR1, can be used to assist tripod grasp without motor because it is developed to have high force transmission ratio.

**Table 3.1:** Notation used in the chapter 3

| Notation | Definition |
|---|---|
| $n_e$ | Number of movable pulleys at the motor tendon |
| $\epsilon_M$ | Gear ratio of the motor |
| $n_e$ | Number of movable pulleys at the end-effector tendon |
| $R$ | Radius of the motor spool |
| $\tau_M$ | Motor stall torque |
| k | Spring coefficient at the actuation unit |
| x | Displacement of the slider |
| $w_M$ | Motor no-load speed |
| $L_t$ | Total length of the actuator |
| $l_{STA}$ | Length of the slider tendon linear actuator |
| $D_{stroke}$ | Stroke of the actuator |
| $A_t$ | Actuator total cross-section area |
| $A_{motor}$ | Initial cross-section area of the motor |
| $a_e$ | Cross-section area generated by movable pulley |
| $m_s$ | Mass of the slider |
| $\mu_b s$ | Friction coefficient b.t.w the rod and bushing |
| g | Gravitational acceleration |
| $T_0$ | Initial tension of the spring |
| $T_M$ | Tension of the end-effector tendon |
| | Initial tension of the spring |
| $\mu_s h$ | Friction coefficient b.t.w the wire and spring sheath |
| $\theta$ | Curved angle of the spring sheath |
| $\mu_{tf}$ | Friction coefficient b.t.w the wire and Teflon tube |
| $\mu_b$ | Friction coefficient b.t.w the wire and bearing |

**Table 3.2:** Classification of tendon driven under-actuation mechanism with position or force constraints.

| | **Kinematic constraints** | **Kinematic constraints with spring** | **kinetic constraints** |
|---|---|---|---|
| **Actuation length** | $\Delta x_i = r_i \Delta X$ | $\Delta x_i = \frac{F_i}{K_i} r_i \Delta X$ ($F_i$ is 0 when the joint $i$ is not under contact) | *unknown* |
| **Joint angle** | $\Delta\theta_i = J_{T,i}(\Delta x_i)$ $= J_{T,i}(r_i \Delta X)$ | $\Delta\theta_i = J_{T,i}(\Delta x_i)$ $= J_{T,i}(\frac{F_i}{K_i} r_i \Delta X)$ | *unknown* |
| **Wire tension** | *unknown* | *unknown* | $F_i = R_i F$ |
| **Joint torque** | *unknown* | *unknown* | $\tau_i = J_{T,i}^{-1}(F_i)$ $= R_i J_{T,i}^{-1}(F_i)$ |

**Table 3.3:** Indicators for the kinetic constrained under-actuation mechanism

| Indicator | Mathematical expression | |
|---|---|---|
| $\mathrm{I}_{\text{adaptability}}$ | $\lvert T_1 + T_2 - T_3 - T_4 \rvert$ | (3.4) |
| $\mathrm{I}_{\text{torsional-resistance}}$ | $max(\lvert T_1 - T_2 \rvert, \lvert T_3 - T_4 \rvert)$ | (3.5) |
| $\mathrm{I}_{\text{reliability}}$ | $max(f_1, f_2, f_3, ...f_n)$ | (3.6) |
| $\mathrm{I}_{\text{efficiency}}$ | $\frac{W_{finger}}{W_{motor}}$ | (3.7) |

**Table 3.4:** Normalized indicators for the kinetic constrained under-actuation mechanism

| Indicator | Mathematical expression | |
|---|---|---|
| $N.I_{\text{adaptability}}$ | $w_a(1 - \frac{(\lvert T_1 + T_2 - T_3 - T_4 \rvert)}{100})$ | (3.8) |
| $N.I_{\text{torsional-resistance}}$ | $w_t(1 - \frac{max(\lvert T_1 - T_2 \rvert, \lvert T_3 - T_4 \rvert)}{50})$ | (3.9) |
| $N.I_{\text{reliability}}$ | $w_r(1 - \frac{max(f_1, f_2, f_3, ...f_n)}{T_M})$ | (3.10) |
| $N.I_{\text{efficiency}}$ | $w_e(1 - \frac{W_{finger}}{W_{motor}})$ | (3.11) |

# Chapter 4

# Design Process of Exo-Glove II

## 4.1. Background

This chapter deals with a design process of the Exo-Glove II. As introduced in the chapter 1, the main goal of the thesis is to develop an tendon-driven under-actuated soft hand wearable robot that assists the thumb, index finger and middle finger with small number of actuators. Unlike the previous research, the under-actuation mechanism of the Exo-Glove II is located in the Slider-Tendon Linear Actuator as introduced in the chapter 2. Also, for the tendon routing of the index and middle finger, optimized tendon routing is used as explained in the chapter 3. This chapter mainly shows design method to obtain the tendon routing with small number of actuators (i.e, method to design the robot that assists three fingers with four actuators) and design method of the robot itself (i.e, methodology to fabricate the proposed robot); The tendon routing method is explained in the section 4.2 and the robot fabrication method is described in the section 4.3. More details about each contents are described in the following sections.

## 4.2. Under-actuated Tendon Routing for Exo-Glove II

In the under-actuated tendon driven wearable robot development, as explained in the chapter 1, the robot design framework in this thesis starts from considering the target body part. Since the Exo-Glove II is for the hand assistance, we considered for the thumb assistance because the thumb roles a lot when grasping or manipulating the objects. For more detail, the thumb opposition, a motion that the thumb locates in a opposite direction of the other fingers, is the most important motion in the grasp (Nanayakkara *et al.* 2017). Therefore, Exo-Glove II was designed to assist the thumb opposition motion for grasping various objects. Then, how can we design the tendon routing of the robot or decide the number of the actuator for the thumb opposition?

For the above question, it is quite obvious that the increased number of actuators with complicated tendon routing could give a chance to perform various tasks. However, it is also true that the increased number of actuators will increase the cost in robot development because of expensive controllers and actuators. One can think that this question could be answered by considering the human muscle-tendon systemKim & Park (2018); Lee *et al.* (2014). The use of biomimetic design method is also a good design method to make motion but it could reduce the usability of the robot because the hand is redundant system with lots of muscles and tendons; Therefore, the robots are usually used for the rehabilitation purposes rather than the assist purposes. As an alternative, tendon routing of the Exo-glove II is designed by considering the functional degree of freedoms (fDOFs) obtained in the several bio-mechanic studies; In the case of the thumb motion, the functional DOF is known as two (i.e, flexion/extension and abduction/adduction) while the fDOFs of the other fingers are known as one (i.e, flexion/extension). To make the above three motions (thumb abduction/adduction, thumb flexion/extension, and other fingers flexion/extension), basic tendon routing of the Exo-Glove II could be expressed as Figure. 4.1. Since the tendon can only transmit the pulling force, two tendons are required to make one degree of freedom motion. Therefore, total six tendons are used for the above motions. Here, as the Exo-Glove does, the proposed robot is also designed to assist index and middle finger using the under-actuation mechanism.

However, the robot design using six actuators could be quite excessive design yet. Increased number of actuators will harm the simplicity of the robot system and increase the robot price as well. Since the number of actuators could be reduced by using the under-actuation mechanism as explained in the chapter 2 and the chapter 3, we have additional chance to make the Exo-Glove II more compact. For simplification, a theoretical background, that $n+1$ numbers of actuators are required to make $n$ DOFs motion in tendon transmission, is used (Ozawa *et al.* 2014). Actually, the use of this theoretical background could induce a wrong result in this case because the theory requires an assumption, that the moment arm of the tendon should be constant, is not satisfied in the Exo-Glove II. Therefore, use of $n + 1$ numbers of actuators for $n$ DOFs in Exo-Glove II requires additional validation. This given theoretical background is only used for an initial guess. In our robot, Exo-Glove II, it was decided to use four actuators because our target application requires three functional DOFs (thumb abduction/adduction, thumb flexion/extension, and other fingers flexion/extension).

With the above guess, the Exo-Glove II with modified tendon routing is designed as Figure 4.2 using four Slider-Tendon Linear Actuators. As shown in two figures (Figure 4.1 and Figure 4.2), these two tendon routings have the same tendon routing but the only difference is how each tendon is connected to the actuator part. In the tendon routing using four actuators, kinetic constraints are applied on 1) flexion tendon of the index/middle finger and flexion tendon of the thumb and 2) adduction tendon of the thumb and extension tendon of the thumb. Since the kinetic constrained under-actuation mechanism (i.e, differential mechanism) is included in the Slider-Tendon Linear Actuator, the design of reducing the actuator does not affects in increasing the complexity of the glove part.

Although the kinetic constrained under-actuation is applied, we have to think whether the proposed design shows sufficient performance compared to the tendon routing that uses six actuators. It is because of the fact that the moment arm of the Exo-Glove II is not a constant as mentioned above. Therefore, additional validation is performed and these are all explained in the result section 4.4, after explanation of other robot design components.

## 4.3. Robot Design

With given tendon routing introduced in the section 4.2, this section describes a method of fabricating the robot with given tendon routing. For the successful robot design, we have to consider the robot requirements and characteristics. Wearable robots have several different characteristics compared to the other robots because the robot should be worn on the human body and should interact with the human body. The actuation of wearable robot could be considered as a process of transmitting the mechanical energy of the robot from the robot to the human body. The total system could be thought as an incorporation of two different system:

the robot and the human; The concept is usually named as *pHRI* (De Santis *et al.* 2008). For the successful incorporation between the robot and the human body, robot kinematic model should be designed with consideration of the human kinematic model; When the center of rotation of the robot joint and the human joint is not aligned, for instance, the user could feel inconvenience because of the difference between the robot configuration and the human kinematic configurationArno H. A *et al.* (2009); Cempini *et al.* (2015*b*). These are usually solved using the *joint alignment mechanism*, but it requires certain amount of spaces so that the robot could be bulky.

For this incorporation without increasing the robot size, several researches have proposed a method of designing wearable robot with soft materials such as silicone or garment (In *et al.* 2015; Kang *et al.* 2019). The use of softness provides an adaptability to the robot as mentioned in the chapter 1; Actually, the robot kinematic is not defined in the soft robot and the kinematic of the robot is defined by the external environment. Therefore, in the soft wearable robot, we only need to care about human kinematic unlike the conventional rigid wearable robot. Due to the fact that the use of soft material solves the annoying problem about the matching human kinematics and the robot kinematics, lots of soft wearable robots have been developed for various purposes.

However, the robots using soft material suffer from several difficulties (i.e, Deformation of the robot, manufacturing method, and pressure concentration on body) due to their inherent characteristics. For instance, the robot deforms when the force is applied to the robot; The deformation makes us difficult to estimate the relationship between the actuation force and the torque applied on the joint. Also, the robot with soft material is quite difficult to manufacture because it requires sewing or molding, which were not used in the manufacturing process of the rigid robot.

In this section, we propose a Exo-Glove II design methodology which uses both soft and rigid components by considering the requirements of each components. To do so, this section is described in terms of the components required for the robot operation. In this thesis, the robot components are classified into three major components: *body*, *router*, and *tendon anchor*; The design process is described in terms of these three components. Briefly speaking, the robot body is defined as a component that roles to fix the other components as explained in the subsection 4.3.1; Since the robot in this thesis has a glove type, the body could be thought as a glove. The second component, named as *router*, is a component which fix the wire path; Details are described in subsection 4.3.2. The last component is a *tendon anchor* and this component is used to fix the both end side of the wire as shown in the subsection 4.3.3.

### 4.3.1. *Glove design*

The first component for the wearable robot is named as *body* and it roles to fix all the other robotic components. In the case of soft wearable robot for hand assistance, a glove is well used because the softness of the robot body provides an advantage to reduce the size by its adaptability; Joint alignment mechanism could be removed and the robot body could be fitted well to the human body even the body size has slight difference as explained in the introduction chapter. The basic fabrication method of the robot body is similar to that of the conventional gloves, except the fact that several components (i.e, router and anchor) should be easily attached to the glove. Therefore, in the design process of the body part, a method of attaching these components to the body should be considered. Details of how each component is attached and is designed are explained in the following sections.

#### 4.3.2. *Router design*

The second design component named router is a component which fix the tendon routing. Since the joint torque is highly related to the wire tension and moment arm (i.e, the joint torque is equal to the cross product between the moment arm and tension of the tendon), the role of the router could be explained as a transmission between joint rotary motion and tendon linear motion. In general, two kinds of routers (i.e, pulley type router and conduit type router) are used in the tendon transmission. In the soft wearable robot, conduit type router is preferred because it has advantage of being attached easily in the soft components (In *et al.* 2015). Unlike to the robot body, one thing we should consider in the router design is that the consideration of the joint alignment issue is not mandatory. It is because the routers can perform given functions even they are attached on the bone rather than the joint; It could be better understood with a schematic view as shown in the Figure 4.6. This section will discuss a method of attaching the router to the robot body before explaining the router configuration because the attachment method affects a lot to the design process.

In the previous wearable robots, the routers were attached by hand-sewing (In *et al.* 2015) or by silicone molding (Kang *et al.* 2016). In the case of hand-sewing method, it is possible to make compact robot because this method makes strong bond between the router and the glove even the bond has thin structure. However, the hand-sewing method is time-consuming and inaccurate method, so that the robot performance highly depend on the manufacturer's skill. On the other hand, the method of using silicone shows relatively uniform performance because they are designed in an all-in-one method (i.e, method of manufacturing all the components in a single process) and therefore we do not need to think about the attachment method. However, because the products using silicone molding are relatively weak compared to the designs using garments, the robot body should be designed thicker.

In this thesis, as an alternative method of attachment, a method of using mechanical fixation with a hanger is proposed as shown in the Figure 4.3. In this method, the hanger is combined with the robot body in the manufacturing process of the robot body using a sewing machine. After that, the routers are attached to the hanger via bolt connection. Indeed, the use of bolt connection has a trade-off issue compared to the sewing method. The use of bolt makes much more easy to attach the router but it makes the robot bulkier than the method of using sewing method; The router with bolt connection requires at least 5mm while the sewing method almost does not require additional space. However, we determined to use the bolt connection because the routing of the extension tendons requires relatively big moment arm (Kim & Ryu 2020); Since the router should have certain amount of height to sustain the moment arm, the use of the bolt connection does not cause problem.

With a given connection method, the overall routers have been developed as shown in the Figure 4.4. Here, main components of the router are nut holder, bolt holder, and wire router as expressed in the Figure 4.4 (b). By tightening the bolt, the bolt holder and nut holder is fixed to the hanger that is attached on the glove. The bold holder and the nut holder is fabricated with the 3D printer and the wire router is made with inextensible garment; Overall view is expressed in the Figure 4.4 (c). The wire router is designed to have three spaces using the sewing machine as shown in the Figure 4.4 (d). The hole at the bottom side is used to fix the tendon routing of the flexion tendon and the other two holes at the both end side are used to fix the router itself to the nut holder as shown in the Figure 4.4 (b). In addition, the bolt holder is arch shaped to reduce the pressure applied on the human body, because it contacts with the finger.

The above router is designed with a combination of rigid material (i.e, nut holder and bolt holder) and soft material (i.e, wire router). The rigid components are used to fix the whole router to the robot body using a bolt connection while the soft component is used for the tendon path; Rigid components are used for easy, accurate fabrication and the soft components are used to endure force with thin structure. Since two different materials with different characteristics are used in the router, the router is named as *hybrid router* in this thesis.

In the case of the thumb router, different design should be applied because the thumb motion has different requirement; Our target goal of the thumb motion is opposition motion which requires both flexion/extension motion and abduction/adduction motion but the router in the previous paragraph is only designed for the flexion/extension motion. The thumb router is described in the Figure 4.5. When designing the router for two degree of freedoms, it is important to consider that the router should be well fixed to the human body. It is because, the relative position of the router against the human body could cause unwanted motion as shown in the Figure 4.5 (c) and (d).

The thumb router also has an unique characteristic that the router also roles as the tendon anchor. It is because the abduction and adduction tendon should be fixed to the thumb router. Indeed, fixing the end of wire at the router is not a big problem; By making eight figure knot, it is quite easy to fix the wire to the router. The eight figure knot is selected because it can endure high tensile force (Horigome *et al.* 2018*b*). In this thesis, the thumb router is designed not only to fix the end of the tendon but also to have a function of tightening itself to make sufficient fixation against the human body. Since the wire routing method of flexion tendon and the extension tendon is introduced in the previous paragraph, we concentrated to show the method of designing abduction tendon and adduction tendon.

The routing method for the abduction and adduction tendon is described in the Figure 4.5 (c) and (d); Indeed, since the end of the abduction and adduction tendon is fixed to the thumb router, it could be more accurate to describe as 'anchoring', but the word 'routing' is used not to confuse the readers. As shown in the Figure 4.5 (b), the tendons are fixed after being routed to wrap the router. This method of anchoring and routing enables the router to squeeze the human body when the tendon is pulled. Therefore, we can fix the router strongly to the body when the tendon is activated. Using this method, it was possible to transmit the tension to the human body even the joint have numerous degree of freedoms. Since the proposed routers all use both rigid and soft materials, we named Exo-Glove II as a *hybrid wearable robot*. By using the last component introduced in the next subsection, the Exo-Glove II has been developed.

#### 4.3.3. *Tendon anchor design*

The last design component is named as a tendon anchor and this component is located at the both end side of the tendon. A concept of the tendon anchor is easier to understand when it is explained as a buoy that defines the section which wire tension applies; The wire tension only applies to the joints that are located between two different tendon anchors. In the tendon transmission which uses Bowden cable, one tendon anchor is an anchor that fix the one end of the tendon while the anchor at the other side is an anchor that fix the Bowden cable as shown in the Figure 4.6. For instance, in the proposed hand wearable robot, one side of the tendon anchor is located at the end of the finger to fix the end of the tendon while the other tendon anchor is located at the wrist side to fix the Bowden cable.

Tendon anchor at the finger side is just designed similar to the tendon router because it has quite similar requirements with tendon router. On the other hand, in the case of the tendon anchor at the Bowden cable side, it has quite different characteristics. This anchor is usually named as Tendon Anchor support ( i.e, TA support) in the previous researches (In *et al.* 2015). In this thesis, we are going to call it just as a wrist tendon anchor. Wrist tendon anchor plays an important role on force equilibrium. It can be easily understood if we look for the force relationship shown in the Figure 4.6. The tension of the tendon roles to pull the whole hand as shown in the Figure 4.6 (a). Therefore, the user has to sustain the hand not to be pulled. On the other hand, the motor part should be fixed to the ground because the tendon also pulls the motor part towards to the human body. One easy way to solve this problem is to use a wrist tendon anchor shown in the Figure 4.6 (d); The hand and the motor part will push each other so that the force equilibrium can be easily accomplished.

One thing we should consider is that the total wire tension will be concentrated to the wrist so that it applies high pressure on the skin (Kang *et al.* 2012). Therefore, soft wrist tendon anchor has been developed as shown in the Figure 4.7 (a). In the wrist tendon anchor design, soft materials are used to reduce the pressure applied on the skin. The anchor is designed to deform according to the body shape as shown in the Figure 4.7 (b).

The tendon anchor not only roles to reduce the pressure applied on the skin, but also to measure the wire tension by containing the tension sensor. Indeed, the advantage of including tension sensor is originated from the tendon routing method that is designed in the chapter 3. By using the TR3 in chapter 3, the Exo-Glove II can measure the wire tension at the glove using the tension sensor that is attached on the glove part rather than the actuator part. With the given configuration, it was possible to control the end-effector tension more accurately; Since the friction at the Bowden cable which is located between the glove and the actuator is not measurable, the end-effector tension is difficult to be controlled using the tension at the actuator. The tension sensor is designed as shown in the Figure 4.7 (d) and the sensor are contained in the router as shown in the Figure 4.7 (a). Advantage of using tension sensor at the end-effector can be found in the Figure 4.14.

Finally, using the robot components introduced in the subsection 4.3.1 - 4.3.3, Exo-Glove II has been developed. After the development, the robot was validated with several experiments shown in the section 4.4.

## 4.4. Validation

### 4.4.1. *Opposition workspace*

In order to show that the robot design using only four Slider-Tendon Linear Actuators is sufficient, validation about the workspace is performed; The theoretical guess of reason for using four actuators are described in section 4.2. Here, a concept of *opposition workspace*, a workspace that is defined as an overlapped workspace of the thumb and index finger, is used (Li *et al.* 2016). The opposition workspace according to the actuator number are described in Figure 4.8. This figure shows that the increase of the actuator number also extends the opposition workspace. The relative opposition workspace size can be seen in the Figure 4.9. As shown in the figure, the relative workspace area increases a lot when the actuator number changes from three to four. One might wonder that the workspace area could be differ when the subject changes because the workspace area depends on the hand size. To check whether the workspace is subject-dependent or not, additional experiment about subject dependency is conducted as shown in the Figure 4.10. The result shows that the size of the opposition workspace changes as well as the shape of the opposition workspace and exact value of the result is described in the Table 4.1. However, since our goal is to consider the relative area of the case using four actuators to the area of the case using six actuators, the relative area is obtained as well. Here, we can figure out that the relative area is not affected a lot to the subject.

### 4.4.2. *Maximum grasping force*

Since the opposition workspace in the subsection 4.4.1 only shows kinematic performance, additional experiment that can measure the grasping force is performed. In hand wearable robot, there are numerous method to measure the robot performance in force domain. In general, fingertip force is measured to figure out the robot performance in the force domain (Kang *et al.* 2019; In *et al.* 2015). However, in terms of theoretical view, it is not suitable for the validation of the under-actuated robot because the robot has limitation in increasing the fingertip force while maintaining the posture (Birglen & Gosselin 2006). Indeed, making fingertip force in a single contact point is not important in practical grasping (Lynch & Park 2016). Instead, satisfying the force closure condition by increasing contact points with the object is a way to increase the stability of the grasp. Therefore, if there are $n$ number of contact points, then the sum of the contact forces ($N_i$) can be an indicator of the grasp stability. Its mathematical expression can be described as Eq (4.1).

$$P_{force} = \sum_{i=1}^{n} f(N_i) \tag{4.1}$$

Therefore, this thesis propose a new experimental method to measure the grasping force as shown in the Figure 4.11. The experiment is designed to measure the wire tension when the object starts moving. In this situation, the sum of contact force can be expressed by dividing the wire tension with friction coefficient as Eq (4.2).

$$\sum_{i=1}^{n} f(N_i) = F_L/\mu_k \tag{4.2}$$

With given equation, experiment is conducted as shown in the Figure 4.13 (a). Since the wearable robot should be operated after being worn on the human hand, the human intention could be included in the experiment. Therefore, we tried to exclude the intention by using the robotic dummy hand. The dummy hand is described in the Figure 4.12. With the given dummy hand, experiments were conducted under several tension conditions (5N, 10N, and 20N) for five times. The experimental result is expressed in the Figure 4.13 (b) and Table 4.2. Here, the dynamic friction coefficient between the object and the garment (Neoprene) was used to figure out the grasp force from the wire tension. The friction coefficient was measured by other experiment as 0.083.

4.4.3. *Tension control*

As explained in the section 4.3.3, the tension sensor is installed in the wrist anchor to measure the end-effector wire tension more accurate. For the validation, this section shows the tension at the end-effector in the situation of feedback control by tension sensor at the actuator (Figure 4.14 (a)) and by tension sensor at the end-effector (Figure 4.14 (b)). As shown in the figure, the control performance increases when the tension sensor is located at the end-effector. Here, velocity based admittance control is used to control the tension as shown in the Eq (4.3).

$$v_{ref} = k_p(F_{ref} - F) + k_d\dot{F} \tag{4.3}$$

## 4.5. Discussion & Conclusion

This chapter deals with the method of designing the hybrid hand wearable robot that uses four Slider-Tendon Linear Actuators. By using the under-actuation mechanism adequately, it was possible to sustain the robot performance compared to the performance of the robot that uses six tendon-driven actuators. For the performance comparison, a concept of opposition workspace is used. The size of the opposition workspace in terms of the actuator number is obtained. As shown in the result, the size of the opposition workspace increases a lot when the number of actuator increases from three to four. Since monte-carlo method is used to obtain the area of the workspace(Li *et al.* 2016), it is quite difficult to explain the reason why the workspace area increases when the number of actuator is four. One we can infer is that it is because of the tendon transmission characteristic that the required number of the actuator is $n + 1$ when the required degree of freedom is $n$.

The robot design in this chapter is explained by classifying the robot components into 1) robot body, 2) tendon router, and 3) tendon anchor. The detail explanation was also conducted according to the robot components. In this thesis, a method of using both rigid and soft materials in the robot design to increase the robot performance. By using this hybrid method, it was possible to simplify the robot fabrication method. Also, to make the motion which has two degree of freedoms, a tendon router that can tighten itself is developed. By doing so, it was possible to transmit the joint torque more accurately.

In addition,the tendon routing that locates the end of the tendon not in the actuator but to the end-effector is used in the Exo-Glove II; The tendon routing was obtained in the chapter 3 and it was named as TR3 in the previous chapter. Then, by attaching the tension sensor at the tendon anchor, the proposed robot show better control performance. Since the end of the tendon is located in the end-effector, it was possible to measure tension in a compact space.

Although various performance of the Exo-Glove II is described in this chapter with the robot development, the method of making hand motion with Exo-Glove II is not explained here. The contents about how to generate motion are described in the next chapter. Since the motion generation with wearable robot requires to consider the human characteristics, method of considering the human characteristics are also included in the next chapter.

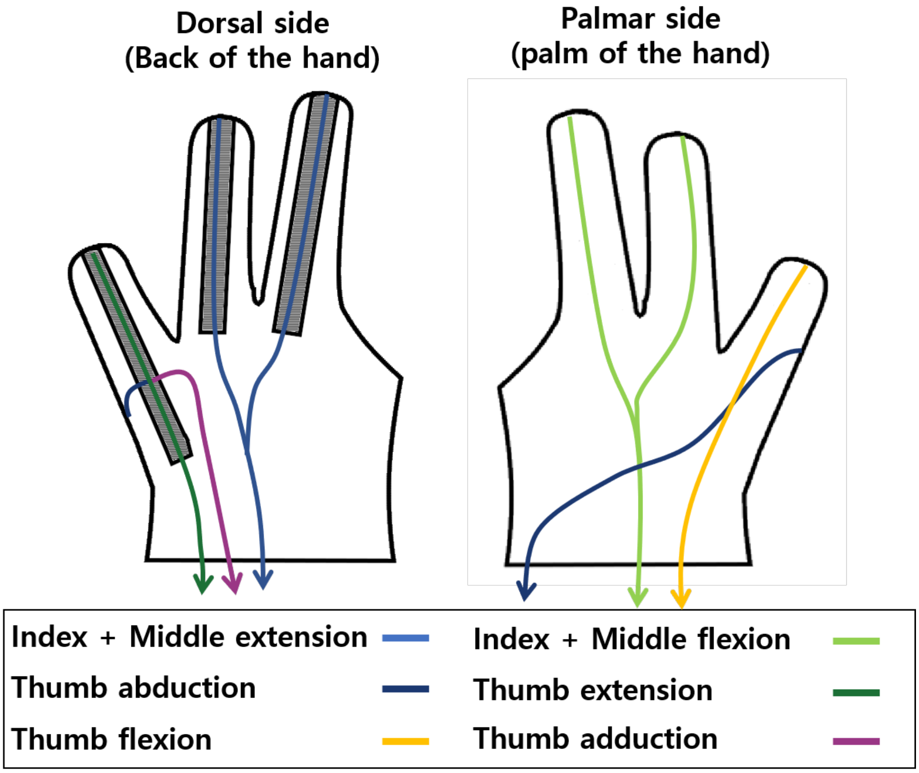


**Figure 4.1: Schematic of tendon routing that uses six tendon-driven actuators**

The tendon routing is designed to use four tendons for assisting the thumb and two tendons for the index and middle finger. By doing so, the glove assists index and middle finger flexion/extension and the thumb opposition.

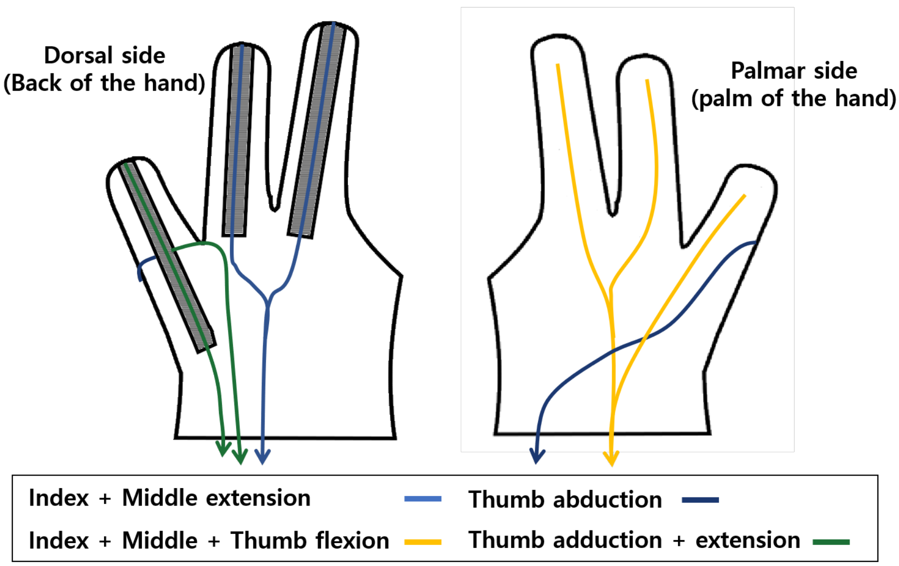


**Figure 4.2: Schematic of tendon routing that uses four tendon-driven actuators**

The tendon routing also uses same number of tendons with the case of the tendon routing in Figure 4.3. However, several tendons are coupled and these are under-actuated in the actuator part; Here, Slider-Tendon Linear Actuators are used for the under-actuation mechanism.

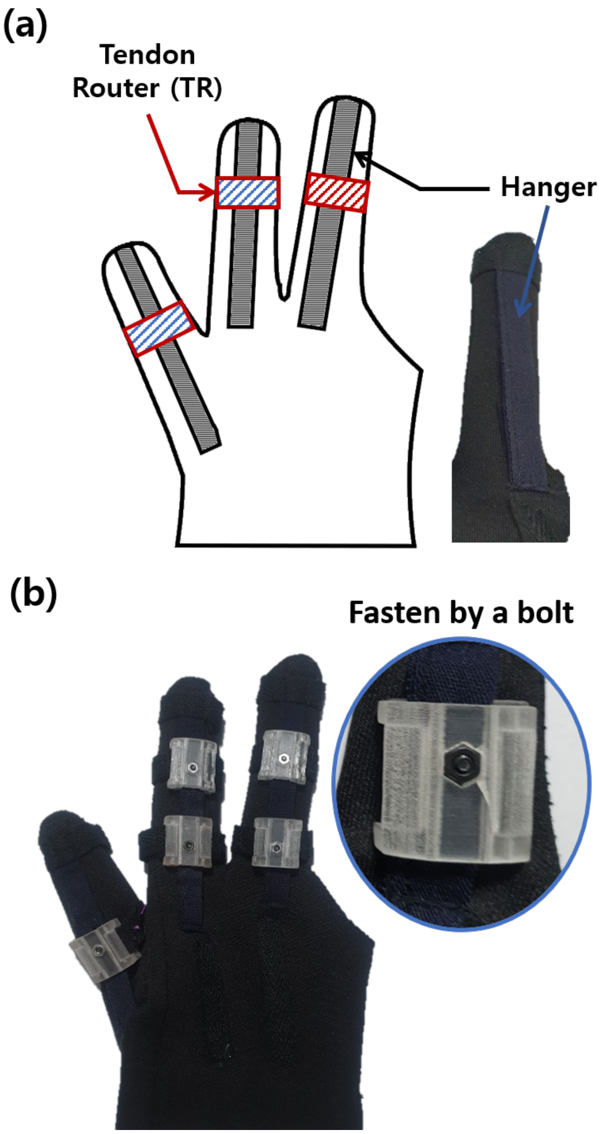


**Figure 4.3: Overview of the Exo-Glove II**

**(a)** shows the brief schematic and a method of using hanger to fix the router to the glove; **(b)** shows the real view of the Exo-Glove II. As shown in the figure, the rigid routers that are used to fix the wire path are connected to the glove by bolt and hanger.

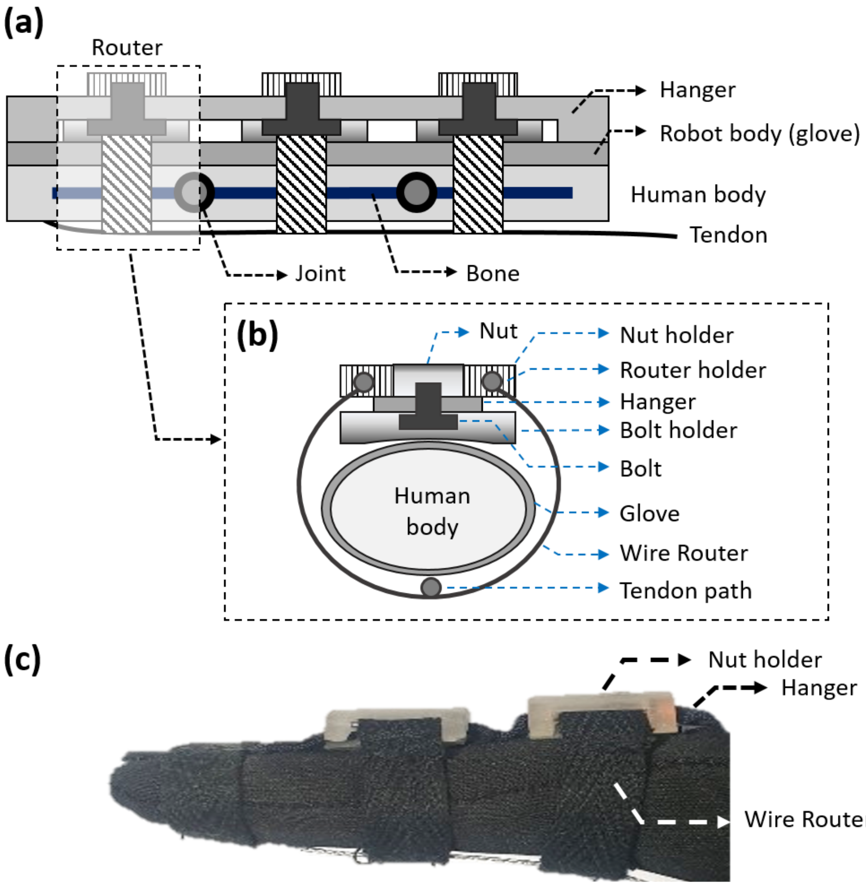


**Figure 4.4: Overview of the tendon router**

**(a)** shows the overall schematic to show how the router is located in the robot; **(b)** shows the detail that shows how the router is designed. **(c)** shows how the router is attached in a real robot.

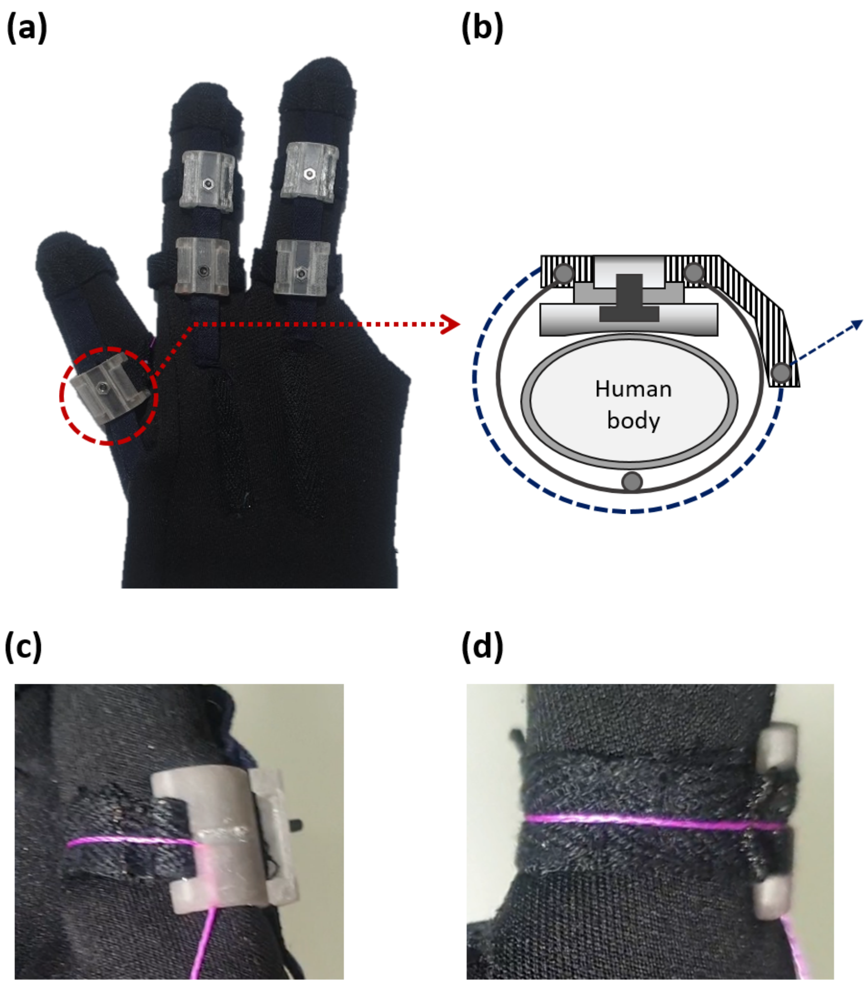


**Figure 4.5: Overview of the tendon router for the thumb**

**(a)** and **(b)** show the overall router design. In the **(b)** blue, dotted arrow is a abduction tendon. Since this tendon surrounds the router, the activation of the tendon will not only make the motion but also fix the router to the human body; **(c)** shows how the router is attached in a real robot. We can find that the abduction tendon not only roles to make the motion but also to fix the router to the human body as shown in **(d)**

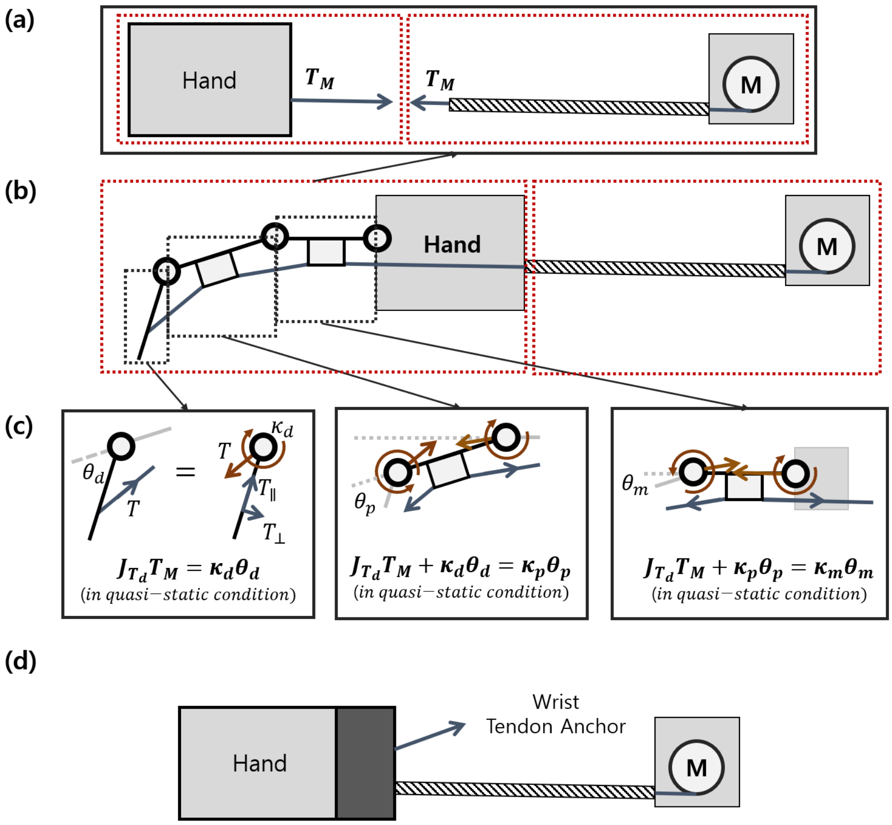


**Figure 4.6: Overview of the tendon anchor**

**(a)** and **(b)** show the overall force relationship between the end-effector part and the actuator part. **(c)** shows the force relationship in each joints. **(d)** shows how wrist tendon anchor is located.

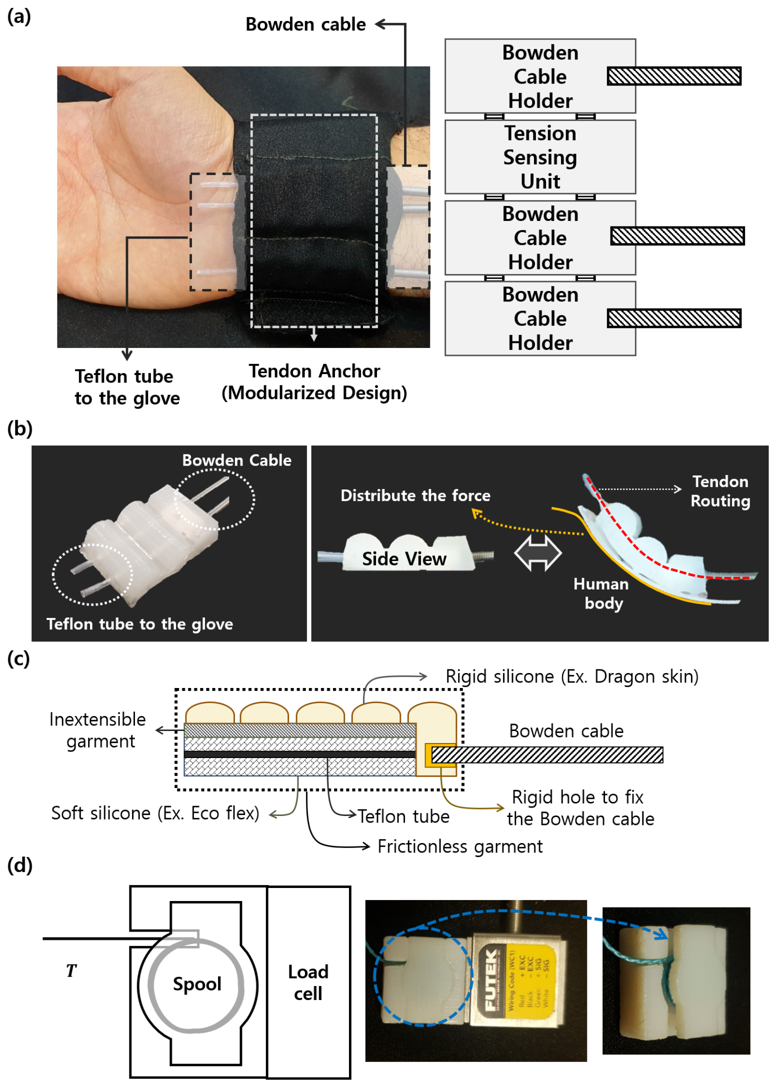


**Figure 4.7: Overview of the tendon anchor**

**(a)** shows the overall view of the tendon anchor; **(b)** shows the method to distribute the force applied on the skin; **(c)** shows a schematic view to show how the tendon anchor is fabricated; and **(d)** shows the tension sensor that is located to the tendon anchor.

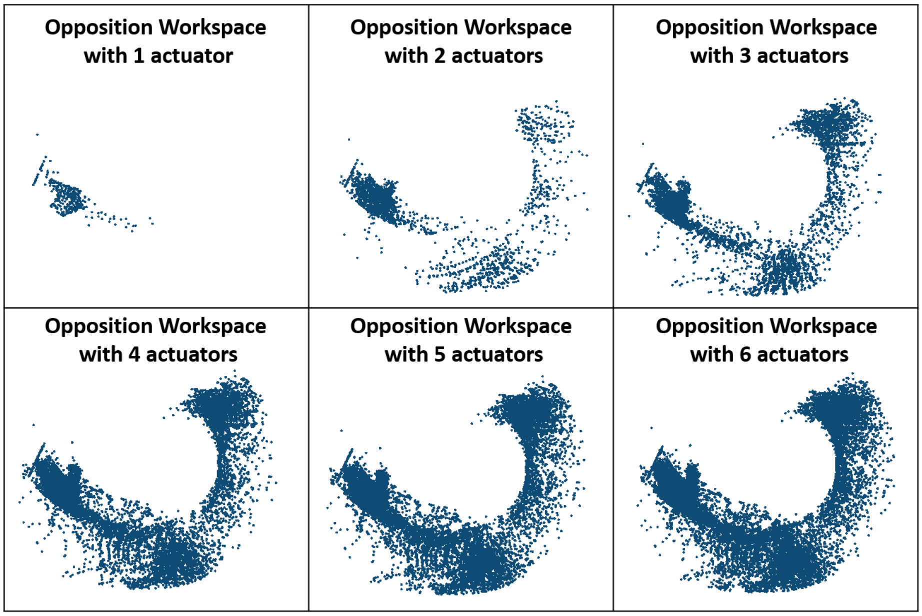


**Figure 4.8: Opposition workspace in terms of the number of tendon-driven actuator.**

Validation used to show that how the reduced number of tendon-driven actuator affects to the opposition workspace. As shown in the figure, the opposition workspace changes as the number of actuators differ; Exact area of each opposition workspace is described in the Figure 4.5.

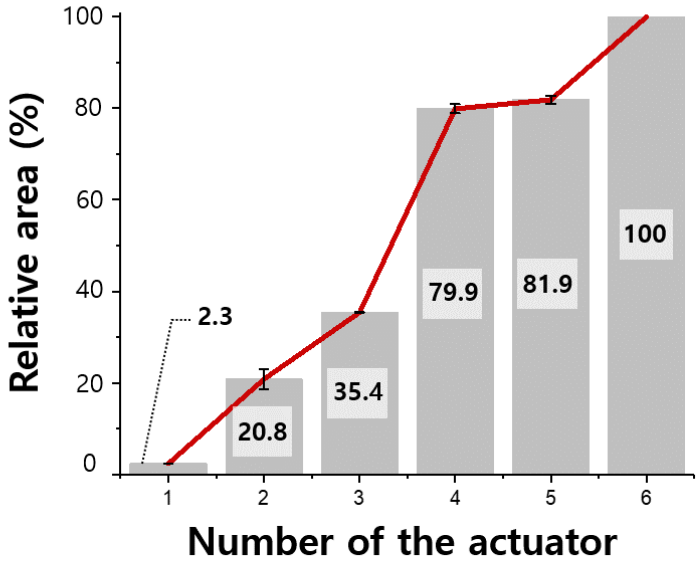


**Figure 4.9: Simulated result of the opposition workspace area.** A bar graph to show the relative area of the opposition workspace in terms of the number of actuators. As it can be seen in the graph, the relative area of the opposition workspace increases a lot when the number of the actuator changes from three to four.

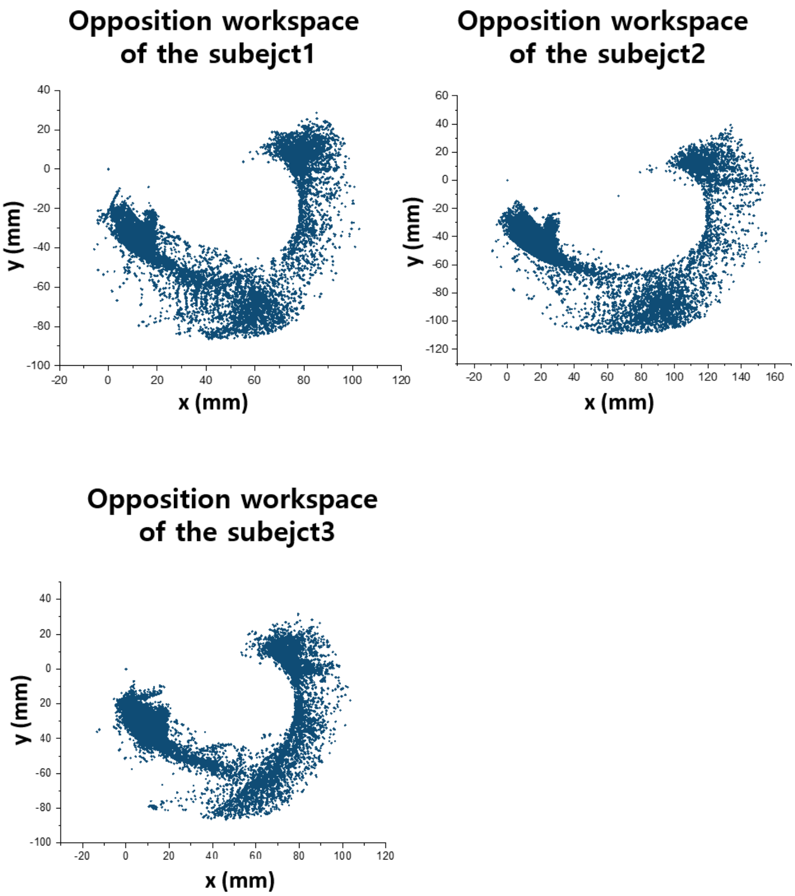


**Figure 4.10: Opposition workspace according to the subject**

Since the workspace depends on the hand size, additional simulation is conducted to find out how the opposition workspace changes as the subject differs. The actual size of the opposition workspace differed as the subject changed but the relative area, which is our main indicator, was not changed significantly.

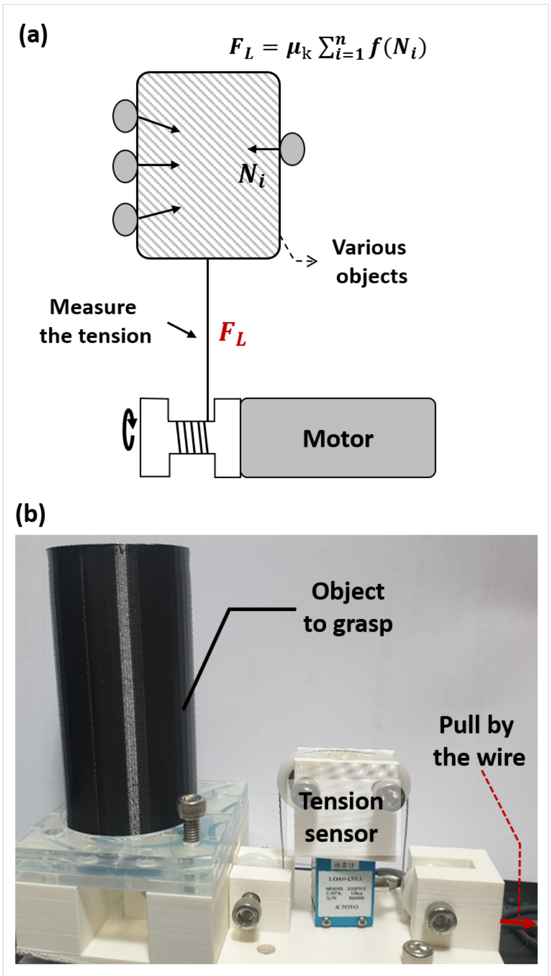


**Figure 4.11: Experimental setup to measure the grasping force** **(a)** shows a schematic view about the concept of the grasping force; The grasping force in the figure is total sum of the normal force, and it could be derived by dividing the lifting force $F_L$ with dynamic friction coefficient $mu_k$; **(b)** shows the experimental setup to measure the proposed indicator and a single tension sensor is used to measure the lifting force $F_L$.

**Figure 4.12: Dummy hand for the experiment**

**(a)** shows the dummy hand for the experiment. Since torsional spring is located in the hand joint, the dummy can substitute the human hand. **(b)** shows the Exo-Glove II that is worn on the dummy hand.

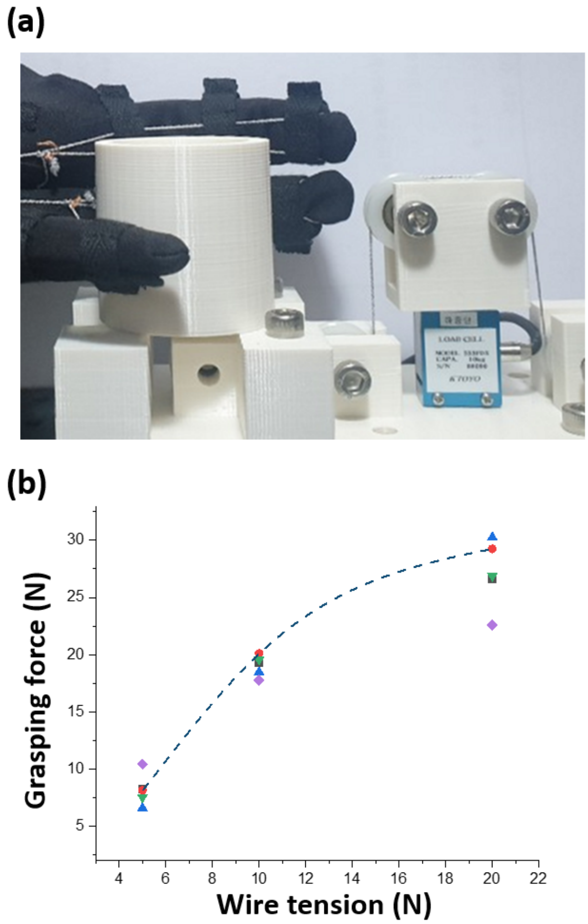


**Figure 4.13: Experimental result of the grasping force**

**(a)** shows how the grasping force is measured. Here, hand dummy is used for the accurate measurement; **(b)** shows the experimental result of the grasping force in terms of the wire tension. As shown in the graph, the grasping force was 24.08N when the wire tension is 20N.

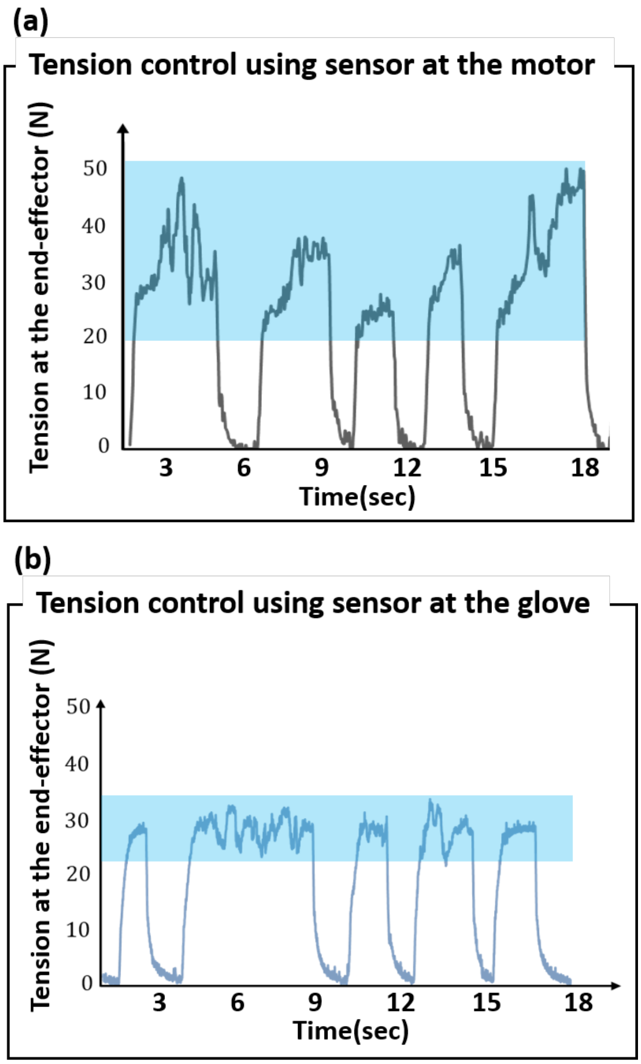


**Figure 4.14: Validation of the tension sensor at the end-effector** **(a)** shows how end-effector wire tension is controlled when the robot can only measure the wire tension at the actuator part; **(b)** shows the wire tension control method using the tension sensor at the end-effector. As it can be seen in the figure, **(b)** shows better control performance.

**Table 4.1:** Result of opposition workspace

| Subject Number | Subject 1 | Subject 2 | Subject 3 |
|---|---|---|---|
| Area of the opposition workspace using 4 actuators | 1406.6 ($mm^2$) | 1841.6 ($mm^2$) | 1353.5 ($mm^2$) |
| Relative area of the opposition workspace | 80.6 (%) | 84.9 (%) | 81.9 (%) |

**Table 4.2:** Result of grasping force

| Tension | Lifting force | Grasping force |
|---|---|---|
| 5 (N) | 0.65 (N) | 7.78 (N) |
| 10 (N) | 1.60 (N) | 19.24 (N) |
| 20 (N) | 2.24 (N) | 24.08 (N) |

# Chapter 5

# Motion Generation with Exo-Glove II

## 5.1. Background

In order to generate a motion with tendon driven robot, it is required to define not only the *Manipulator Jacobian* which explains an relationship between joint position and end-effector position but also additional mappings that shows an relationship between actuator position and joint position which can be named as *Actuation Jacobian*; Overall relationships can be described as shown in the Figure 5.1. The concept of Manipulator Jacobian is a familiar concept for robotic researchers and can be derived by solving forward/inverse kinematics of the system (Lynch & Park 2016). On the other hand, the relationship between joint torque and wire tension is only used in remote actuation because the joint torque is not directly applied by the actuator. In this thesis, this relationship is named as *Actuation Jacobian* by getting inspiration of the terminologies used in the other research (Kim *et al.* 2018). Unlike other robots, there are several difficulties in obtaining these two Jacobians in soft wearable robot with under-actuation mechanism. The Manipulator Jacobian requires to solve human kinematics, which is relatively complicated then the rigid robot. Also, the Actuation Jacobian requires to consider human joint stiffness, elongation of the robot body, and friction of the wire. In order to obtain these Jacobians even with the difficulties, this chapter provides a novel data-driven method to find out the Jacobians in section. In addition, the remainder of this chapter shows how the found Jacobians are used to control the proposed robot to generate a given motion in section.

## 5.2. Manipulator Jacobian

Unlike other rigid robots, the Manipulator Jacobian of the soft wearable robot is defined by human kinematics. Therefore, the Manipulator Jacobian can be obtained by measuring human body motion. Therefore, a method of calibrating kinematic information of human body is required for the analysis. For kinematic analysis, a concept of Product of Exponential (POE) formula is used and the theoretical background about POE is explained in the Appendix C. Briefly speaking, this section is about obtaining the relationship between joint angle and fingertip position; To derive this relationship, we have to know about the joint position. This relationship can be expressed as Eq (5.1). Here, $S$ and $\theta$ each denotes screw parameter and joint angle; Screw parameter is a parameter used in the POE and is defined by the kinematic structure of the robot and usually has a constant value. With these two variables, we can figure out the fingertip position ($X_{F.Tip}$).

$$\begin{aligned} X_{F.Tip} &= f(S, \theta) \\ \dot{X}_{F.Tip} &= J_m(S, \theta)\dot{\theta} \end{aligned} \tag{5.1}$$

Since the human joints are not exact revolute joints, additional work is required to define the kinematics. One well used method is using the simplified kinematic model that can represents the human motion (Weston B *et al.* 2000). In this method, by replacing a single but complex joint to the sum of several 1-DOF revolute or prismatic joints, the kinematic model could be developed similar to the conventional rigid robots as shown in the Figure 5.5. Even we use the kinematic model proposed by Weston B *et al.* (2000), additional calibration is required that matches the user kinematic data to the proposed kinematic model. Especially, the thumb requires this calibration because the thumb has complicated structure. Therefore, kinematic calibration is performed as shown in the appendix D. Also, the final result of the kinematic calibration for the thumb CMC joint is explained in subsection 5.5.1.

## 5.3. Actuation Jacobian

As described in the section5.1, in order to control the joint torque in tendon transmission, the concept of Actuation Jacobian should be considered. The mathematical definition of the Actuation Jacobian can be described as Eq (5.2).

$$\begin{aligned} q &= g(l) \\ \dot{q} &= J_a(l)\dot{l} \end{aligned} \tag{5.2}$$

When the tendon routing is fixed by using bearings, the Actuation Jacobian can be regarded as moment arm of the each tendon to the joints and is constant to the joint angle. However, in the case of conduit type tendon transmission, the Actuation Jacobian is not constant because the moment arm differs as the joint angle changes. Since the proposed robot in this thesis uses conduit type transmission for compactness, the analytical solution to obtain Actuation Jacobian in the conduit type tendon transmission is calculated as shown in the Figure 5.2.

Since the Soft Tendon Routers (components that fix the wire path as defined in the chapter 4) move along with finger, the position of the router can be derived as shown in Eq (5.3). $\vec{P}_i^{an}(q_i)$ in the equation is a position vector of the router in terms of joint angle ($q_i$) shown in Figure 5.2.

$$\vec{P}_i^{an}(-q_i) = Rot(-q_i)\vec{P}_i^{an}(0) = \begin{bmatrix} \cos(-q_i) & -\sin(-q_i) \\ \sin(-q_i) & \cos(-q_i) \end{bmatrix} \vec{P}_i^{an}(0) \quad (5.3)$$

Using the position of the Soft Tendon Router, the length of the moment arm can be derived by using the concept of the cross product, as in Eq (5.4).

$$R_i = 0.5\frac{norm(\vec{P}_{i-1}^{bm} \times \vec{P}_i^{an}(-q_i))}{|\vec{P}_{i-1}^{bm} - \vec{P}_i^{an}(-q_i)|} \quad (5.4)$$

Since the relationship between the joint angle and moment arm of the wire is non-linear, the finger configuration in terms of tension can be solved numerically, rather than analytically. One thing we can intuitively know about the relationship in Eq (5.4) is that the moment arm of the extensor wire could be shorter than that of the flexor, even if the router configuration is the same. For example, when the lengths of $a_i$, $b_{i-1}$, $m_{i-1}$, and $n_i$ are 5, 5, 3, and 3mm, respectively, the moment arm of the flexor and extensor wire can be described as shown in Figure 5.2. As shown in the graph, the moment arm of the flexor increases as the joint angle increases, while that of the extensor reduces. Further, the moment arm of the extensor becomes negative when the angle increases; this means that even if the tension of the extensor increases, extension may not occur. In a real-world situation, thanks to the finger structure, the moment arm of the extensor can be sustained larger than zero because the finger skin will prevent the situation where the moment arm would become negative. However, this situation is quite unstable because sometimes the glove can deform and the wire path may rotate to the side direction; this causes the moment arm to be negative. Therefore, it is safe to make the extensor moment arm larger than zero. This is possible by increasing the height of the soft router ($m_{i-1}$ and $n_i$). For instance, when $m_{i-1}$ and $n_i$ of the router increase to 5mm, it is possible to sustain the moment arm of the extensor larger than zero, even as the joint angle increases.

With a relationship between moment arm and joint angle, it is possible to obtain the relationship between joint angle and tension of the wire. note that, although a formal method uses relationship between joint angle and wire length in order to obtain Jacobian, this method uses a different kind of relationship. Some of the readers can feel awkward because the proposed relationship is defined between distance and force. However, since the proposed robot consists under-actuation mechanism and the system can be assumed as quasi-static condition, the proposed robot system shows different aspects with other robots. For more detail, the joint angle can not be defined only with the actuator pulled length because numerous joints move simultaneously even with one actuator. Here, decision of joint angle requires joint stiffness and wire tension as well. Also, even though the under-actuation mechanism is used, defining the relationship between joint angle and wire tension is still dangerous because of the dynamic momentum. However, thanks to the low inertia and acceleration, the concept of proposed Jacobian can be used. (i.e, When the dynamic term is not ignored, the joint angle can not be defined in to one using a force because the angle becomes a function of time.) This can be easily understood through the Eq (5.5), which is state equation about joint $q_i$, where $\kappa$ means joint stiffness and $I$ means inertia of the finger.

$$I\ddot{q_i} = R_i T - \kappa \Delta q_i \tag{5.5}$$

With the given Eq (5.5), we can infer that the joint angle $q_i$ is a function of moment arm ($R_i$), wire tension ($T$), and time ($t$) as shown in the Eq (5.6). Therefore, the Jacobian about joint angle and wire tension does not make sense in this moment.

$$q_i = f(R_i, T, t) \tag{5.6}$$

By using quasi-static condition, the term $I\ddot{q_i}$ in the equation is usually ignored because both $I$ and $\ddot{q_i}$ are small. Then, the joint angle of the finger can be simply expressed as Eq (5.7). However, since the joint stiffness ($\kappa$) is a human property that changes according to various factors (e.g, joint angle, age, sex, posture), solving Eq (5.7) is not a simple problem. Therefore, additional approach about using data driven method is proposed in section 5.4.

$$\Delta q_i = \frac{R_i T}{\kappa} \tag{5.7}$$

## 5.4. Joint Angle Estimation through a Tension and Stroke Measurement

As explained in the previous sections, in order to make grasp posture with the proposed robot, the relationship between joint angle and wire tension should be obtained. Therefore, data-driven method is proposed to induce the above relationship. Here, we measured joint angle and wire tension simultaneously to obtain the relationship. With the synchronized data, Gaussian Process Regression (GPR) is executed.

Since the proposed method is based on the data-driven method rather than model-driven method, gathering well-synchronized data is important. Since the motor is controlled under CANopen communication, the synchronization between motor data and Vicon data was executed by using additional Sync signal that is sent right after the CAN signal. The overall motor control with sync signal is depicted in the Figure 5.3.

With the data acquisition method described in the previous paragraph, experiment was conducted to measure the joint position and motor data. The experiment was conducted for a single person as a pilot study because the main goal is to show how the robot was developed and controlled, rather than its clinical contribution. Here, the experiment was divided into two steps. The first experiment was conducted to find out the hand kinematics and the second experiment was designed for stiffness parameters estimation. In the first experiment, a total of 14 markers were used for hand motion tracking, as shown in Figure 5.4. Here, 12 markers were used to measure the position and orientation of the index finger, while the remaining two markers were used to measure the position of the thumb. To measure the hand motion, eight motion capture cameras (Bonita10, Vicon) were used. With this marker configuration, joint configuration was derived using the concept of forward and inverse kinematics. In the first experiment, the participant was asked to move all possible ranges when moving his finger spontaneously.

After solving the kinematics of the hand, a second experiment was conducted to find out the relationship between the tension and joint angle. Here, we experimented with various tension conditions to see how the movement of the finger changed under different tension conditions. For loading of each actuation tendon, the maximum tension magnitude that maximizes the finger movement was initially measured. As a next step, the joint angle of the index finger was measured in a condition where the tension of one actuation wire was gradually increased while sustaining the tension of other actuation wires at 0, 33, 66, and 100% of the maximum tension.

## 5.5. Experimental Results

### 5.5.1. *Result of the kinematic System Identification*

Using the kinematic calibration method introduced in the section 5.2, the kinematic parameters of the thumb joint is calibrated. For the calibration, total 12 markers are used as shown in the Figure 5.5 (a). Since the CMC joint has three degree of freedoms, the kinematic model of CMC joint can be represented as Figure 5.5 (b). By solving the kinematic calibration, the screw parameter $S_1$, $S_2$, and $S_3$ were obtained. The result of the kinematic system identification is described in the Figure 5.6. As shown in the figure, the end-effector position error dramatically reduced after the calibration. The RMS error of the end-effector position can be found in the Table 5.1.

5.5.2. *Result of the Gaussian Process Regression*

As a result, the relationship between wire tension and joint angle are obtained as shown in Figure 5.7. In order to determine the relationship, motor encoder, motion data, and loadcell data was measured simultaneously. The relationship was obtained using Gaussian Process Regression; the results are shown in Figure 5.7. In this figure, (a), (c) and (e) show the tendency of the joint angle along with the regression results. Here, the x axis of the graphs means the number of data; the number of data in x axis means that i-th row of the x axis is i-th data in the data set. In order to show the accuracy of estimation, the relationship between estimated angle and ground truth angle is compared as shown in Figure 5.7 (b), (d) and (f). As the root mean square error (RMSE) in the figures show, the proposed estimation fits well in the ground truth angle.

In order to show the effectiveness of the stiffness parameter estimation, we also included additional result of comparison between the proposed estimation and the model-based estimation as shown in Figure5.8. As noticed in the Introduction section, since it is difficult to consider the elongation of the robot body or the human joint stiffness in modelling, we used constant value of stiffness and ignored the elongation of the robot body. This model-based estimation is derived using the result of Eq (5.4) and Eq (5.7).

With the given regression results, finally, the robot is controlled using the overall control scheme as shown in Figure 5.9. Overall control scheme of the proposed robot can be expressed as Figure 5.9. The high level control roles to find out the appropriate tension that makes grasp posture with given grasp mode. Since the proposed robot does not contain any additional vision sensor, the size of the object and grasp mode are decided manually. With given object size and grasp mode, target tension of four different actuators are induced by using the result of inverse kinematics and regression. After that, the tension is controlled by a low level controller using additional tension sensors designed with loadcells (LSB200, FUTEK). In this controller, admittance control is used; the tension is controlled by velocity, which is based on a PD controller with motor encoder, as shown in Eq (5.8) and Figure 5.9. (Whitney 1977)

$$v_{ref} = k_p(F_{ref} - F) + k_d\dot{F} \tag{5.8}$$

The resolution and maximum non-linearity of the tension sensing unit can be described as 0.004N and 0.2N, respectively. It can be derived from the resolution (0.002N) and maximum non-linearity (0.1N) of the loadcell installed in the tension sensing unit. This is because the friction of the wire at the tension sensing unit is negligible and the tension sensing unit is designed to measure twice of the wire tension. In addition, the resolution of the motor encoder can be described as 16 lines per revolution. Since the motor has 69:1 gear ratio, we can conclude that the resolution of the motor encoder is about 0.006 rad.

### 5.5.3. *Motion generation with Exo-Glove II*

Using the regression results in the subsection 5.5.2, it was possible to make various postures with Exo-Glove II. Here, admittance control is used to control the tension of the actuation tendon and the final result of generating the hand motion is shown in the Figure 5.10.

## 5.6. Discussion & Conclusion

In this chapter, a method to make grasp posture using the Exo-Glove II is explained. Unlike the other robots, motion generation of the wearable robot is quite complicated; It is because the human properties should be considered to make a robot model. In this chapter, a data-driven method is used to figure out the robot model. As a result, the Gaussian Process Regression is used to find out the relationship between joint angle and the wire tension. With the regression result, it was possible to obtain several grasp postures by tension control. Overall conclusion about the thesis is located as a final chapter.

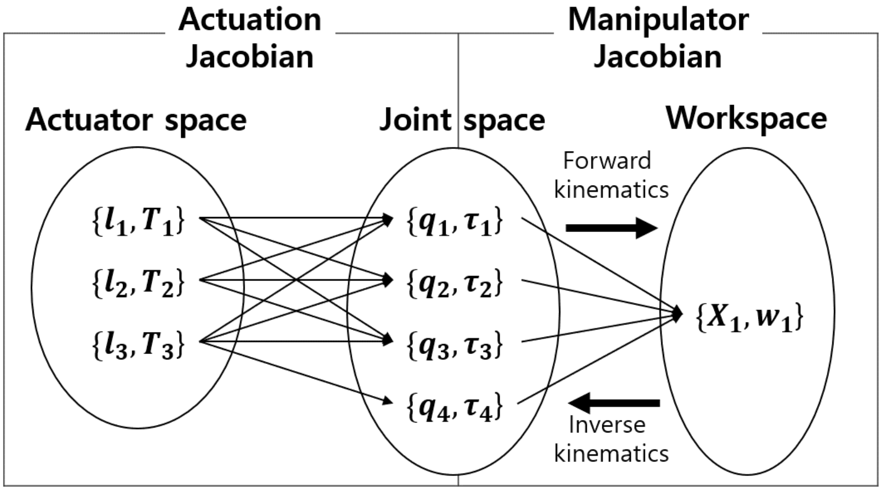


**Figure 5.1: Schematic that describes Actuation Jacobian and Manipulator Jacobian**

The relationship between the actuator space and the joint space (e.g, actuator stroke and joint angle) are defined by Actuation Jacobians. On the other hand, Manipulator Jacobians define the relationship between joint and the end-effector position; The concept of Manipulator Jacobian is same as that in the conventional robots.

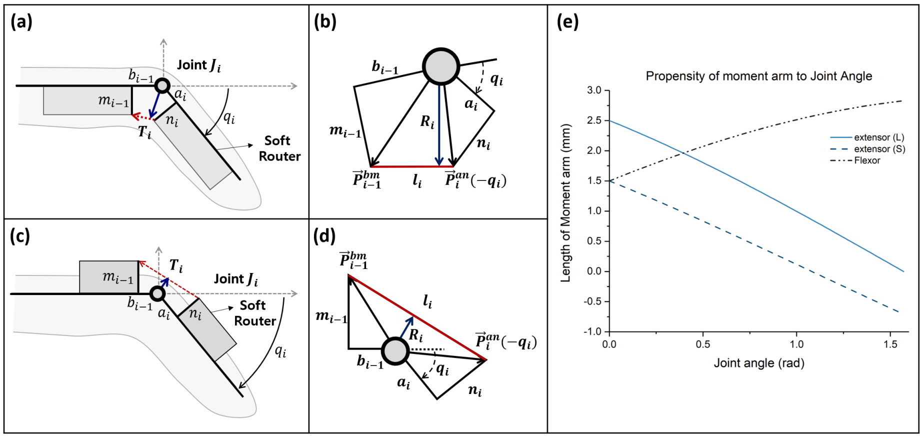


**Figure 5.2: Schematic view of the tendon routing method in the Exo-Glove II**

**(a)** and **(b)** show a schematic of the flexor router, while **(c)** and **(d)** show a schematic of the extensor router; (**e**) shows aspects of how the moment arm changes with respect to variation of the joint angle. Here, length of the flexor router and extensor (S) router ($a_i$, $b_{i-1}$, $m_{i-1}$, and $n_i$) each are 5, 5, 3, and 3mm, while $m_{i-1}$, and $n_i$ of the extensor (L) router is increased to 5mm.

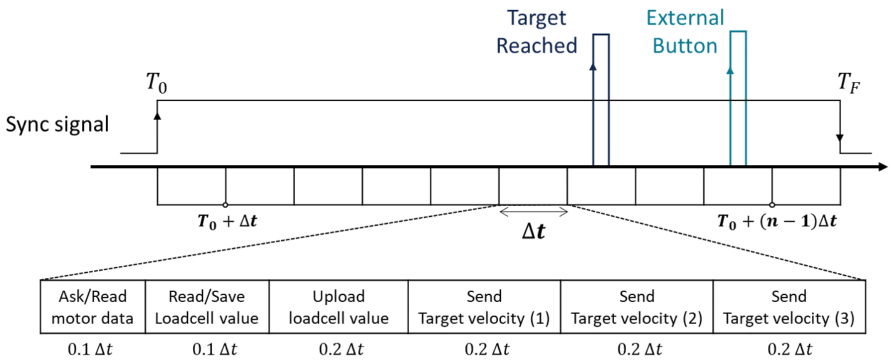


**Figure 5.3: Schematic of time scheduling in the controller for reliable data acquisition.**

In order to acquire the synchronized data reliably, the time schedule is divided into 10 steps as figure shows.

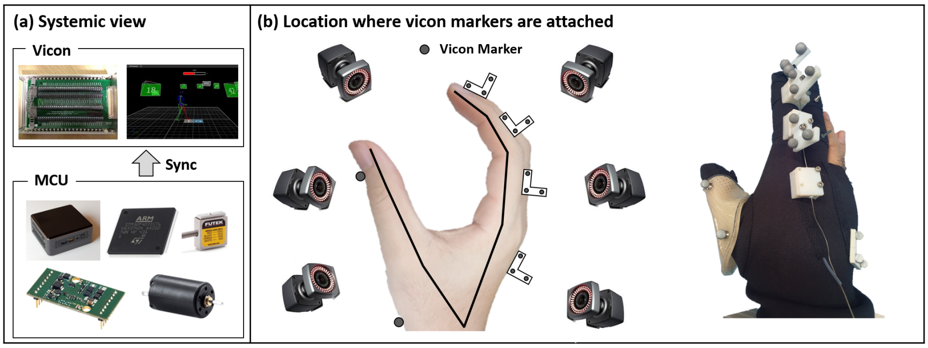


**Figure 5.4: Schematic view of the experimental protocol**

(**a**) a systemic view of Vicon and the control system; (**b**) the location where Vicon markers are attached.

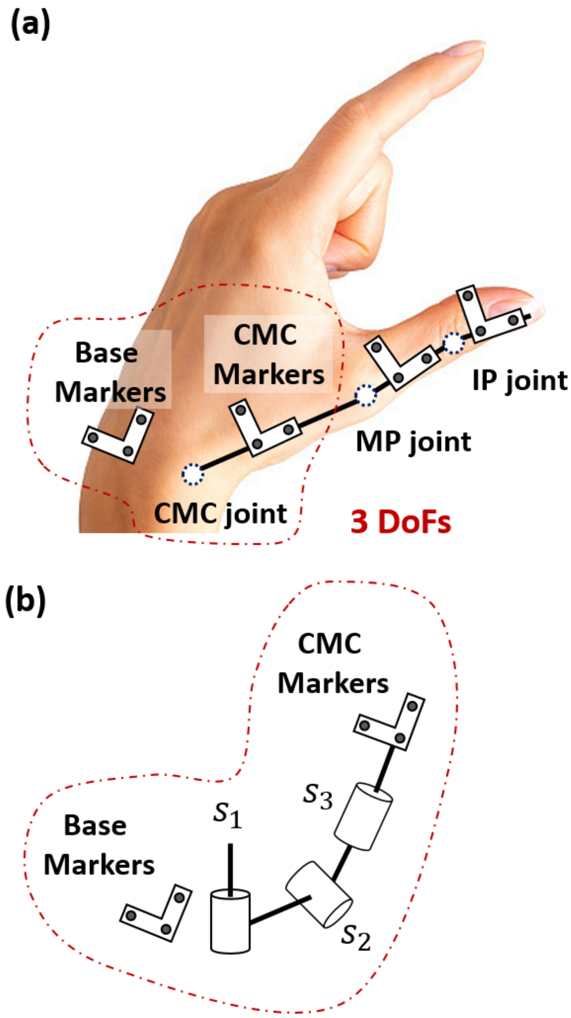


$$T_{base-CMC} = T_{b1}T_{12}T_{23}T_{3E}$$

$$= e^{s_1\theta_1}e^{s_2\theta_2}e^{s_3\theta_3}M$$

**Figure 5.5: Kinematic parameters of the thumb**

**(a)** shows the thumb joints and markers used to calibrate the thumb kinematic parameters and **(b)** shows the target calibration model for the thumb joints.

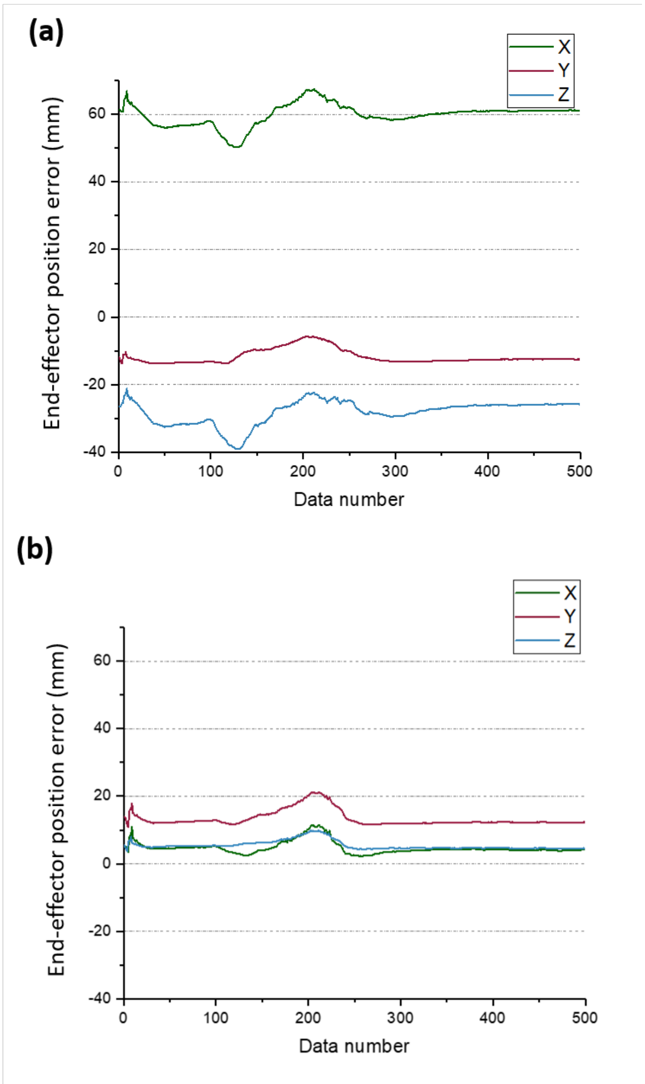


**Figure 5.6: Simulated results of the kinematic system identification**

**(a)** shows the error of the end-effector position before calibration while **(b)** shows the end-effector position error after calibration.

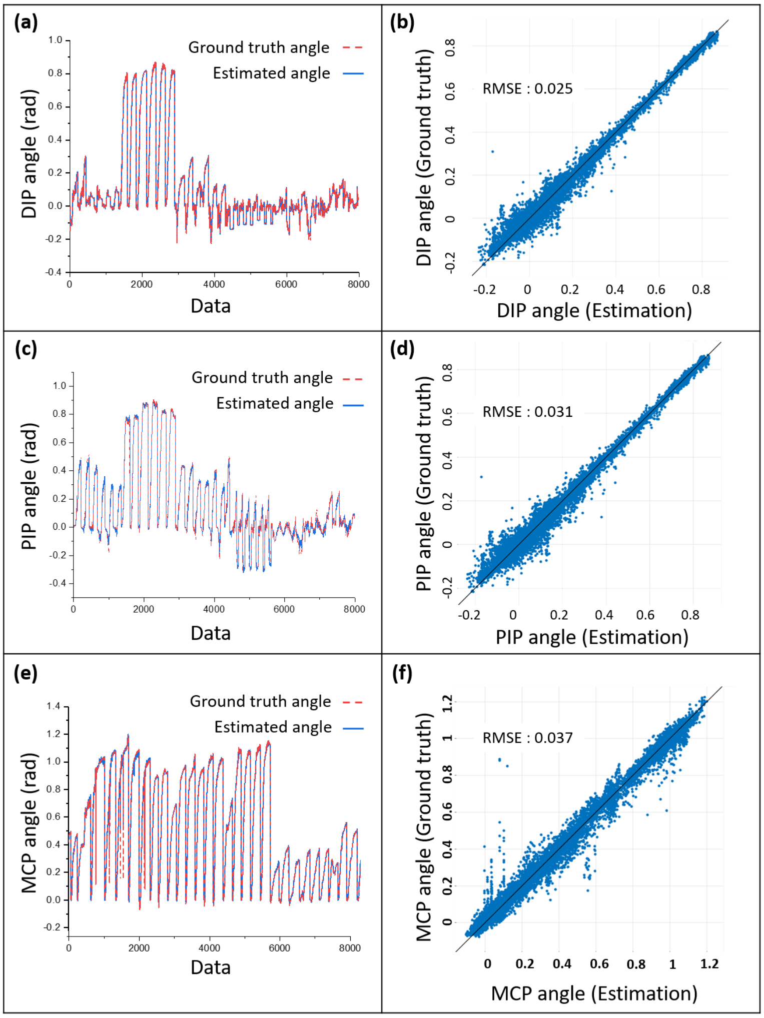


**Figure 5.7: Experimental results of the stiffness parameter estimation that shows relationship between joint angle and wire tension.**

**(a)**, **(c)**, and **(e)** show comparison of the ground truth angle with estimated angle using wire tension and wire stroke. The relationship between estimated angle and ground truth angle can be found in **(b)**, **(d)**, and **(f)**.

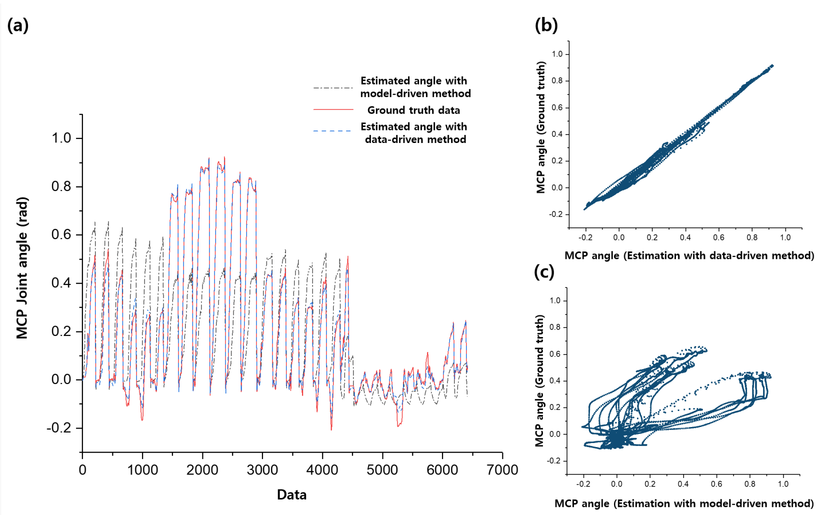


**Figure 5.8: Results of estimation that shows relationship between joint angle and wire tension.**

(**a**) shows comparison of the ground truth angle with the estimated angle from data-driven method and the estimated angle from model-driven method; (**b**) and (**c**) each show response plot of the data-driven method and model-driven method respectively.

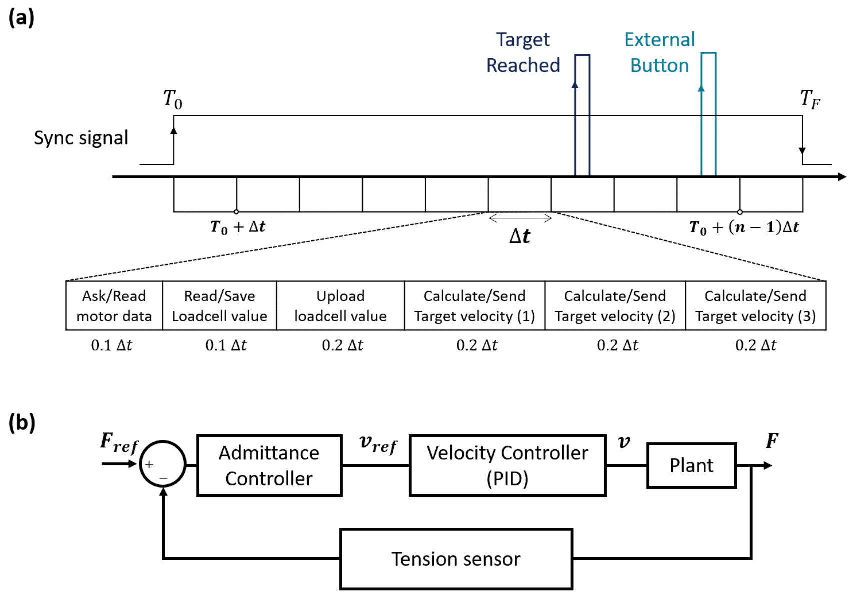


**Figure 5.9: Block diagram of the control scheme used in the proposed robot**

By adapting the concept of admittance control, the wire tension is controlled by controlling the corresponding velocity.


**Figure 5.10: Exo-Glove II with various grasps**

Exo-Glove II is designed to assist the thumb, index and middle finger and therefore, it was possible to make tripod grasp, lateral pinch, and wrap grasp with Exo-Glove II.

**Table 5.1:** Result of kinematic calibration

| RMS error before calibration | x direction | y direction | z direction |
|---|---|---|---|
| Value (mm) | 59.86 | 11.90 | 28.33 |
| RMS error after calibration | x direction | y direction | z direction |
| Value (mm) | 5.06 | 13.53 | 5.58 |

# Chapter 6

# Conclusion

The wearable robot researchers have been struggled with the trade-off issue between the simplicity and the functionality of the robot; When the number of actuators increases, it is possible to assist numerous joints but it also affects the robot system to be bulky and complex; When the number of actuator reduces, it is possible to assist only limited number of joints. The thesis aimed to solve this trade-off issue by a proper use of under-actuation mechanism. For more detail, the thesis propose a under-actuated tendon driven wearable robot for various postures; Exo-Glove II has been developed to assist various postures such as power grasp, lateral pinch, and tripod grasp with four tendon driven actuators.

Since the assisted postures require the thumb, index finger and middle finger motion, Exo-Glove II should assist nine joints with 14 DOFs. It means that at least 14 actuators are required to make hand motion, but it is quite unsubstantial solution in wearable robot. It is because - due to the robots should be worn on human body - the size, complexity, volume are significantly important factors. In order to satisfy the robot requirement, the proposed system is operated only with limited number of actuators by using the concept of the under-actuation mechanism; The proposed system covers nine joints with four tendon driven actuators by incorporating the under-actuation mechanism.

Even the under-actuation mechanism enables to reduce the robot complexity while sustaining the robot functions, there are an unsolved issue about scalability. In the under-actuation mechanism, when the constrained joints increase (i.e, when the number of joints that are assisted by a single actuator increases), the overall tendon routing becomes complicated or the friction at the wire increases as explained in the chapter 3.2.

The proposed research deals with the scalability issue by including a novel concept of actuator named Slider-Tendon Linear actuator, which contains the under-actuation mechanism; In this concept, by locating the under-actuation mechanism in the actuator rather than in the end-effector, the proposed actuator solve the scalability issue. As the results in the chapter 2 show, the proposed method of using Slider-Tendon Linear actuator not only improves the performance of the mechanism but also simplifies the end-effector.

In order to maximize the performance of the robot which uses the Slider-Tendon Linear actuator, we also proposed a framework to find out the optimal tendon routing with consideration of the proposed actuator. In the proposed method, total seven tendon routings were obtained for the two finger situation. As a result, with four performance factors, the optimal tendon routing was selected as shown in chapter 3.

The thesis also provides a novel design method of the wearable robot by providing a concept of hybrid wearable robot. By appropriately using the rigid material and the soft material, it was possible to improve the fabrication process without harming the robot performance or usability. With given robot design and the Slider-Tendon Linear actuator, lastly, the method of making posture with Exo-Glove II is introduced. Unlike other robots, it is difficult to derive the robot model in soft tendon driven wearable robot due to several uncertainties originated from the human properties, robot deformation, and wire elongation. Since it is difficult to configure the the wearable robot, the last chapter introduces data-driven method to find out the relationship between wire tension and the joint angle. Using the derived relationship, it was possible to make several grasp postures.

As a summary, the proposed research shows a method to design the wearable robot with consideration of both usability and functionality. In order to consider these two factors, the thesis shows a properly used under-actuation mechanism could be a key technology to improve both performance factors. In this thesis, we proposed a novel soft hand wearable robot that assists various grasps with a proper use of under-actuation mechanism. In this robot, in order to deal with the scalability issue, a novel concept of actuator named Slider-Tendon Linear actuator was also introduced. The proposed study also includes a framework to find out the optimal way to apply the under-actuation mechanism and a method to deal with the possible problems that can be generated in the under-actuation mechanism. Using the proposed researches in this thesis, we hope that these research also can be used for other robotic researches which aim to improve the robot performance as well as the simplicity.

# References

Agarwal, Priyanshu, Yun, Youngmok, Fox, Jonas, Madden, Kaci & Deshpande, Ashish D. 2017 Design, control, and testing of a thumb exoskeleton with series elastic actuation. *International Journal of Robotics Research* **36** (3), 355–375.

Alexander, Verl, Alin, Albu-schaffer, Oliver, Block & Annika, Raatz 2015 *Soft Robotics - Transferring Theory to Application*, , vol. 17. Springer.

Anne, Hollister, William L, Buford, Loyd M, Myers, David J, Giurintano & Andrew, Novick 1992 The axes of rotation of the thumb CMC joint. *Journal of orthopaedic Research* **10** (3), 454–460.

Arno H. A, Stienen, Hekman, Edsko E. G., van der Helm, Frans C. T. & van der Kooij, Herman 2009 Self-Aligning Exoskeleton Axes Through Decouling of Joint Rotation and Translation. *Ieee Transactions on Robotics* **25** (3), 628–633.

Asbeck, Alan T., Schmidt, Kai, Galiana, Ignacio, Wagner, Diana & Walsh, Conor J. 2015 Multi-joint soft exosuit for gait assistance. *Proceedings - IEEE International Conference on Robotics and Automation* **2015-June** (June), 6197–6204.

Bicchi, Antonio, Gabiccini, Marco & Santello, Marco 2011 Modelling natural and artificial hands with synergies. *Philosophical Transactions of the Royal Society B: Biological Sciences* **366** (1581), 3153–3161.

Birglen, Lionel & Gosselin, Clément M. 2006 Force analysis of connected differential mechanisms: Application to grasping. *International Journal of Robotics Research* **25** (10), 1033–1046.

Brown, Christopher Y. & Asada, H. Harry 2007 Inter-finger coordination and postural synergies in robot hands via mechanical implementation of principal components analysis. *IEEE International Conference on Intelligent Robots and Systems* pp. 2877–2882.

Bunnel, Sterling 1938 Opposition of the thumb. *The Journal of Bone and Joint Surgery* **20** (2), 269–284.

Cappello, Leonardo, Meyer, Jan T., Galloway, Kevin C., Peisner, Jeffrey D., Granberry, Rachael, Wagner, Diana A., Engelhardt, Sven, Paganoni, Sabrina & Walsh, Conor J. 2018 Assisting hand function after spinal cord injury with a fabric-based soft robotic glove. *Journal of NeuroEngineering and Rehabilitation* **15** (1), 1–10.

Catalano, M. G., Grioli, G., Farnioli, E., Serio, A., Piazza, C. & Bicchi, A. 2014 Adaptive synergies for the design and control of the Pisa/IIT SoftHand. *International Journal of Robotics Research* **33** (5), 768–782.

Cempini, Marco, Cortese, Mario & Vitiello, Nicola 2015*a* A powered finger-thumb wearable hand exoskeleton with self-aligning joint axes. *IEEE/ASME Transactions on Mechatronics* **20** (2), 705–716.

Cempini, Marco, Cortese, Mario & Vitiello, Nicola 2015*b* A powered finger-thumb wearable hand exoskeleton with self-aligning joint axes. *IEEE/ASME Transactions on Mechatronics* **20** (2), 705–716.

Chernyak, Vadim, Flynn, Timothy, O'Rourke, Jeffrey, Morgan, Jonathan, Zalutsky, Anton, Chernova, Sonia, Nestinger, Stephen S. & Padir, Taskin 2012 The design and realization of a high mobility biomimetic quadrupedal robot. *Proceedings of 2012 8th IEEE/ASME International Conference on Mechatronic and Embedded Systems and Applications, MESA 2012* pp. 93–98.

Chiri, Azzurra, Vitiello, Nicola, Giovacchini, Francesco, Roccella, Stefano, Vecchi, Fabrizio & Carrozza, Maria Chiara 2012 Mechatronic design and characterization of the index finger module of a hand exoskeleton for post-stroke rehabilitation. *IEEE/ASME Transactions on Mechatronics* **17** (5), 884–894.

Chu, Chia Ye & Patterson, Rita M. 2018 Soft robotic devices for hand rehabilitation and assistance: A narrative review. *Journal of NeuroEngineering and Rehabilitation* **15** (1), 1–14.

De Santis, Agostino, Siciliano, Bruno, De Luca, Alessandro & Bicchi, Antonio 2008 An atlas of physical human-robot interaction. *Mechanism and Machine Theory* **43** (3), 253–270.

Ding, Ye, Galiana, Ignacio, Asbeck, Alan, Quinlivan, Brendan, De Rossi, Stefano Marco Maria & Walsh, Conor 2014 Multi-joint actuation platform for lower extremity soft exosuits. *Proceedings - IEEE International Conference on Robotics and Automation* pp. 1327–1334.

Dollar, Aaron M. & Howe, Robert D. 2010 The highly adaptive SDM hand: Design and performance evaluation. *International Journal of Robotics Research* **29** (5), 585–597.

Feix, Thomas, Romero, Javier, Schmiedmayer, Heinz-Bodo, Dollar, Aaron M & Kragic, Danica 2016 The GRASP Taxonomy of Human Grasp Types. *IEEE Transactions on Human-Machine Systems* **46** (1), 66–77.

Fontana, M., Dettori, A., Salsedo, F. & Bergamasco, M. 2009 Mechanical design of a novel hand exoskeleton for accurate force displaying. *Proceedings - IEEE International Conference on Robotics and Automation* pp. 1704–1709.

Grebenstein, Markus, Chalon, Maxime, Friedl, Werner, Haddadin, Sami, Wimböck, Thomas, Hirzinger, Gerd & Siegwart, Roland 2012 The hand of the DLR Hand Arm System: Designed for interaction. *The International Journal of Robotics Research* **31** (13), 1531–1555.

Guo, Jiaqi, Yu, Shuangyue, Li, Yanjun, Huang, Tzu Hao, Wang, Junlin, Lynn, Brian, Fidock, Jeremy, Shen, Chien Lung, Edwards, Dylan & Su, Hao 2018 A soft robotic exo-sheath using fabric EMG sensing for hand rehabilitation and assistance. *2018 IEEE International Conference on Soft Robotics, RoboSoft 2018* pp. 497–503.

Hasegawa, Yasuhisa, Mikami, Yasuyuki, Watanabe, Kosuke, Firouzimehr, Zeinab & Sankai, Yoshiyuki 2008 Wearable handling support system for paralyzed patient. *2008 IEEE/RSJ International Conference on Intelligent Robots and Systems, IROS* pp. 741–746.

Hirose, Shigeo 1985 Connected differential mechanism and its application. *Internation conference on advanced robotics* pp. 319–326.

Horigome, Atsushi & Endo, Gen 2016 Basic study for drive mechanism with synthetic fiber rope-investigation of strength reduction by bending and terminal fixation method. *Advanced Robotics* **30** (3), 206–217.

Horigome, Atsushi, Endo, Gen, Takata, Atsushi & Wakabayashi, Youki 2018*a* Development of New Terminal Fixation Method for Synthetic Fiber Rope. *IEEE Robotics and Automation Letters* pp. 1–1.

Horigome, Atsushi, Endo, Gen, Takata, Atsushi & Wakabayashi, Youki 2018*b* Development of New Terminal Fixation Method for Synthetic Fiber Rope. *IEEE Robotics and Automation Letters* pp. 1–1.

Iannucci, Lorenzo, Del Rosso, Stefano, Curtis, Paul T., Pope, Dan J. & Duke, Phillip W. 2018 Understanding the thickness effect on the tensile strength property of Dyneema®HB26 laminates. *Materials* **11** (8).

In, Hyunki, Jeong, Useok, Lee, Haemin & Cho, Kyu Jin 2017 A Novel Slack-Enabling Tendon Drive That Improves Efficiency, Size, and Safety in Soft Wearable Robots. *IEEE/ASME Transactions on Mechatronics* **22** (1), 59–70.

In, Hyunki, Kang, Brian Byunghyun, Sin, Minki & Cho, Kyu-jin 2015 Exo-Glove: A Wearable Robot for the Hand With a Soft. *IEEE Robotics and Automation Magazine* pp. 97–105.

Jingdong, Zhao, Li, Jiang, Shicai, Shi, Hegao, Cai, Hong, Liu & Gerd, Hirzinger 2006 A five-fingered underactuated prosthetic hand system. *2006 IEEE International Conference on Mechatronics and Automation, ICMA 2006* **2006** (50435040), 1453–1458.

Kaneko, Makoto, Wada, Mitsuo, Maekawa, Hitoshi & Tanie, Kazuo April, 1991 A new consideration on tendon-tension control system of robot hands. *Proceedings. 1991 IEEE International Conference on Robotics and Automation* pp. 1028–1033.

Kang, Brian Byunghyun, Choi, Hyungmin, Lee, Haemin & Cho, Kyu-Jin 2019 Exo-Glove Poly II: A Polymer-Based Soft Wearable Robot for the Hand with a Tendon-Driven Actuation System. *Soft Robotics* **6** (2), 214–227.

Kang, Brian Byunghyun, In, Hyunki & Cho, Kyujin 2012 Force transmission in joint-less tendon driven wearable robotic hand. *International Conference on Control, Automation and Systems* pp. 1853–1858.

Kang, Brian Byunghyun, Lee, Haemin, In, Hyunki, Jeong, Useok, Chung, Jinwon & Cho, Kyu Jin 2016 Development of a polymer-based tendon-driven wearable robotic hand. *Proceedings - IEEE International Conference on Robotics and Automation* **2016-June**, 3750–3755.

Kim, Byungchul, In, Hyunki, Lee, Daeyoung & Cho, Kyujin 2017 Development and assessment of a hand assist device : GRIPIT. *Journal of Neuroengineering and Rehabilitation* pp. 1–22.

Kim, Byungchul & Ryu, Jiwon 2020 Joint Angle Estimation of a Tendon-driven Soft Wearable Robot through a Tension and Stroke Measurement. *Sensors (Switzerland)* pp. 1–20.

Kim, Dong Hyun & Park, Hyung Soon 2018 Cable Actuated Dexterous (CADEX) Glove for Effective Rehabilitation of the Hand for Patients with Neurological diseases. *IEEE International Conference on Intelligent Robots and Systems* pp. 2305–2310.

Kim, Minji, Park, Junyoung, Kim, Juhyeok, Kim, Myungsin & Lee, Dongjun 2018 Stiffness Decomposition and Design Optimization of

Under-Actuated Tendon-Driven Robotic Systems. *Proceedings - IEEE International Conference on Robotics and Automation* pp. 2266–2272.

Lalibert, Thierry 2008 An Anthropomorphic Underactuated Robotic Hand with 15 Dofs and a Single Actuator. *IEEE International Conference on Robotics and Automation* pp. 749–754.

Lee, Sang Wook, Landers, Katlin A. & Park, Hyung Soon 2014 Development of a biomimetic hand exotendon device (BiomHED) for restoration of functional hand movement post-stroke. *IEEE Transactions on Neural Systems and Rehabilitation Engineering* **22** (4), 886–898.

Li, Jia, Zhao, Fei, Li, Xingchen & Li, Junjie 2016 Analysis of robotic workspace based on Monte Carlo method and the posture matrix. *Proceedings of 2016 IEEE International Conference on Control and Robotics Engineering, ICCRE 2016* pp. 1–5.

Li, Zong Ming & Tang, Jie 2007 Coordination of thumb joints during opposition. *Journal of Biomechanics* **40** (3), 502–510.

Lynch, Kevin M. & Park, Frank C. 2016 *Introduction To Modern Robotics Mechanics, Planning, and Control*. Cambridge University Press, arXiv: 0712.0689.

Mackenzie, Christine 1994 *The Grasping Hand*, , vol. 53. North-Holland, arXiv: arXiv:1011.1669v3.

Madson, Michael 2013 Cable connector.

Mao, Ying & Agrawal, Sunil Kumar 2012 Design of a Cable-Driven Arm Exoskeleton (CAREX) for Neural Rehabilitation: Robotics, IEEE Transactions on. *Robotics, IEEE Transactions on* **PP** (99), 1–10.

Marzke, M.W. 1992 Evolutionary development of the human thumb. *Hand Clinics* **8** (1), 1–8.

Nanayakkara, Visakha K., Cotugno, Giuseppe, Vitzilaios, Nikolaos, Venetsanos, Demetrios, Nanayakkara, Thrishantha & Sahinkaya, M. Necip 2017 The Role of Morphology of the Thumb in Anthropomorphic Grasping: A Review. *Frontiers in Mechanical Engineering* **3** (June).

Nilsson, Mats, Ingvast, Johan, Wikander, Jan & Von Holst, Hans December, 2012 The Soft Extra Muscle system for improving the grasping capability in neurological rehabilitation. *2012 IEEE-EMBS Conference on Biomedical Engineering and Sciences, IECBES 2012* pp. 412–417.

Ogane, D., Hyodo, K. & Kobayashi, H. 1996 Mechanism and control of a 7 DOF tendon-driven robotic arm with NST. *J. Robot. Soc. Jpn.* **14** (8), 1152–1159.

Okamura, Koichiro & Park, Frank Chongwoo 1996 kinematic calibration using the product of exponentials formula.

Ozawa, Ryuta, Kobayashi, Hiroaki & Hashirii, Kazunori 2014 Analysis, classification, and design of tendon-driven mechanisms. *IEEE Transactions on Robotics* **30** (2), 396–410.

Palli, G. & Melchiorri, C. 2006 Model and control of tendon-sheath transmission systems. *Proceedings - IEEE International Conference on Robotics and Automation* **2006** (May), 988–993, arXiv: arXiv:1011.1669v3.

Panizzolo, Fausto A., Galiana, Ignacio, Asbeck, Alan T., Siviy, Christopher, Schmidt, Kai, Holt, Kenneth G. & Walsh, Conor J. 2016 A biologically-inspired multi-joint soft exosuit that can reduce the energy cost of loaded walking. *Journal of NeuroEngineering and Rehabilitation* **13** (1).

Park, Daegeun & Cho, Kyu Jin 2017 Development and evaluation of a soft wearable weight support device for reducing muscle fatigue on shoulder. *PLoS ONE* **12** (3), 1–24.

Shahid, Talha, Gouwanda, Darwin, Nurzaman, Surya G., Gopalai, Alpha A., Shahid, Talha, Gouwanda, Darwin, Nurzaman, Surya G. & Gopalai, Alpha A. 2018 Moving toward Soft Robotics: A Decade Review of the Design of Hand Exoskeletons. *Biomimetics* **3** (3), 17.

SOUCACOS, P. N. 2001 Indications and selection for digital amputation and replantation. *Journal of Hand Surgery* **26 B** (6), 572–581.

SPORER, N, HDMLE, M, KRENN, R, PASCUCCI, A & SCHEDL, M 2002 DLR's torque-controlled light weight robot. In *Mechatronics*, pp. 1710–1716.

THK 2017 Ball ScrewTHKGeneral Catalog. *Tech. Rep.*.

THOMSON INDUSTRIES INC. 2013 Lead Screws , Ball Screws and Ball Splines Catalogue .

T.TOWNSEND, WILLIAM 1988 The Effect of Transmission Design on Force Controlled manipulator performance. *Ph.D. dissertation, Dept. Mech. Eng.* .

VEALE, ALLAN JOSHUA & XIE, SHANE QUAN 2016 Towards compliant and wearable robotic orthoses: A review of current and emerging actuator technologies. *Medical Engineering and Physics* **38** (4), 317–325.

WEGE, ANDREAS, KONDAK, KONSTANTIN & HOMMEL, GÜNTER 2006 Development and control of a hand exoskeleton for rehabilitation. *Human Interaction with Machines Proceedings of the 6th International Workshop held at the Shanghai JiaoTong University, 2005* pp. 149–157.

WENSING, PATRICK M., WANG, ALBERT, SEOK, SANGOK, OTTEN, DAVID, LANG, JEFFREY & KIM, SANGBAE 2017 Proprioceptive actuator design in the MIT cheetah: Impact mitigation and high-bandwidth physical interaction for dynamic legged robots. *IEEE Transactions on Robotics* **33** (3), 509–522.

WESTON B, GRIFFIN, RYAN P, FINDLEY, MICHAEL L, TURNER & MARK R, CUTKOSKY 2000 Calibration and Mapping of a Human Hand for Dexterous Telemanipulation. In *Haptic Interfaces for Virtual Environments and Teleoperator Systems Symposium*, pp. 1 – 8.

WHITNEY, D.E. 1977 Force Feedback Control of Manipulator Fine Motions. *Transactions of the ASME Journal of Dynamical Systems Measurement Control* **99** (2), 91–97.

WORSNOPP, T. T., PESHKIN, M. A., COLGATE, J. E. & KAMPER, D. G. 2007

An actuated finger exoskeleton for hand rehabilitation following stroke. *2007 IEEE 10th International Conference on Rehabilitation Robotics, ICORR'07* **00** (c), 896–901.

Xiloyannis, Michele, Cappello, Leonardo, Binh, Khanh D, Antuvan, Chris W & Masia, Lorenzo 2017 Preliminary design and control of a soft exosuit for assisting elbow movements and hand grasping in activities of daily living. *Journal of Rehabilitation and Assistive Technologies Engineering* **4**, 205566831668031.

Xiloyannis, Michele, Cappello, Leonardo, Khanh, Dinh Binh, Yen, Shih Cheng & Masia, Lorenzo 2016 Modelling and design of a synergy-based actuator for a tendon-driven soft robotic glove. *Proceedings of the IEEE RAS and EMBS International Conference on Biomedical Robotics and Biomechatronics* **2016-July**, 1213–1219.

Xu, Patricia A., Levine, David J., Yang, Ho-Jung, Shepherd, Robert F., O'Brien, Kevin W., Xiao, Michael F., Aubin, Cameron A. & Wiesner, Lennard W. 2018 Elastomeric passive transmission for autonomous force-velocity adaptation applied to 3D-printed prosthetics. *Science Robotics* **3** (23), eaau5543.

# Appendix A

# Literature review of the hand wearable robots and hand anatomy

## A.1. Literature review of the hand wearable robots

Wearable robots developed nowadays can be classified according to 1) the material used in the robot, 2) the parts to be worn, and 3) the purpose of the robot. When the robots are categorized according to the purpose of robot, robots can be separated into the robots for rehabilitation and the robots for assistance. Also, the wearable robots can be divided into the robots for upper limb, lower limb, and core muscle. Lastly, the robots can be classified by the materials used in the robot. (e.g, rigid wearable robot and soft wearable robot)

In fact, the terms *rigid* and *soft* used in the wearable robots are confusing while the other classifications are quite straightforward. This is because these terms can not only mean a robot's body is hard or soft, but it can also mean that the transmission is hard or soft. When these terms are used to describe the compliance of the robot body, the rigid wearable robots can be defined robots using metal frames as shown in (Worsnopp *et al.* 2007; Hasegawa *et al.* 2008; Chiri *et al.* 2012), while soft wearable robots are thought as the robot with compliant materials such as garment (In *et al.* 2015) and silicone (Kang *et al.* 2019).

The wearable robots with rigid frame show advantage when high assistance force is required; It applies less compression force on the joints because the frame can endure the force instead. Also, these robots can assist to make more accurate posture because the robot kinematics can be easily solved. However, when the rigid frame is used, the size and weight problem occurs due to the joint alignment issue (Cempini *et al.* 2015*a*; Chiri *et al.* 2012). The alternative method is to use soft material because the joint alignment issue can be easily solved by its inherent characteristics.

When the compliance of transmission is used for the classification, gear or linkage driven methods are described as rigid transmissions (Fontana *et al.* 2009; Wege *et al.* 2006) while tendon (In *et al.* 2015; Kang *et al.* 2019) or pneumatic driven methods (Cappello *et al.* 2018) are considered as soft transmissions. Similar to the rigid frame and soft frame cases, the compliance of transmission also affects the simplicity and accuracy of the robots; When the compliant actuation is used, it is possible to make safe and compact robot but the deformation of the transmission makes difficult to figure out the Jacobian of the robot; Here, Jacobian is used to explain the relationship between joint angle and actuator stroke. However, when the transmission becomes stiff, the robot accuracy increases and fast response can be possible. Although the stiff transmission has certain advantages, it is hesitated to be used in some application because of the bulky size and relatively dangerous performance.

Actually, when we consider about the target body parts of the wearable robot, most of human body parts to be the target. Among various body parts, hand is one of frequently assisted body part. It is because hand roles quite important role in daily living. Although the wearable robot for the hand assistance has received great attention for lots of researchers, the hand wearable robot yet exists only in the lab. One of the main reason is that the hand has a complicated structure; Details about the hand structure are more explained in the appendix A.2. Here, we are going to concentrate on the review of the thumb wearable robot because the proposed robot in this thesis is thumb wearable robot as well.

Since the thumb has quite complicated structure, the thumb assist wearable robots have not developed a lot. In case of rigid wearable robot, Agarwal *et al.* (2017) has developed a tendon driven wearable robot that uses series elastic actuation method to assist the thumb. Thanks to the series elastic actuator, the robot shows sufficient torque control performance. However, since the robot has quite bulky size, it could cause difficulty to use in assistance purposes. As a simplified design, several tendon driven robots are designed to assist the thumb with four actuators (Kim & Park 2018; Lee *et al.* 2014). This design is based on the fact that the opposition of the thumb, one of the most important motion in human hand, requires two functional degree of freedoms (fDOFs) (Li & Tang 2007). As the previous researches show, the usage of four actuators can make sufficient grasp posture by assisting the opposition of the thumb (Kim & Park 2018; Lee *et al.* 2014). Note that, this information gives us that it is not important to assist whole degree of freedoms. Although these robots have relatively simple design, using four actuators for the thumb is yet excessive. Therefore, we tried to develop more simple wearable robot using the under-actuation mechanism. Details are described in the main text.

For the last classification, the wearable robot could be classified using the purpose of the robot. In this classification, most of wearable robots are developed for two purposes: assistance and rehabilitation. This classification could be understood more easily by looking at the exact cases. For instance, In et al. developed a tendon driven soft robotic glove, named as SNU Exo-Glove, for spinal cord injured people (In *et al.* 2015). This glove assists thumb, index and middle finger with three actuators. For adaptability, under-actuation mechanism is applied in this robot. Exo-Glove Poly was developed by the same research team and they changed the material of robot body from garment to polymer. In addition, this research team maximized the simplicity of the robot by assisting thumb passively. Other researchers developed Graspy Glove for high portability, by attaching all actuators and electrical circuits on the back side of the hand. As rehabilitation purposes, BiomHED was developed by mimicking muscle and tendon system of the human hand. This robot uses 7 motors and tries to make natural posture of human hand by attaching the wire similar to the tendon of human hand. A commercially developed glove, named as Gloreha, also exists and this robot provides rehabilitation with virtual reality environment. As such, hand assisted robots have been developed with different strategy for a variety of purposes. (e.g, high grasping performance, creating natural hand posture, high portability, or ability to rehabilitate physical functions and etc.)

## A.2. Human hand anatomy

Since the wearable robots interact with the human body in the human environment, it is important to understand the human body. The importance is even more pronounced when it comes to the soft wearable robots because these robots make the motion with respect to the human body rather than the robot body as mentioned in the introduction chapter. Since the proposed robot in this thesis is hand wearable robot (i.e, More specifically, wearable robot for the thumb, index finger, and middle finger), this section mainly describes the hand anatomy.

Human hand consists of five fingers and it performs various tasks by grasping or manipulating numerous objects. When the finger moves, the joint motion can be defined in terms of flexion/extension, abduction/adduction, and surpination/pronation; Since human joints are rotational joint rather than prismatic joint, the human joints can be explained in three directional rotations.

The direction of the above three motions can be described as follow. In the direction of grasping, the motion is usually expressed as flexion, while a motion in the opposite direction is called extension. In addition, if a tendon is used in flexion, it can be roughly called a flexor, while an extensor is used to designate a tendon that is used in extension. Spreading between fingers is called abduction, while the opposite is called adduction. The last motion is called internal rotation; in this motion, the finger itself rotates.

Nomenclature of the joints and phalanges of the hand is described as shown in Figure A.1. In the case of the index finger, the distal interphalangeal joint (DIP joint) and the proximal interphalangeal joint (PIP joint) have one degree of freedom (flexion/extension motion), while the metacarpo interphalangeal joint (MCP joint) has two degrees of freedom (flexion/extension and abduction/adduction motion). Also, the word distal is used to describe the direction away from the body, while the word proximal is used to express the opposite direction, which is the direction towards the body. To express the palm side of the hand, the word 'palmar' is used, while the other side of the hand is called the dorsal side.

In the grasping, the thumb plays the most important role by being located in the opposite direction of the other fingers; this posture is named as a thumb opposition and is generated by the unique joint characteristics of the thumb (Marzke 1992; Bunnel 1938). Soucacos (2001) insists that the thumb provides more than 40% of the hand function and therefore, it is given the first priority for replantation.

The thumb consists of three bones and for convenience, each bone will be named as metacarpal, proximal phalange, and distal phalange. Then, the thumb joints could be defined as Carpometacarpal (CMC) joint, Metacarpal (MP) joint, and Interphalange (IP) joint. The degree of freedoms of the thumb joints are not well defined. For instance, the CMC joint could be described as two DoFs or three DoFs because the human joint are not exactly revolute joint; The existence of the Flexion/extension and abduction/adduction motion is quite certain but in the case of the internal rotation motion (i.e, pronation and supination), researchers have different opinions (Nanayakkara *et al.* 2017). Especially, some researchers insist that the internal rotation is coupled with flexion/extension motion (Li & Tang 2007) and the others explain that this internal motion does not occur (Anne *et al.* 1992).

In the thumb motion, one of the most important motion is named as an *opposition* motion. This motion means the thumb is located in the opposite direction of the other fingers. The importance of the opposition is quite obvious because the grasp motion should apply force closure or form closure to the object. In this opposition motion, flexion and abduction/adduction motion of the CMC joint plays important role (Li & Tang

2007).

In the grasping motion of the human hand, a concept of *virtual finger* is well used (Mackenzie 1994). This concept is quite vague but it gives better understand about the grasp. In this concept of virtual finger, the grasp is occurred with two virtual fingers. These two VFs are located in the opposite direction to the each other, and applies opposite directional force to the grasped object. According to the virtual fingers in the opposite direction, there are three kinds of opposition modes: Pad opposition, palm opposition, and side opposition. Recently, the grasp taxonomy is developed in terms of these opposition mode and we can find that the thumb motion is important in grasping (Feix *et al.* 2016).

According to these previous studies about the wearable robot and the human hand anatomy, the thumb wearable robot named Exo-Glove II has been developed in this thesis. Exo-Glove II are developed to assist the thumb, index finger and middle finger using four tendon driven actuators. By using the under-actuation mechanism, it was possible to reduce the number of actuators. Details are described in the main text.

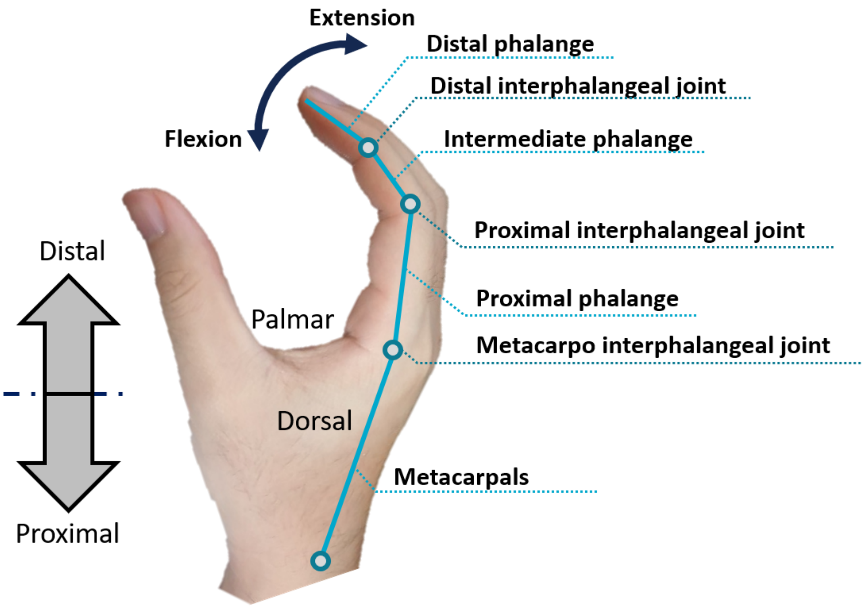


**Figure A.1:** Brief explanation of how the parts of the hand are represented.

# Appendix B

# Method to calculate the tension distribution in dual tendon routing

## B.1. Friction modelling of tendon

Appendix A explains a method to calculate the tension distribution of a system with dual tendon routing. Here, tension distribution of 7 tendon routings (TR1 - TR7 in the Figure B.1) were calculated. Modelling is done with several assumptions and was experimentally verified. Friction applied on the wire can be derived using a capstan equation(Kaneko *et al.* April, 1991). In the capstan equation, friction of the wire is assumed as being applied on the wire when the wire path is curved; Since the mass of wire is negligible, normal force applied on the wire is only affected by tension of the wire and curvature of wire path. The relation between input tension ($T_{in}$ in Figure B.2 (a)) and output tension($T_{out}$ in Figure B.2 (a)) can be described as shown in Eq (B.1).

$$T_{out} = T_{in} e^{-\mu N} \tag{B.1}$$

The relationship between input tension and the output tension varies

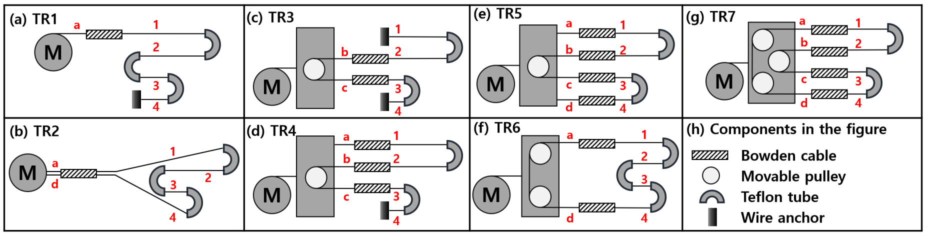


**Figure B.1: Possible tendon routings for dual tendon routing**
In Exo-Glove, seven tendon routings are possible and method to derive these tendon routing is explained in chapter 3.3.2.

whether the wire moves along a non-rotating object such as a Teflon tube or it moves along a rotating object, such as a bearing. When the wire passes fixed curvature such as Teflon tube, the friction of the wire can be simply defined as Eq (B.2) and Eq (B.3). On the other hand, in the case of rotating curvature, the friction between the wire and bearing cover ($f$ in the Figure B.2 (b)) and the friction inside the bearing ($g$ in the Figure B.2 (b)) should be considered. Since the mass of bearing is negligible, we can assume the $f$ and $g$ should be equal because of force equilibrium. Although we cannot exactly know the $f_{rotary}$ in Eq (B.4), we can estimate the friction by using $g_{rotary}$ in Eq (B.5). Finally, the relationship between input tension and output tension in the rotary case can be described as Eq (B.6).

$$f_{static} \leqslant T_{in}e(-\mu_s\theta) \tag{B.2}$$

$$f_{static} = T_{in}e(-\mu_k\theta) \tag{B.3}$$

$$f_{roatary} = T_{out} - T_{in} \leqslant T_{in}e^{-\mu_s\theta} \tag{B.4}$$

$$g_{rotary} = T_{in}(1 - e^{-\mu_r N}) \tag{B.5}$$

$$f_{rotary} = g_{rotary} = T_{in}(1 - e^{-\mu_r N}) \tag{B.6}$$

In this appendix, wire elongation is considered to avoid the fact that static friction is difficult to infer the exact value and only thing we can know is that it is just less than the maximum static friction. If the wire elongation causes movement of the wire, we assumed the friction as a dynamic friction. Dynamic friction coefficient of the Teflon tube and the bearing used in the modelling is 0.18 and 0.001 (In *et al.* 2015). Since the process of deriving the tension of each segments begins with finding the direction in which the wire moves, details for deriving tension distribution are explained in the following sections by considering the kinematic conditions of the wire. With the derived tension distribution, several indicators, things to evaluate whether it is useful to apply to real application, are proposed.

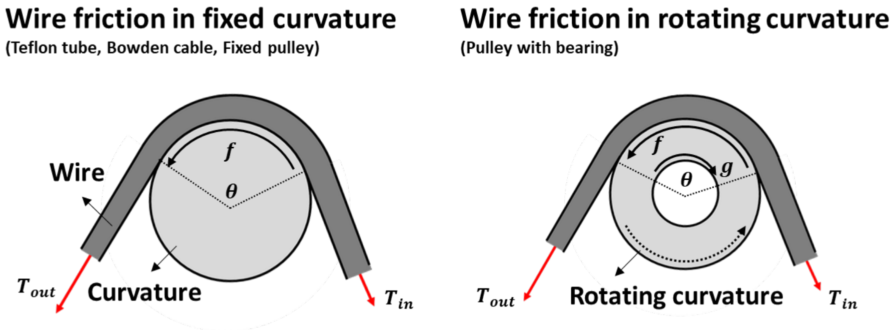


**Figure B.2: Schematic to derive wire friction in curvature**

Since the friction depends on the relative distance between objects, the friction is defined whether wire is moving along the fixed curvature or rotating curvature.

## B.2. Tension distribution of the tendon routing 1

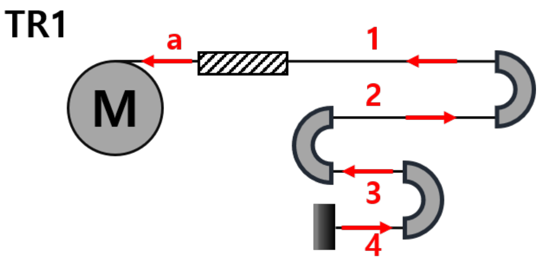


**Figure B.3: Schematic of tendon routing 1**

Tendon routing 1 (TR1) schematic to derive the tension distribution.

In TR1, one side of the wire is fixed at the end-effector while the other side of wire is fixed at the motor. In this case, tension distribution can be easily obtained because the pulling direction of the wire is straightforward. Here, when the motor pulls the wire, the wire passes from the section 4 to section 1 and finally it moves to the section $a$. Therefore, the force equations about tension can be described as follows.

$$T_M = T_a \tag{B.7}$$

$$T_3 - T_4 = T_3(1 - e^{-\mu_t \pi}) \tag{B.8}$$

$$T_2 - T_3 = T_2(1 - e^{-\mu_t \pi}) \tag{B.9}$$

$$T_1 - T_2 = T_1(1 - e^{-\mu_t \pi}) \tag{B.10}$$

$$T_a - T_1 = T_a(1 - e^{-\mu_s \theta_s}) \tag{B.11}$$

| TR1 | $T_M$ | $T_1$ | $T_2$ | $T_3$ | $T_4$ |
|---|---|---|---|---|---|
| | 1 | 0.32 | 0.18 | 0.10 | 0.06 |
| Ratio | - | 48(%) | 27(%) | 16(%) | 9(%) |

**Table B.1:** Tension distribution of the tendon routing 1

Using the Eq (B.7) - Eq (B.11), final tension distribution can be obtained as Eq (B.12) - Eq (B.15).

$$T_1 = T_M e^{-\mu_s \theta_s} \tag{B.12}$$

$$T_2 = T_M e^{-\mu_s \theta_s - \mu_t \pi} \tag{B.13}$$

$$T_3 = T_M e^{-\mu_s \theta_s - 2\mu_t \pi} \tag{B.14}$$

$$T_4 = T_M e^{-\mu_s \theta_s - 3\mu_t \pi} \tag{B.15}$$

We can see that the tension of the wire gradually decreases as the wire goes from section 1 to section 4. When the exact value about friction coefficient is used in the above equations, the tension distribution of TR1 can be summarized as Table.B.1. Overall comparison with other tendon routings (TR1 - TR7) are explained at the end of appendix.

## B.3. Tension distribution of the tendon routing 2

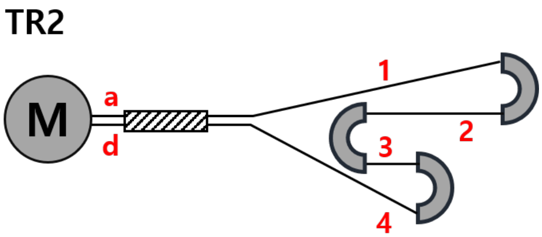


**Figure B.4: Schematic of tendon routing 2**

Tendon routing 2 (TR2) schematic to derive the tension distribution.

In TR2, both side of the wire is fixed at the motor. In this case, tension distribution is more uniform than TR1 because each side of the wire (section 1 and 4) is pulled by the wire at the section a and d respectively. Here, the tension relationship between each sections can be described as Eq (B.16) - Eq (B.22). Here, the wire between section 3 and 4 does not move theoretically. Therefore, exact friction between section 3 and 4 can not be defined and the only information about the friction is that the friction is less than the maximum static frictional force as shown in Eq (B.21). However, when the wire elongates when the tension increases, the friction between section 3 and 4 can be defined as kinetic friction. Therefore, the relationship between $T_3$ and $T_4$ can be defined as Eq (B.22).

$$T_M = T_a + T_d \tag{B.16}$$

$$T_a - T_1 = T_a(1 - e^{-\mu_s \theta_s}) \tag{B.17}$$

$$T_d - T_4 = T_d(1 - e^{-\mu_s \theta_s}) \tag{B.18}$$

$$T_1 - T_2 = T_1(1 - e^{-\mu_t \pi}) \tag{B.19}$$

$$T_2 - T_3 = T_2(1 - e^{-\mu_t \pi}) \tag{B.20}$$

$$T_4 - T_3 < T_4(1 - e^{-\mu_{t.s} \pi}) \tag{B.21}$$

$$T_4 - T_3 = T_4(1 - e^{-\mu_t \pi}) \tag{B.22}$$

With the Eq (B.15) - Eq (B.22), final tension distribution can be obtained as Eq (B.23) - Eq (B.27).

$$T_1 = G_\mu T_M e^{-\mu_s \theta_s} \tag{B.23}$$

$$T_2 = G_\mu T_M e^{-\mu_s \theta_s - \mu_t \pi} \tag{B.24}$$

$$T_3 = G_\mu T_M e^{-\mu_s \theta_s - 2\mu_t \pi} \tag{B.25}$$

$$T_4 = G_\mu T_M e^{-\mu_s \theta_s - \mu_t \pi} \tag{B.26}$$

$$G_\mu = (1 + e^{-\mu_t \pi})^{-1} \tag{B.27}$$

Here, the tension of the wire decreases from section 1 to section 3 but the tension of the wire at the section 4 shows bigger than that of the wire at the section 3 because the wire of the section 4 is directly pulled by the motor by being pulled by the wire at the section a. When the exact

| TR1 | $T_M$ | $T_1$ | $T_2$ | $T_3$ | $T_4$ |
|---|---|---|---|---|---|
| | 1 | 0.21 | 0.12 | 0.07 | 0.12 |
| Ratio | - | 41(%) | 23(%) | 13(%) | 23(%) |

**Table B.2:** Tension distribution of the tendon routing 2

value about friction coefficient is used in the above equations, the tension distribution of TR2 can be summarized as Table.B.2.

## B.4. Tension distribution of the tendon routing 3

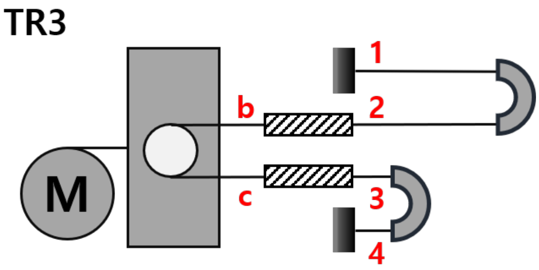


**Figure B.5: Schematic of tendon routing 3**

Tendon routing 3 (TR3) schematic to derive the tension distribution.

In TR3, both side of the wire is fixed at the end-effector and the tension is applied by pulling a movable pulley that is located at the middle of the wire as shown in B.5. Since the movable pulley is used, friction between the section b and section c is defined by a rolling resistance of the bearing. Here, the friction between section 2 and section b is not defined because wire at the section 1 and section 2 does not move. However, by considering the wire elongation, the friction between the section 2 and section b is also considered as a kinetic friction. With the above assumption, the relationship of the tension in each section can be described as Eq (B.28) - Eq (B.33).

$$T_M = T_b + T_c \tag{B.28}$$

$$T_b - T_2 = T_b(1 - e^{-\mu_s \theta_s}) \tag{B.29}$$

$$T_2 - T_1 = T_2(1 - e^{-\mu_t \pi}) \tag{B.30}$$

$$T_b - T_c = T_b(1 - e^{-\mu_b \pi}) \tag{B.31}$$

$$T_c - T_3 = T_c(1 - e^{-\mu_s \theta_s}) \tag{B.32}$$

$$T_3 - T_4 = T_3(1 - e^{-\mu_t \pi}) \tag{B.33}$$

Using the Eq (B.28) - Eq (B.33), final tension distribution can be obtained as Eq (B.34) - Eq (B.38).

$$T_1 = T_M K_b e^{-\mu_s \theta_s - \mu_t \pi} \tag{B.34}$$

$$T_2 = T_M K_b e^{-\mu_s \theta_s} \tag{B.35}$$

$$T_3 = T_M K_b e^{-\mu_b \pi - \mu_s \theta_s} \tag{B.36}$$

$$T_4 = T_M K_b e^{-\mu_b \pi - \mu_s \theta_s - \mu_t \pi} \tag{B.37}$$

$$K_b = (1 + e^{-\mu_b \pi})^{-1} \tag{B.38}$$

In this tendon routing, thanks to the wire elongation, difference of the tension at the section 2 and section 3 do not differ significantly from the tension differences at the section b and the section c even the friction of the Bowden cable is considered. When the exact value about friction coefficient is used in the above equations, the tension distribution of TR3 can be summarized as Table.B.3.

| TR3 | $T_M$ | $T_1$ | $T_2$ | $T_3$ | $T_4$ |
|---|---|---|---|---|---|
| | 1 | 0.09 | 0.16 | 0.16 | 0.09 |
| Ratio | - | 18(%) | 32(%) | 32(%) | 18(%) |

**Table B.3:** Tension distribution of the tendon routing 3

## B.5. Tension distribution of the tendon routing 4

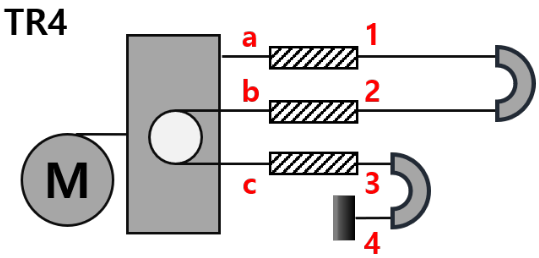


**Figure B.6: Schematic of tendon routing 4**

Tendon routing 4 (TR4) schematic to derive the tension distribution.

In TR4, one side of the wire is fixed at the end-effector while the other side of wire is fixed at the motor. Also, the movable pulley is used between section b and section c to apply kinetic constraints at two fingers.

In this case, tension distribution can be easily obtained because the moving direction of the wire is straightforward. Here, when the motor pulls the wire, the wire passes from the section 4 to section 1 and finally it is pulled to the section a. Therefore, the force equations about tension can be described as shown in Eq (B.39) - Eq (B.45).

$$T_M = T_a + T_b + T_c \tag{B.39}$$

$$T_a - T_1 = T_a(1 - e^{-\mu_s \theta_s}) \tag{B.40}$$

$$T_1 - T_2 = T_1(1 - e^{-\mu_t \pi}) \tag{B.41}$$

$$T_2 - T_b = T_2(1 - e^{-\mu_s \theta_s}) \tag{B.42}$$

$$T_b - T_c = T_b(1 - e^{-\mu_b \pi}) \tag{B.43}$$

$$T_c - T_3 = T_c(1 - e^{-\mu_s \theta}) \tag{B.44}$$

$$T_3 - T_4 = T_3(1 - e^{-\mu_s \pi}) \tag{B.45}$$

Using the Eq (B.39) - Eq (B.45), final tension distribution can be obtained as Eq (B.46) - Eq (B.50).

$$T_1 = K_{tr4} T_M e^{-\mu_s \theta_s} \tag{B.46}$$

$$T_2 = K_{tr4} T_M e^{-\mu_s \theta_s - \mu_t \pi} \tag{B.47}$$

$$T_3 = K_{tr4} T_M e^{-3\mu_s \theta_s - \mu_t \pi - \mu_b \pi} \tag{B.48}$$

$$T_4 = K_{tr4} T_M e^{-3\mu_s \theta_s - 2\mu_t \pi - \mu_b \pi} \tag{B.49}$$

$$K_{tr4} = (1 + e^{-2\mu_s \theta_s - \mu_t \pi} + e^{-2\mu_s \theta_s - \mu_t \pi - \mu_b \pi})^{-1} \tag{B.50}$$

In TR3, the tension difference between section 2 and section 3 is small while in TR4 the tension difference between these two sections is large. This is caused by the difference in the direction of wire movement in both paths. – In TR3, the wire moves in the direction pulled into sections $b$ and $c$ in sections 2 and 3. In TR4, on the other hand, the wire moves in the direction from section 3 to section $c$ and from section $b$ to section

| TR4 | $T_M$ | $T_1$ | $T_2$ | $T_3$ | $T_4$ |
|---|---|---|---|---|---|
| | 1 | 0.29 | 0.16 | 0.05 | 0.03 |
| Ratio | - | 54(%) | 31(%) | 10(%) | 6(%) |

**Table B.4:** Tension distribution of the tendon routing 4

2. − When the exact value about friction coefficient is used in the above equations, the tension distribution of TR4 can be summarized as shown in Table.B.4.

## B.6. Tension distribution of the tendon routing 5

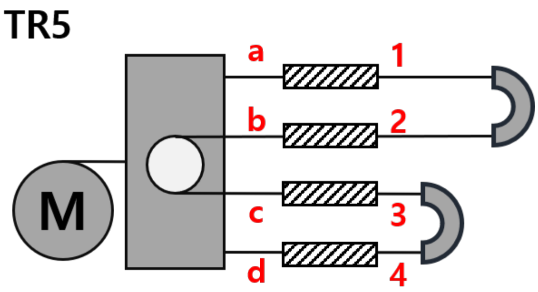


**Figure B.7: Schematic of tendon routing 5**

Tendon routing 5 (TR5) schematic to derive the tension distribution.

In TR5, both side of the wire is fixed at the motor and kinetic constraint is also applied by a movable pulley that is installed at the motor. Here, the wire moves similar to the motion of wire at the TR4. In this tendon routing, the force equations about tension can be easily obtained as shown in Eq (B.51) - Eq (B.58).

$$T_M = T_a + T_b + T_c + T_d \tag{B.51}$$

$$T_a - T_1 = T_a(1 - e^{-\mu_s \theta_s}) \tag{B.52}$$

$$T_1 - T_2 = T_1(1 - e^{-\mu_t \pi}) \tag{B.53}$$

$$T_2 - T_b = T_2(1 - e^{-\mu_s \theta_s}) \tag{B.54}$$

$$T_b - T_c = T_b(1 - e^{-\mu_b \pi}) \tag{B.55}$$

$$T_c - T_3 = T_c(1 - e^{-\mu_s \theta_s}) \tag{B.56}$$

$$T_3 - T_4 = T_3(1 - e^{-\mu_t \pi}) \tag{B.57}$$

$$T_4 - T_d = T_4(1 - e^{-\mu_s \theta_s}) \tag{B.58}$$

Using the Eq (B.51) - Eq (B.58), final tension distribution can be obtained as Eq (B.59) - Eq (B.63).

$$T_1 = K_{tr5} T_M e^{-\mu_s \theta_s} \tag{B.59}$$

$$T_2 = K_{tr5} T_M e^{-\mu_s \theta_s - \mu_t \pi} \tag{B.60}$$

$$T_3 = K_{tr5} T_M e^{-3\mu_s \theta_s - \mu_t \pi - \mu_b \pi} \tag{B.61}$$

$$T_4 = K_{tr5} T_M e^{-3\mu_s \theta_s - 2\mu_t \pi - \mu_b \pi} \tag{B.62}$$

$$K_{tr5} = (1 + e^{-2\mu_s \theta_s - \mu_t \pi}(1 + e^{-\mu_b \pi} + e^{-\mu_t \pi - \mu_b \pi}))^{-1} \tag{B.63}$$

Since the direction of the wire in this tendon routing is similar to that of the wire in TR4, the tension distribution shows similar to that of TR4. The only different thing is $K_{tr5}$ because this tendon routing pulls more wire than the TR4. Here, we can infer that wire at the section $a$ or section $d$ increases the difference in tension between section 2 and section 3. – Wire at the section $a$ or the section $d$ roles to apply kinematic constraints

| TR5 | $T_M$ | $T_1$ | $T_2$ | $T_3$ | $T_4$ |
|---|---|---|---|---|---|
| | 1 | 0.18 | 0.10 | 0.03 | 0.02 |
| Ratio | - | 54(%) | 31(%) | 10(%) | 6(%) |

**Table B.5:** Tension distribution of the tendon routing 5

on the wire and it forces to make movement of the wire. When the exact value about friction coefficient is used in the above equations, the tension distribution of TR5 can be summarized as Table.B.5.

## B.7. Tension distribution of the tendon routing 6

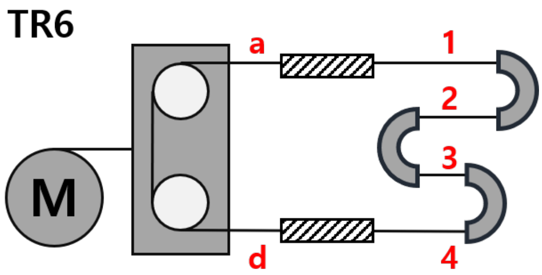


**Figure B.8: Schematic of tendon routing 6**

Tendon routing 6 (TR6) schematic to derive the tension distribution.

In TR6, both side of the wire has no fixation point. This tendon routing requires to connect both end of the wire. This connection sometimes can cause a problem in practical application. This tendon routing makes two kinetic constraints by using both movable pulley and fixed pulley. The result of TR6 can be compared with the result of TR2 or TR3. We can say that TR2 applies kinematic constraints between wire at section 1 and section 4 while TR6 applies kinetic constraints between wire at the section 1 and section 4.

The difference of constraints make big difference in tension distribution because kinetic constraints make wires in two sections have the same force, while kinematic constraints cause the wires in two sections to move the same distance. In TR6, the force equations about tension can be described as shown in Eq (B.64) - Eq (B.70).

$$T_M = T_a + T_d \tag{B.64}$$

| TR6 | $T_M$ | $T_1$ | $T_2$ | $T_3$ | $T_4$ |
|---|---|---|---|---|---|
| | 1 | 0.16 | 0.09 | 0.09 | 0.16 |
| Ratio | - | 32(%) | 18(%) | 18(%) | 32(%) |

**Table B.6:** Tension distribution of the tendon routing 6

$$T_1 - T_2 = T_1(1 - e^{-\mu_t \pi}) \tag{B.65}$$

$$T_2 - T_3 < T_2(1 - e^{-\mu_{t.s} \pi}) \tag{B.66}$$

$$T_4 - T_3 = T_4(1 - e^{-\mu_t \pi}) \tag{B.67}$$

$$T_a - T_1 = T_a(1 - e^{-\mu_s \theta_s}) \tag{B.68}$$

$$T_d - T_4 = T_d(1 - e^{-\mu_s \theta_s}) \tag{B.69}$$

$$T_a - T_d = T_a(1 - e^{-\mu_b \theta_b}) \tag{B.70}$$

Using the Eq (B.64) - Eq (B.70), final tension distribution can be obtained as Eq (B.71) - Eq (B.75).

$$T_1 = T_M K_b e^{-\mu_s \theta_s} \tag{B.71}$$

$$T_2 = T_M K_b e^{-\mu_s \theta_s - \mu_t \pi} \tag{B.72}$$

$$T_3 = T_M K_b e^{-\mu_b \pi - \mu_s \theta_s - \mu_t \pi} \tag{B.73}$$

$$T_4 = T_M K_b e^{-\mu_s \theta_s - \mu_b \pi} \tag{B.74}$$

$$K_b = (1 + e^{-\mu_b \pi})^{-1} \tag{B.75}$$

The tension distribution of TR6 shows same with that of TR3. It is because of the friction between section 2 and section3. In these force equations, relationship between tension at section 2 and tension at section 3 is also defined by static friction. It is true that the friction can be defined as kinetic friction if there are elongation. However, even the wire elongation is present, there may be no wire movement between sections in the Teflon tube in this tendon routing. –If the tensions on both sides of the Teflon tube are exactly the same, they may extend in both directions from the center of the Teflon tube.– With this assumption, we obtained tension distribution and can be described as Table.B.6.

## B.8. Tension distribution of the tendon routing 7

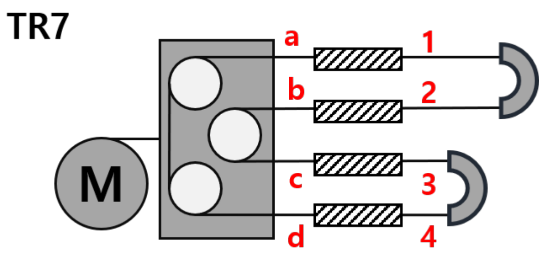


**Figure B.9: Schematic of tendon routing 7**

Tendon routing 7 (TR7) schematic to derive the tension distribution.

In TR7, as same as TR6, both end of the wire is connected to each other. In this case, there are two kinetic constraints between section $a$ and section $d$ or between section $b$ and section $c$. Since movable pulleys are used, the friction of the wire between section a and section d, and friction between section b and section c can be easily obtained. Here, the situation in the Teflon tube between section 1 and section 2 or section 3 and section 4 is similar to the situation in the Teflon tube between section 2 and 3 of TR6. Therefore, the force equations about tension can be described as Eq (B.76) - Eq (B.84).

$$T_M = T_a + T_b + T_c + T_d \tag{B.76}$$

$$T_3 - T_4 < T_3(1 - e^{-\mu_t \pi}) \tag{B.77}$$

$$T_1 - T_2 < T_1(1 - e^{-\mu_t \pi}) \tag{B.78}$$

| TR7 | $T_M$ | $T_1$ | $T_2$ | $T_3$ | $T_4$ |
|---|---|---|---|---|---|
| | 1 | 0.32 | 0.32 | 0.32 | 0.32 |
| Ratio | - | 25(%) | 25(%) | 25(%) | 25(%) |

**Table B.7:** Tension distribution of the tendon routing 7

$$T_a - T_1 = T_a(1 - e^{-\mu_s \theta_s}) \tag{B.79}$$

$$T_b - T_2 = T_b(1 - e^{-\mu_s \theta_s}) \tag{B.80}$$

$$T_c - T_3 = T_c(1 - e^{-\mu_s \theta_s}) \tag{B.81}$$

$$T_d - T_4 = T_d(1 - e^{-\mu_s \theta_s}) \tag{B.82}$$

$$T_a - T_d = T_a(1 - e^{-\mu_b \pi}) \tag{B.83}$$

$$T_b - T_c = T_b(1 - e^{-\mu_b \pi}) \tag{B.84}$$

Using the Eq (B.76) - Eq (B.84), final tension distribution can be obtained as Eq (B.85) - Eq (B.89).

$$T_1 = 0.5 K_b T_M e^{-\mu_s \theta_s} \tag{B.85}$$

$$T_2 = 0.5 K_b T_M e^{-\mu_s \theta_s} \tag{B.86}$$

$$T_3 = 0.5K_bT_Me^{-\mu_s\theta_s-\mu_b\pi} \tag{B.87}$$

$$T_4 = 0.5K_bT_Me^{-\mu_s\theta_s-\mu_b\pi} \tag{B.88}$$

$$K_b = (1 + e^{-\mu_b\pi})^{-1} \tag{B.89}$$

We can see that the tension distribution of TR7 is relatively uniform than other tendon routings. If the assumption that there is no wire movement between sections 3 and 4 and between sections 1 and 2 is incorrect, there may be friction in the Teflon tube. In such a situation, it is necessary to verify experimentally because the movement occurs in the direction of minimizing energy. The comparison between the modeling results and the experimental results is described in the next chapter.− Fortunately, friction between section 1 and section 2 or friction between section 3 and section 4 were negligible in the experiment and is explained in Figure B.11− When the exact value about friction coefficient is used in the above equations, the tension distribution of TR7 can be summarized as Table.B.7.

## B.9. Residual friction according to the tendon routing

The friction at the tendon routing not only reduces the efficiency of the robot and makes uneven fingertip force but also induces the residual friction. When the residual friction exists, generating the motion could be difficult. It could be easily understood by looking for the flexion of the Exo-Glove and the Exo-Glove II; Additional experiment is performed with a single person using Exo-Glove and Exo-Glove II. In the case of the Exo-Glove, the initial, flexed, and released joint angle is 0.18 (rad), 0.86 (rad), and 0.79 (rad) respectively. It means that even the tension of the flexion tendon is removed, the joint angle does not restore to its initial position. However, on the other hand, in the case of the Exo-Gove II, the initial, flexed, and released joint angle each was 0.17 (rad), 0.90 (rad), and 0.61 (rad); This result are described in the Figure B.10 (a). When the residual friction exists, relatively large amount of extension tension is required as shown in the Figure B.10 (b). In the Exo-Glove, about 19.5N is required to extend the finger to make the initial posture. However, in the Exo-Glove II, it is possible to extend the finger with only 6.2 N of the extension tension. The residual friction can be also induced by looking at the hysteresis graph shown in the Figure B.10 (c) and (d); (c) and (d) each represents the hysteresis graph of the Exo-Glove and the Exo-Glove II. Here, output tension (i.e, tension at the end-effector tendon) is measured as a function of the input tension (i.e, tension at the motor part). As it can be seen in the figure, residual friction exists a lot in the Exo-Glove.

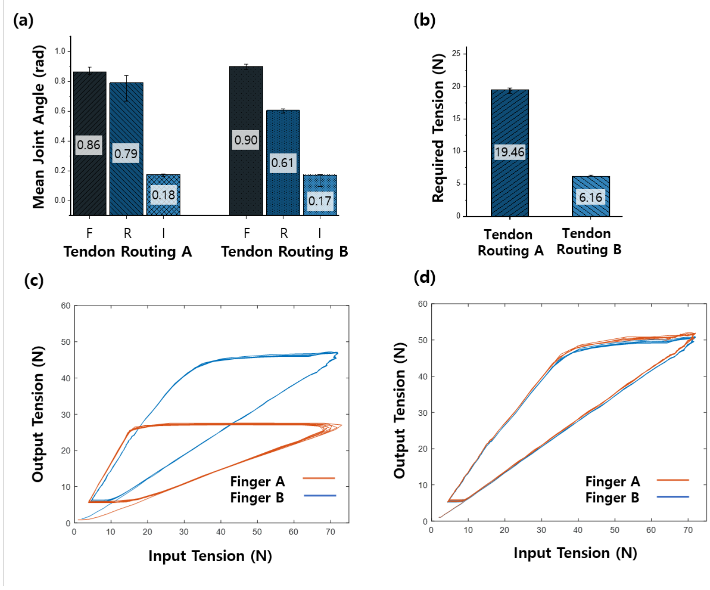


**Figure B.10: Experimental result for the residual friction**

Experimental results that indirectly measure the residual friction of the wire. Tendon routing A is the Exo-Glove tendon path while tendon routing B is the Exo-Glove II tendon path. **(a)** shows the mean joint angle of each cases: case 1) Joint angle at flexion, case 2) Joint angle when the flexor wire tension is removed, and case 3) Joint angle at the initial state. Here, mean joint angle is mean value of MCP, PIP, and DIP joint angle. F, R, I at the x-axis each means flexion, release, and initial state respectively. The number inside the bar graph is the mean value of the each case; **(b)** shows tension required to extend the finger after flexion for tendon routing A and tendon routing B, respectively. Also, the hysteresis in tension domain was measured. **(c)** shows the output tension (i.e, tension at the end-effector) as a function of the input tension (i.e, tension at the motor part) in the Exo-Glove. **(d)** shows the output tension as a function of the input tension in the Exo-Glove II.

## B.10. Conclusion

As a result, the simulated results shown in Table B.1 - Table B.7 can be summarized and can be compared with experimental results as in Table B.8 and Figure.B.11. Here, line + symbol graph depicts the simulation results while the bar graph shows the experimental results. All simulation results are normalized so that the sum of T1 and T4 is equal to 1. As can be seen from the figure, the tension distributions of the seven tendon routings obtained through simulation and experimentation show a similar tendency. When the friction coefficient between Teflon tube and the wire is 0.18, which is a value obtained in the previous research, the rms error between experimental and simulation results is 13.6%. However, rms error can be minimized to 3.4% by setting the friction coefficient to 0.09. The smaller friction measured than that measured in the previous research is inferred by the effect of the spring used to prevent deformation of the Teflon tube; In the previous study, force measurement were done without preventing the deformation of the Teflon tube, whereas in this study, the surface of the Teflon tube was wrapped with a spring to minimize the deformation of the Teflon tube. It is true that using springs could be an unfair measurement because the springs are not used in the actual wearable robot application. Nevertheless, we used the springs for more reliable data acquisition. In fact, both values 0.09 and 0.18 are not a problem because they are all within the range shown in the literature; the literature value of friction coefficient between Teflon tube and steel is known as 0.05 - 0.2. Since the results of simulation and experiment show similar trends, we can conclude that the proposed method to obtain the optimal tendon routing could be a possible solution.

| Ratio | $T_M$ | $T_1$ | $T_2$ | $T_3$ | $T_4$ |
|---|---|---|---|---|---|
| TR1 | 1 | 0.32 | 0.18 | 0.10 | 0.06 |
| TR2 | 1 | 0.21 | 0.12 | 0.07 | 0.12 |
| TR3 | 1 | 0.09 | 0.16 | 0.16 | 0.09 |
| TR4 | 1 | 0.29 | 0.16 | 0.05 | 0.03 |
| TR5 | 1 | 0.18 | 0.10 | 0.03 | 0.02 |
| TR6 | 1 | 0.16 | 0.09 | 0.09 | 0.16 |
| TR7 | 1 | 0.32 | 0.32 | 0.32 | 0.32 |
| **Distribution** | $T_M$ | $T_1$ | $T_2$ | $T_3$ | $T_4$ |
| TR1 | - | 48(%) | 27(%) | 16(%) | 9(%) |
| TR2 | - | 41(%) | 23(%) | 13(%) | 23(%) |
| TR3 | - | 18(%) | 32(%) | 32(%) | 18(%) |
| TR4 | - | 54(%) | 31(%) | 10(%) | 6(%) |
| TR5 | - | 54(%) | 31(%) | 10(%) | 6(%) |
| TR6 | - | 32(%) | 18(%) | 18(%) | 32(%) |
| TR7 | - | 25(%) | 25(%) | 25(%) | 25(%) |

**Table B.8:** Comparison of the tension distribution of the seven tendon routings.

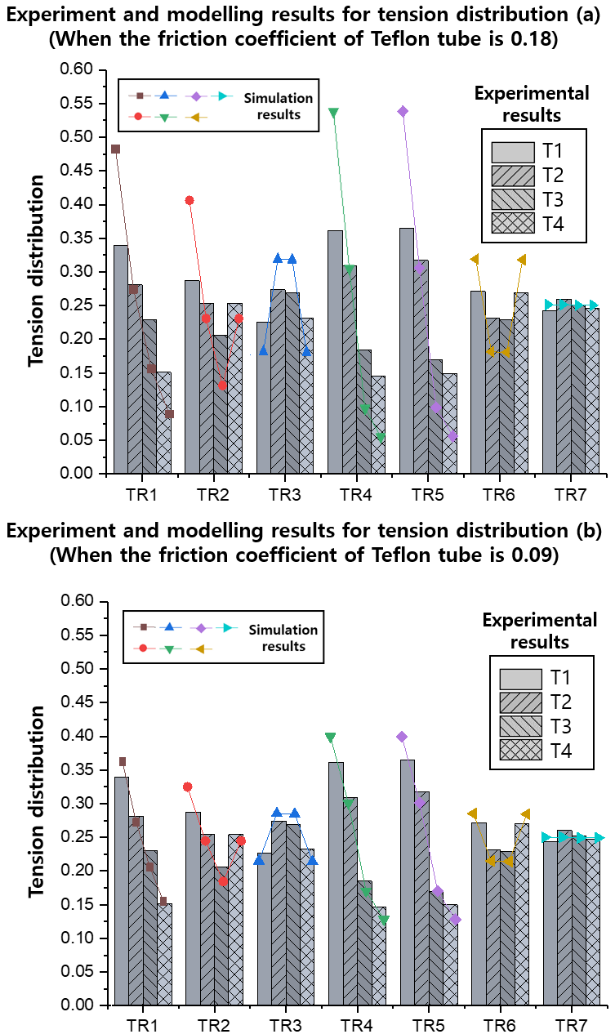


**Figure B.11: Tension distribution of the seven different tendon routings**

Bar graph of the figure means the experimental results of tension distribution in each tendon routings while the line+symbol graph of the figure means the simulation results. **(a)** shows the simulation results with the friction coefficient of 0.18 and **(b)** shows the simulation results with the friction coefficient of 0.09.

# Appendix C

# Theoretical Background of Product of Exponential

In robotics, a relation between a joint angle and an end-effector can often be expressed through forward and inverse kinematics. In this appendix, we introduce a method to solve the kinematics of an index finger. We propose a method of finding the exact center of rotation in a finger joint using the position of Vicon markers attached on the skin. In order to find the center of rotation, the Product of Exponential method (POE) is used.

First, the position of each marker measured directly from the Vicon expressed in a fixed frame {F} should be transformed with respect to a moving frame {M}, which moves along with the hand, since it is the relative position of the finger with respect to the hand that is meaningful. We defined this reference moving frame {M} to be located at the back of the hand , since this part does not move relative to other parts in a hand while an index finger is in motion. The coordinate systems of the fixed frame {F} and reference frame {M} are shown in Figure C.1 (a). Using this concept, transformation of a marker position $X_M \in \mathbb{R}^{3\times 1}$ from frame

{F} into frame {M} can be written as Eq (C.1), using a transformation matrix $T_{MF} \in \mathbb{R}^{4\times4}$. $\overrightarrow{X_M}$, $\overrightarrow{X_F}$, and $\overrightarrow{P_M}$ are illustrated in Figure C.1 (a), and $R_{MF}$ is a rotation matrix from frame {M} to {F}.

$$\begin{bmatrix} X_M \\ 1 \end{bmatrix} = T_{MF} \begin{bmatrix} X_F \\ 1 \end{bmatrix} = \begin{bmatrix} R_{MF} & P_{MF} \\ 0 & 1 \end{bmatrix} \begin{bmatrix} X_F \\ 1 \end{bmatrix} \tag{C.1}$$

The basic concept of deriving the transformation matrix in Eq (C.1) is expressing the $\overrightarrow{X_M}$ vector with respect to the frame {F}, as shown in Eq (C.3), while $\hat{x}_F$, $\hat{y}_F$, $\hat{z}_F$ can be written as Eq (C.2). From the relationship between the two coordinates shown in Eq (C.2), the position of the markers in frame {M} can be expressed in a matrix form, as shown in Eq (C.3). Other details about coordinate transformation can be found in previous works about robotics (Lynch & Park 2016). One thing different from traditional robotics is that usually a transformation matrix shows different forms because the matrices are defined to transform a vector from a moving frame to a fixed frame.

$$\begin{aligned} \hat{x}_F &= v_{xx}\hat{x}_M + v_{xy}\hat{y}_M + v_{xz}\hat{z}_M \\ \hat{y}_f &= v_{yx}\hat{x}_M + v_{yy}\hat{y}_M + v_{yz}\hat{z}_M \\ \hat{z}_F &= v_{zx}\hat{x}_M + v_{zy}\hat{y}_M + v_{zz}\hat{z}_M \end{aligned} \tag{C.2}$$

$$
\begin{aligned}
\vec{X}_M &= X_{Mx}\hat{x}_M + X_{My}\hat{y}_M + X_{Mz}\hat{z}_M \\
&= \vec{X}_F - \vec{P}_M \\
&= X_{Fx}\hat{x}_F + X_{Fy}\hat{y}_F + X_{Fz}\hat{z}_F - (Pm_x\hat{x}_F + Pm_x\hat{y}_F + Pm_x\hat{z}_F) \\
&= (X_{Fx} - Pm_x)(v_{xx}\hat{x}_M + v_{xy}\hat{y}_M + v_{xz}\hat{z}_M) \\
&+ (Y_{Fy} - Pm_y)(v_{yx}\hat{x}_M + v_{yy}\hat{y}_M + v_{yz}\hat{z}_M) \\
&+ (Z_{Fz} - Pm_z)(v_{zx}\hat{x}_M + v_{zy}\hat{y}_M + v_{zz}\hat{z}_M) \\
&= \begin{bmatrix} v_{xx} & v_{yx} & v_{zx} \\ v_{xy} & v_{yy} & v_{zy} \\ v_{xz} & v_{yz} & v_{zz} \end{bmatrix} (X_F - Pm) \\
&= R_{MF}(X_F - Pm) \\
&= R_{MF}X_F + P_{MF}
\end{aligned}
\tag{C.3}
$$

A transformation matrix can also be expressed as products of exponential (POE) by introducing a screw axis $S \in \mathbb{R}^{6\times1}$. A screw axis S is equal to $[w, v]^T$, where $w$ and $v$ refer to an angular and a linear velocity of a moving frame, respectively. Eq (C.4) is an example of a POE expression that can be used in the case illustrated in Figure C.1 (b). Figure C.1 (b) shows a rotation of a moving frame $\{M_1\}$ to the frame $\{M_2\}$ about a rotational axis $\hat{w}$. In Eq (C.4), $M_{M_1M_2}$ refers to the transformation matrix from frame $\{M_1\}$ to $\{M_2\}$ at their initial position, and $e^{[s]\theta}$ in Eq (C.5) refers to the transformation that actually occurs due to the rotation, while $[S] = \begin{bmatrix} [w] & v \\ 0 & 0 \end{bmatrix} \in \mathbb{R}^{4\times4}$ is a matrix form of $S$, and $\theta$ is an angle of rotation. Vector $Q$ directs to an arbitrary point on the rotational axis and is expressed in frame $\{M_1\}$. In this sense, we can express the rotation from a coordinate to another along the screw axis.

$$T_{M_2M_1} = e^{[S]\theta} M_{M_2M_1} \tag{C.4}$$

$$e^{[S]\theta} = \begin{bmatrix} e^{[\hat{w}]\theta} & G(\theta)v \\ 0 & 1 \end{bmatrix} = \begin{bmatrix} R & P \\ 0 & 1 \end{bmatrix} \tag{C.5}$$

$$\begin{aligned} G(\theta) &= I\theta + (1-\cos\theta)[\hat{w}] + (\theta - \sin\theta)[\hat{w}]^2 \\ G^{-1}(\theta) &= \frac{1}{\theta}I - \frac{1}{2}[\hat{w}] + (\frac{1}{\theta} - \frac{1}{\theta}\cot\frac{\theta}{2})[\hat{w}]^2 \end{aligned} \tag{C.6}$$

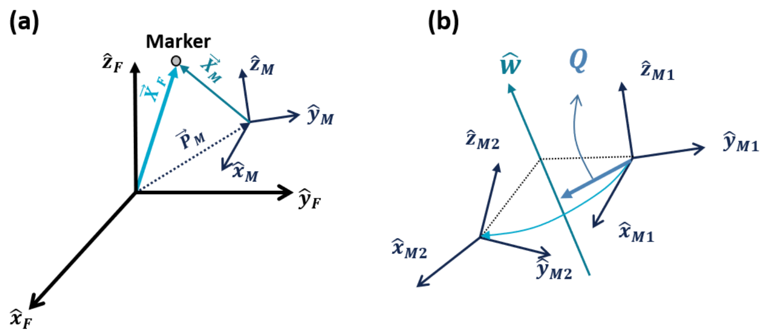


**Figure C.1: Schematic view to explain the transformation and rotation of coordinates**

**(a)** shows two different ways to define the marker position in different frames (i.e, Moving frame or Fixed frame). **(b)** shows a method to define screw parameters in Product of Exponential formula.

Based on the relationship between a transformation matrix $T$ using Vicon data and $T$ using the POE method in Eq (C.4), we can finally estimate the center of rotation in a finger joint as a function of the rotation angle. The angle of rotation $\theta$ and rotational axis $\hat{w}$ can be obtained from

Eq (C.7) and Eq (C.8). Here, $r_{ii}$ in Eq (C.7) is an $i^{th}$ component in the main diagonal of a rotation matrix and $w_x, w_y, w_z$ in Eq (C.8) are x, y, and z components of $\hat{w}$. From Eq (C.5), the linear velocity is equal to $G^{-1}(\theta)p$, while $G^{-1}(\theta)$ can be written as Eq (C.6). Knowing that the linear velocity is equal to $-w \times Q$, we can determine the direction and magnitude of the vector $Q$, which points at the joint center, as in Eq (C.9) and Eq (C.10). Eq (C.9) and Eq (C.10) are based on an assumption that we are looking for the vector $Q$ that is perpendicular to the rotational axis $\hat{w}$. This method can be applied to finding the center of the finger joints.

$$\theta = \cos^{-1}(\frac{r_{11} + r_{22} + r_{33} - 1}{2}) \tag{C.7}$$

$$[\hat{w}] = \begin{bmatrix} 0 & -w_z & w_y \\ w_z & 0 & -w_x \\ -w_y & w_x & 0 \end{bmatrix} = \frac{1}{2\sin\theta}(R - R^T) \tag{C.8}$$

$$\hat{Q} = \hat{w} \times \hat{v} \tag{C.9}$$

$$\| Q \| = \frac{\| v \|}{\| \hat{w} \|} \tag{C.10}$$

In the case of an MCP joint, which has two degrees of freedom, instead of using Eq (C.4) we should use Eq (C.11) when expressing the transformation matrix. Eq (C.11) consists of products of exponentials based on two rotational axes, each of which are abduction and flexion, respectively. Since the transformation matrix measured from the Vicon data includes both abduction and flexion information, we should separate it into two different rotations and find out the rotation angles for each.

$$T_{MCP} = e^{[S_1]\theta_1} e^{[S_2]\theta_2} M_{initial} \tag{C.11}$$

Here, we introduce a numerical method to estimate $\theta_1$ and $\theta_2$ using the space Jacobian $J_s(\theta)$. This method starts by setting the initial guesses of $\theta_1$ and $\theta_2$ as $\theta_{initial} \in \mathbb{R}^{2\times1}$. Then we define a matrix $[A] \in \mathbb{R}^{4\times4}$ as Eq (C.12). $T(\theta_{initial})$ is a transformation matrix with $\theta_{initial}$ as an input, and $T^{-1}$ is calculated from the ground truth data measured by Vicon. The next step is to calculate $\Delta\theta$ from Eq (C.13). The space Jacobian $J_s(\theta)$ can be calculated as shown in Eq (C.14) and Eq (C.15). Finally, we can update $theta_{initial}$ by $\theta_{initial} + \Delta\theta$ and repeat the whole process until $\theta$ converges. In this way, we can determine the abduction and flexion angle separately at the MCP joint, and hence, we can also calculate the distance between two adjacent joints, which can also be regarded as the length of phalanges. More detailed information about the numerical method used in this process is elaborated in (Lynch & Park 2016).

$$[A] = log(T(\theta_{initial})T^{-1}) \tag{C.12}$$

$$-A = J_s(\theta)\Delta\theta \tag{C.13}$$

$$J_s(\theta) = [S_1|{S_2}^{'}] \tag{C.14}$$

$$\begin{gathered} {S_2}^{'} = Ad_{e^{[S1]\theta 1}}(S_2) \\ (\text{where, } Ad_T(S) = \begin{bmatrix} R & 0 \\ [P]R & R \end{bmatrix} S \in \mathbb{R}^{6\times6}) \end{gathered} \tag{C.15}$$

# Appendix D

# Kinematic Calibration with Product of Exponential

The process of matching the kinematic model is usually named as *kinematic system identification*. In this thesis, a kinematic system identification is conducted based on the product of exponential formulas (POEs). Basic explanations about the product of exponential formulas are included in the appendix C. Overall process are all represented in the previous research about the system identification using POEs (Okamura & Park 1996).

To find out the thumb kinematic parameters, which is the main goal of kinematic calibration in this thesis, the thumb motion is measured by the Vicon motion capture system as shown in the Figure D.1 (a). Since the CMC joint has three degree of freedoms, the internal screw parameters could be explained as shown in the Figure D.1 (b).

$$\begin{aligned} X_{F.Tip} &= f(S, \theta) \\ \dot{X}_{F.Tip} &= J_m(S, \theta)\dot{\theta} \end{aligned} \tag{D.1}$$

The kinematic system identification starts from the Eq (D.1), which represents the relationship between the joint angle $\theta$ and the fingertip position $X_{F.Tip}$ . With given equation, the error of the end-effector could be represented as Eq (D.2). Here, the error $dX_{F.Tip}$ is $6 \times 1$ vector which represents the position error and orientation error.

$$dX_{F.Tip} = \frac{\partial f}{\partial \theta} d\theta + \frac{\partial f}{\partial S} dS \tag{D.2}$$

Then, the calibration can be explained as a process of finding the optimal $d\theta$ and $dS$ that minimize the end-effector error; In mathematical expression, it can be represented as D.3 in least-square methods.

$$min\|dx - \frac{\partial f}{\partial \theta} d\theta - \frac{\partial f}{\partial S} dS\|^2 \tag{D.3}$$

$$g(\theta_1, \theta_2, ..., \theta_n) = e^{S_1\theta_1} e^{S_2\theta_2} \cdots e^{S_n\theta_n} M \tag{D.4}$$

The infinitesimal $dx$ can be represented by considering the manipulator jacobian $J_m$ in the Eq (5.1). When we represent the transformation matrix between the base frame and the end-effector frame in POE form as Eq (D.4), generalized velocity of end-effector frame can be represented as $\dot{g}g^{-1}$(Lynch & Park 2016). It can be represented in a form using manipulator jacobian as Eq (D.5).

$$\begin{aligned} \dot{g}g^{-1} &= S_1\dot{\theta_1} + e^{S_1\theta_1} S_2 e^{-S_1\theta_1} \dot{\theta_2} + \cdots \\ &+ e^{S_1\theta_1} \cdots \times e^{S_{n-1}\theta_{n-1}} S_n e^{-S_{n-1}\theta_{n-1}} \cdots e^{-S_1\theta_1} \dot{x_n} \\ &= J_m \times [\dot{\theta_1}\dot{\theta_2} \cdots \dot{\theta_n}]^T \end{aligned} \tag{D.5}$$

Since the $\dot{g}g^{-1}$ in the Eq (D.5) represents the velocity of the end-effector frame, the end-effector error can be represented by considering $dg \cdot g^{-1}$ which can be represented as Eq (D.6).

$$\begin{aligned} dg \cdot g^{-1} = {} & d(e^{S_1\theta_1})e^{-S_1\theta_1} \\ & + e^{S_1\theta_1}d(e^{S_2\theta_2})e^{-S_2\theta_2}e^{-S_1\theta_1} \\ & + \cdots + e^{S_1\theta_1}\cdots e^{S_{n-1}\theta_{n-1}}d(e^{S_n\theta_n}) \\ & \times e^{-}S_n\theta_n \cdots e^{-}S_1\theta_1 \\ & + e^{S_1\theta_1}\cdots e^{S_n\theta_n}(dM)M^{-1} \\ & \times e^{S_n\theta_n}\cdots e^{S_1\theta_1} \end{aligned} \tag{D.6}$$

The $\dot{g}g^{-1}$ can be represented in terms of adjoint map as shown in the Eq (D.7), where the definition of the adjoint map can be found in the appendix C. Here, $\Gamma$ represents screw parameters which can be expressed as $\Gamma = log(M)$.

$$\begin{aligned} dg \cdot g^{-1} = {} & S_1 d\theta_1 + Ad_{e^{S_1\theta_1}}(A_2)d\theta_2 \\ & + \cdots + Ad_{e^{S_1\theta_1}\cdots e^{A_{n-1}\theta_{n-1}}}(A_n)d\theta_n \\ & + \theta_1 \int_0^1 Ad_{e^{S_1\theta_1}}(A_1)du \\ & + \theta_2 Ad_{e^{S_1\theta_1}}(\int_0^1 Ad_{e^{S_2\theta_2}}(A_2)du) \\ & + \cdots + \theta_n Ad_{e^{S_1\theta_1}\cdots e^{S_{n-1}\theta_{n-1}}}(\int_0^1 Ad_{e^{S_n\theta_n}}(A_n)du) \\ & + Ad_{e^{S_1\theta_1}\cdots e^{S_n\theta_n}}(\int_0^1 Ad_{e^{\Gamma u}}(d\Gamma)du) \end{aligned} \tag{D.7}$$

Finally, the linearized equation about the end-effector error can be represented in a matrix form $y = AP$ as Eq (D.9). Here, $P$ means the vector of kinematic parameters as below:

$$P = \begin{bmatrix} d\theta_1 d\theta_2 \cdots d\theta_n & dS_1{}^T \cdots dS_n{}^T dS_M{}^T \end{bmatrix} \tag{D.8}$$

$$\begin{aligned} y &= [r_1 \mid r_2 \mid \cdots \mid r_n \mid Q_1 \mid Q_2 \mid \cdots \mid Q_n \mid Q_M]P \\ &\triangleq \mathbf{AP} \end{aligned} \tag{D.9}$$

The terminology $r_1$ to $r_n$ and $Q_1$ to $Q_M$ in the Eq (D.9) are brief expression for the compact form and these can be represented as Eq (D.10) - (D.12).

$$r_k = (\prod_{i=0}^{k-1} \begin{bmatrix} \Theta_i & 0 \\ [b_i]\Theta_i & \Theta_i \end{bmatrix}) \begin{bmatrix} w_k \\ v_k \end{bmatrix} \tag{D.10}$$

$$\begin{aligned} Q_k = (\prod_{i=0}^{k-1} & \begin{bmatrix} \Theta_i & 0 \\ [b_i]\Theta_i & \Theta_i \end{bmatrix})x_k \\ \times \int_0^1 & \begin{bmatrix} R_k(u) & 0 \\ [d_k]R_k(u) & R_k(u) \end{bmatrix} du \end{aligned} \tag{D.11}$$

$$\begin{aligned} Q_M = (\prod_{i=0}^{n} & \begin{bmatrix} \Theta_i & 0 \\ [b_i]\Theta_i & \Theta_i \end{bmatrix})x_k \\ \times \int_0^1 & \begin{bmatrix} R_M(u) & 0 \\ [d_M]R_M(u) & R_M(u) \end{bmatrix} du \end{aligned} \tag{D.12}$$

In the above equations ((D.10) - (D.12)), several variables such as $\Theta$, $b_i$, and etc. are not defined; These can be defined by represented form in the Eq (D.13) and (D.14) as below:

$$e^{S_i\theta_i} = \begin{bmatrix} \Theta_i & b_i \\ 01 & \end{bmatrix}, e^{S_i\theta_i u} = \begin{bmatrix} R_i(u) & d_i(u) \\ 01 & \end{bmatrix} \tag{D.13}$$

$$M = e^{\Gamma} = \begin{bmatrix} \Theta_M & b_M \\ 01 & \end{bmatrix}, e^{\Gamma u} = \begin{bmatrix} R_M(u) & d_M(u) \\ 01 & \end{bmatrix} \tag{D.14}$$

As a next step, we should think about the left-hand side of $dg \cdot g^{-1}$; since $dg$ means the error of the transformation matrix, it can be simply represented as Eq (D.15) where, $T_a$ is a transformation matrix obtained from the measured data and $T_n$ is computed transformation matrix using the nominal kinematic parameters (i.e, estimated transformation matrix).

$$\begin{aligned} dg \cdot g^{-1} &= (T_a - T_n){T_n}^{-1} \\ &= T_a{T_n}^{-1} - I \\ &= log(T_a{T_n}^{-1}) \\ &= y \end{aligned} \tag{D.15}$$

Therefore, by finding the kinematic parameter $P$ in the Eq (D.9), it is possible to conduct the kinematic calibration. In order to increase the performance of the kinematic calibration, it is quite obvious that the number of experiments should be increased; For instance, if we measure the position of the end-effector by motion capture camera, increase of the position data will increase the performance of the proposed kinematic calibration. If we assume that there are $m$ numbers of data, the linearized equation can be extended to the Eq (D.16) or to the compact form as Eq (D.17).

$$\begin{bmatrix} y_1 \\ y2 \\ \vdots \\ y_m \end{bmatrix} = \begin{bmatrix} A_1 \\ A2 \\ \vdots \\ A_m \end{bmatrix} \mathbf{P} \tag{D.16}$$

$$\hat{y} = \hat{A}\mathbf{P} \tag{D.17}$$

By solving the above equation with a least-square method, we can finally obtain the variations $p$ as shown in the Eq (D.18). Using the $p$, it is possible to reduce the kinematic error $dy$; By updating the kinematic parameter $P$ to $P'$ as shown in the Eq (D.19), we can reduce the kinematic error. Since the proposed optimization problem is a non-linear problem, the overall process should be iterated until the variations $p$ approach zero.

$$\mathbf{P} = (\hat{y}^T\hat{y})^{-1}\hat{y}^T\hat{y} \tag{D.18}$$

$$\mathbf{P'} = \mathbf{P} + \mathbf{p} \tag{D.19}$$

The overall process of the kinematic calibration is explained more detail in (Okamura & Park 1996). Also, the result of kinematic calibration in this thesis could be found in the section 5.5.1.

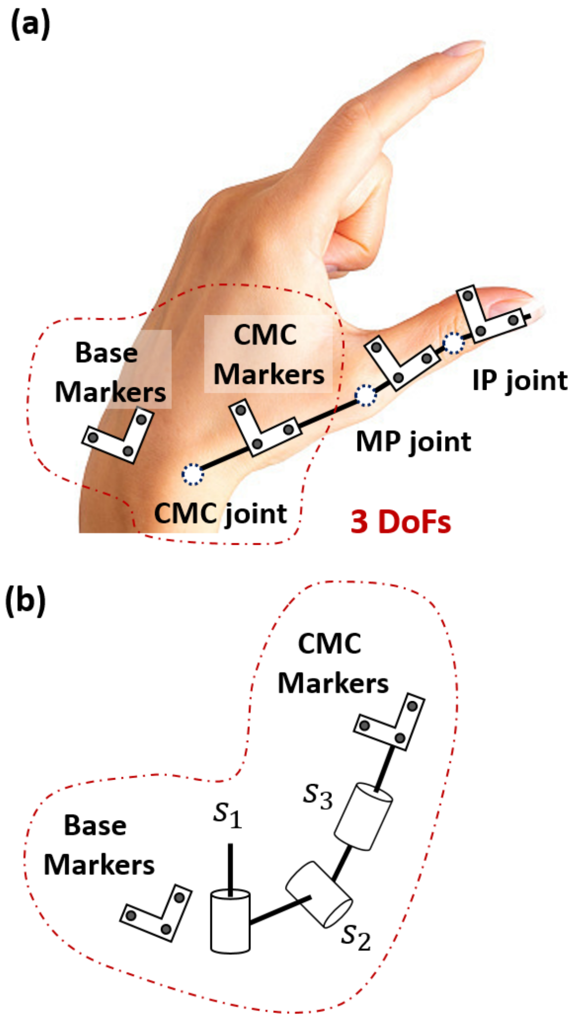


$$T_{base-CMC} = T_{b1}T_{12}T_{23}T_{3E}$$
$$= e^{s_1\theta_1}e^{s_2\theta_2}e^{s_3\theta_3}M$$

**Figure D.1: Kinematic parameters of the thumb**

**(a)** shows the thumb joints and markers used to calibrate the thumb kinematic parameters and **(b)** shows the target calibration model for the thumb joints.

# 슬라이더-텐던 구동기를 이용한 손 부위 착용형 로봇

서울대학교 대학원
기계항공공학부
김 병 철

## 요 약

손 부위 착용형 로봇의 개발은 로봇의 사용적 성능과 기능적 성능의 두 가지 성능 지표에 영향을 받는다. 기존 로봇들과 다르게 신체에 착용되어 사용되기 때문에 로봇의 부피, 무게, 착용의 편리성에 대한 고려가 필요하며 이는 사용적 성능에 해당하는 지표이다. 반면, 기능적 성능으로는 보조하는 관절의 수, 이를 통해 만들어내는 자세의 다양성, 실제로 낼 수 있는 힘의 크기와 같은 지표들이 존재한다. 이러한 두 가지 성능 지표는 로봇의 설계 방법을 통해 향상시킬 수 있지만 근본적으로 구동기의 수에 영향을 받는다. 많은 수의 관절을 보조하여 다양한 자세를 만들어내기 위해서는 구동기의 수가 많아져야 하며 큰 힘을 보조하기 위해서는 구동기의 크기가 커질수 밖에 없다. 하지만, 늘어난 구동기의 수와 커진 구동기의 크기는 자연스럽게 로봇의 부피와 무게에 부정적인 영향을 끼치기 때문에 적절한 수의 구동기가

사용되는 것이 중요하다. 기존 손 부위 착용형 로봇은 위의 문제를 해결하기 위해 보조하는 관절의 수보다 적은 수의 구동기를 사용하는 부족 구동 메커니즘을 활용하고 있으며 해당 관절들에 적절한 구속 조건을 부여함으로써 원하는 기능을 수행하도록 한다.

하지만, 부족 구동 메커니즘의 과도한 사용은 마찰 증가, 제어 자유도의 제약을 일으키기 때문에 로봇의 요구조건에 맞는 적절한 수의 구동기 사용이 중요하다. 본 학위 논문은 부족 구동 메커니즘의 성능을 확보하도록 개발된 슬라이더-텐던 구동기와 이를 사용한 손 부위 착용형 로봇을 제안한다. 슬라이더-텐던 구동기는 와이어 기반 착용형 로봇에 필요한 요구조건들을 만족시키도록 개발되었으며, 이를 토대로 개발된 손 부위 착용형 로봇은 적은 수의 구동기로도 충분한 보조 성능을 확보할 수 있음을 확인할 수 있었다. 본 학위 논문의 착용형 로봇은 엄지의 대립 운동과 검지, 중지의 굽힘 운동을 보조하도록 개발되었으며 부족 구동 메커니즘을 통해 네 개의 구동기만으로도 충분한 성능을 확보할 수 있음을 확인할 수 있었다. 또한, 본 연구는 부족 구동 메커니즘을 착용형 로봇에 적용하는 방법론과 해당 메커니즘으로 인해 발생하는 기존 문제들을 대처하는 방향성을 제시하고 있기 때문에 다양한 착용형 로봇 연구 및 기존 로봇들의 성능 향상 및 시스템 단순화에 기여할 것으로 예상된다.

**주요:** 착용형 로봇, 부족 구동 메커니즘, 와이어 구동기, 와이어 경로 최적화, 기계학습 기반 로봇 제어

**학 번:** 2014-30349